UCSF
UC San Francisco Electronic Theses and Dissertations

Title
Metabolic requirements necessitate microenvironmental crosstalk in breast cancer

Permalink
https://escholarship.org/uc/item/6g24523m

Author
Camarda, Roman

Publication Date
2018

Peer reviewed|Thesis/dissertation

eScholarship.org Powered by the California Digital Library
University of California

Metabolic requirements necessitate microenvironmental crosstalk in breast cancer

by

Roman Camarda

DISSERTATION

Submitted in partial satisfaction of the requirements for the degree of

DOCTOR OF PHILOSOPHY

in

Biomedical Sciences

in the

GRADUATE DIVISION

of the

UNIVERSITY OF CALIFORNIA, SAN FRANCISCO

To my mother, Lily Camarda, and my grandmother, Margaret Camarda

For their unconditional and unending love and support

Acknowledgements

I cannot imagine a more supportive and enjoyable environment for me to conduct my graduate studies than UCSF. More than anyone else at UCSF, I am indebted to my graduate advisor Andrei Goga. For so many reasons, I have been and will continue to be inspired by Andrei. As a scientist, he is passionate, creative, insightful, has a truly staggering depth of knowledge, and maintains a strong belief in the good of scientific inquiry. As a husband and a father, he is caring, committed, encouraging, and genuinely understanding. I joined Andrei's lab because I admired both his excitement and enthusiasm, as well as his trust in the scientists he mentors. I am deeply grateful for the freedom and support that Andrei provided me throughout my graduate studies, and I sincerely hope I can continue to channel the creative and open-minded nature that Andrei brings to his science throughout my career.

I would like to express thanks to my thesis committee, Alan Ashworth, Davide Ruggero and Shingo Kajimura. All three of these amazing scientists have provided so much invaluable advice and mentorship over the years, and all three have put up with countless knocks on their doors to ask for just one more thing. I would also like to acknowledge Zena Werb, Aaron Tward and Elad Ziv, as well as Dan Nomura at UC Berkeley, who have provided ongoing mentorship and tremendous support for all of my fellowship applications.

There would not have been any pursuit of graduate school without the guidance and mentorship of several people in Seattle. In particular, Jim Johnston, my sophomore biology teacher at Seattle Prep High School, deserves singular responsibility for putting me on the path of science. I am deeply indebted to Jim for years of mentorship and

support, and I am thankful to him and his wife Jamie for their tremendous friendship. I would also like to thank Michael Lagunoff, and all of the members of the Lagunoff lab I overlapped with, for teaching me what it really means to conduct academic research. Michael took a chance on a “squirrely” 19-year-old, and for that I am forever grateful. In addition, Tracie Delgado and Erica Sanchez were essential to my training in the Lagunoff lab, and introduced me to the world of cellular metabolism that I have been obsessed with ever since.

I am deeply grateful to the UCSF BMS program and all of its directors and administrators. Jason Cyster, Mark Ansel and Anita Sil provided excellent directorship of the program throughout my graduate studies, and I am thankful to all three for supporting my work and endless applications. To Lisa Magargal, Demian Sainz, Ned Molyneaux, Monique Piazza, Nate Jew, and everyone else in the BMS office, thank you so much for the boundless support they gave me. I cannot possibly list all of the ways they helped me during my time at UCSF, but I am sincerely grateful to each of them, and it’s been such a pleasure working with them.

When I joined the Goga lab, there were specific members without whom I never would have had as much fun as I did in graduate school. In particular, I would like to thank Brittany Anderton, Alicia Zhou and Dai Horiuchi. Brittany interviewed me during my recruitment to UCSF, mentored me during my rotation in the Goga lab, and was a constant source of encouragement. Alicia is one of the sharpest scientists I have ever met, held my hand intellectually and experimentally whenever I needed it, and has continued to provide invaluable advice for my life and career. Dai is a scientist’s scientist, has served as a constant source of inspiration with his persistence, passion

and commitment, and, just like Alicia, has continued to serve as an amazing source of advice and feedback. Finally, a big thank you to Sanjeev Balakrishnan, Henok Eyob, Celine Mahieu and Olga Momcilovic for all of their help supporting my studies.

To the current members of the Goga lab, they make every day in the lab fun, stimulating and exciting. It is a well-known fact that the PI is the only constant in a lab, and we have gone through many iterations over my time at UCSF, but I truly believe the current group of Gogans have found a rhythm that is really special, and I'm grateful to have been a part of it. To the postdocs, Andrew Beardsley, Matt Gruner, Seda Kilinc-Avsaroglu, Joyce Lee, Filomena Ricciardi, Julia Rohrberg, Dan Van de Mark, and our visiting scientist Sensen Lin, they have supported my scientific growth each and every day, and for that I will always be grateful. To the graduate students, Rachel Nakagawa and Jeremy Williams, thanks to them for all of the support, and best of luck with their remaining studies. Finally, to the research associate Moufida Taileb, and the technicians, Joy Gittens and Mercedes Joaquin, thanks for all the work they do to keep the lab running.

I would also like to acknowledge all of the collaborators I have worked with throughout my graduate studies. I can sincerely state that I am not a lone-wolf scientist, and for that reason and many more I am deeply indebted to all of the labs that supported my work. In particular I would like to thank Mark Ansel, Atul Butte, Shingo Kajimura, Gregor Krings, Dan Liebler, Dan Nomura, Hope Rugo, Melinda Sanders, John Shepherd, Aaron Tward, Zena Werb, Torsten Wittmann, and every member of the aforementioned labs that I worked with. I have enjoyed every collaboration I established, and I am grateful for the endless conversations and feedback provided.

To all of the members of the UCSF HSW6 and HSW7 community, as well as the Cell & Tissue Biology administrative staff, thanks for all of the support and feedback they provided throughout my graduate studies. I would like to specifically acknowledge Diane Barber for recruiting me to UCSF and mentoring me during my first rotation, and all of the members of the Barber lab, particularly Brad Webb, for making the first quarter of graduate school such a wonderful experience.

Moving from Seattle to San Francisco was an interesting and challenging transition. Thanks to all the fantastic friends that I've made in San Francisco, I always had an ear to bend and shoulder to lean on. To my BMS class, it was an honor to be part of such a sharp and fun group of talented scientists. To the BMS students, my year and otherwise, that I connected with on a deeper level, they know who they are, and I am sincerely grateful for their friendship and support. I love each of them, and I look forward to more adventures in the future. To all of my San Francisco friends outside of BMS, they also know who they are, and I am equally indebted for their love and support.

The biggest challenge of leaving Seattle was being away from my family and friends. I have been extremely fortunate to have a big family, and with each family member, associated friends and loved ones. There are too many names to list on this page, but to each and every one of my family and friends, I thank them from the bottom of my heart for making me the person I am today, and for their unwavering support. I must, however, acknowledge my brothers Luke Camarda and Giancarlo Martino. I have missed them dearly, but knowing that these two have had my back since the day I was born has given me all the strength in the world. Finally, to my mother, Lily, and my late grandmother, Margaret, there are no words to describe how thankful I am for both of

them. They gave me the confidence and persistence I needed at every step of my life, and everything I do is in their honor.

Last, and certainly not least, I must thank my wife Krystal Fontaine. She has been, and always will be, the inspiration and role model of my life. As a scientist, her attention to detail and commitment to rigor is staggering. As a daughter and friend, her heart knows no bounds. I cannot express how fortunate I am to have Krystal as a life partner. She is my best friend, and I will never stop trying to make her proud of me. Finally, there is no Krystal without our tiny girl-kitten Stella. She has been the first thing I see when I wake up (because she's standing on my chest meowing at my face) nearly every day for the past four years, and I wouldn't have it any other way. Stella, I love you.

Chapter 1 is reprinted largely as it appears in:

Camarda R., Williams J., and Goga A. In vivo reprogramming of cancer metabolism by MYC. Frontiers in Cell and Developmental Biology 5:35. doi:10.3389/fcell.2017.00035.

Chapter 2 is reprinted largely as it appears in:

Camarda R., Zhou A.Y., Balakrishnan S., Kohnz R.A., Mahieu C., Anderton B., Eyob H., Kajimura S., Tward A., Krings G., Nomura D.K., and Goga A. Inhibition of fatty acid oxidation as a therapy for MYC-overexpressing triple-negative breast cancer. Nature Medicine doi:10.1038/nm.4055.

Chapter 3 is reprinted largely as it appears in:

Camarda R., Williams J., Malkov S., Zimmerman L.J., Manning S., Aran D., Beardsley A., Van de Mark D., Chen Y., Berdan C.A., Louie S.M., Mahieu C., Winkler J., Willey E., Gagnon J.D., Shinoda K., Ansel K.M., Werb Z., Nomura D.K., Kajimura S., Butte A.J., Sanders M.E., Liebler D.C., Rugo H., Krings G., Shepherd J.A., and Goga A. Tumor cell-adipocyte gap junctions activate lipolysis and are essential for breast tumorigenesis. bioRxiv doi: https://doi.org/10.1101/277939.

Metabolic requirements necessitate microenvironmental crosstalk in breast cancer

Roman Camarda

Abstract

Despite marked advancements in targeted therapeutics, breast cancer remains the most diagnosed cancer and second leading cause of cancer-related death in women in the United States. The triple-negative subtype of breast cancer (TNBC), which lacks expression of the estrogen, progesterone and human epidermal growth factor 2 receptors, has the highest proliferative and metastatic indices, and there are no TNBC-specific therapies available in the clinic. Expression of the oncogenic transcription factor MYC is elevated in TNBC. By its nature as a transcription factor, it is challenging to drug MYC directly. An alternative strategy is a synthetic lethal approach in which pathways are identified that are essential for MYC-overexpressing tumor cells, but not normal cells. It has been shown that MYC alters metabolism during tumorigenesis, however, its role in TNBC metabolism remains largely unexplored. In addition, previous studies have largely been conducted in vitro, which may not recapitulate metabolism found in vivo.

From targeted metabolomics on a transgenic mouse model of MYC-overexpressing TNBC and RNA expression analysis of primary TNBC samples from The Cancer Genome Atlas (TCGA), I identified fatty acid oxidation (FAO) as dysregulated in TNBC. Using a variety of models, I demonstrated that MYC-overexpressing TNBC has an increased bioenergetic reliance on FAO, and that inhibition of FAO abrogates tumor growth. Given the interface that exists between

cancer cells and adipocytes in the breast, I examined whether tumor-adjacent adipose tissue could be a source of fatty acids that fuel tumorigenesis. Studying tumors and adjacent tissue from patient cohorts and mouse models, I found that lipolysis is hyperactivated in breast tumor-adjacent adipocytes. I investigated the tumor-adipocyte interface and found that gap junctions form between breast cancer cells and adipocytes that transfer cAMP, a lipolysis-inducing signaling molecule, from tumor cells to adipocytes. In addition, tumor-adipocyte gap junction formation requires connexin 31 (Cx31), the most upregulated connexin in the TCGA TNBC cohort, and Cx31 is essential for tumor growth and activation of lipolysis. Thus, I have identified FAO and tumor cell-adipocyte gap junctions as critical elements of TNBC tumorigenesis that may serve as new therapeutic targets to treat this aggressive subset of breast cancer.

Table of contents

List of tables

Chapter 1

Chapter 2

Chapter 3

List of figures

Chapter 1

Chapter 2

Chapter 3

Chapter 1

In vivo reprogramming of cancer metabolism by MYC

Summary

The past few decades have welcomed tremendous advancements towards understanding the functional significance of altered metabolism during tumorigenesis. However, many conclusions drawn from studies of cancer cells in a dish (i.e. in vitro) have been put into question as multiple lines of evidence have demonstrated that the metabolism of cells can differ significantly from that of primary tumors (in vivo). This realization, along with the need to identify tissue-specific vulnerabilities of driver oncogenes, has led to an increased focus on oncogene-dependent metabolic programming in vivo. The oncogene c-MYC (MYC) is overexpressed in a wide variety of human cancers, and while its ability to alter cellular metabolism is well established, translating the metabolic requirements and vulnerabilities of MYC-driven cancers to the clinic has been hindered by disparate findings from in vitro and in vivo models. This review will provide an overview of the in vivo strategies, mechanisms and conclusions generated thus far by studying MYC's regulation of metabolism in various cancer models.

Introduction

Cancer is a disease of uncontrolled growth, and proliferating cells change their metabolic demands compared to quiescent cells[1,2]. Tumor cells can outcompete normal cells, regardless of the proliferative capacity of the tissue of origin. Dysregulated metabolism is a hallmark of tumorigenesis,[3] and such altered metabolism permits tumor cells to survive and proliferate despite adverse conditions.

Historical studies of altered metabolism in cancer pointed to increased glycolysis, and later glutaminolysis, as defining characteristic of tumor cells. Significant progress has been made studying glycolysis and glutaminolysis, and therapeutic targeting of these pathways is actively being pursued in the clinic[4,5]. However, it has become increasingly apparent that while glycolysis and glutaminolysis certainly play major roles in some tumors[4,5], alternative sources of "fuel" can be just as, if not more, important[6]. Notably, targeting of alternative metabolic pathways, for example lipid biosynthesis, is currently in clinical trials against a variety of tumor types, and cannot be undervalued[7].

A critical link between understanding cancer metabolism and targeting it therapeutically is identifying the upstream effectors that reshape tumor metabolism. The proto-oncogene MYC is a pleiotropic transcription factor and is one of the most commonly amplified or overexpressed genes in human cancers[8]. While MYC expression is dysregulated in a wide variety of cancers, its oncogenic role has most thoroughly been studied in vivo in the context of transgenic models of aggressive breast, liver, lung, prostate, and kidney cancers, as well as neuroblastoma and lymphoma (see references below; Figure 1 and Table 1). For example, we and others have demonstrated that MYC expression is elevated in the estrogen, progesterone and

human epidermal growth factor receptor-2 (HER2), receptor triple-negative subtype of breast cancer (TNBC)[9,10]. Additionally, MYC translocation to the IgG locus plays a causal role in Burkitt's Lymphoma[8,11]. As a transcription factor, MYC's primary mode of transformation is through the pro-tumorigenic transcriptional dysregulation of a wide variety of processes including proliferation, cell size, apoptosis, and metabolism[8]. Regulation of MYC's transcriptional activity[12], and the role of MYC's transcriptional binding partners in the regulation of metabolism[13] have been studied and reviewed, and will not be discussed here. It is also important to note that given the broadly important role of MYC in cancer, a direct MYC inhibitor could be of great clinical utility. However, such an inhibitor has yet to be created, and the strategy of targeting MYC directly remains challenging[14,15]. Thus, alternative strategies of targeting MYC-driven cancers via selective inhibition of cellular pathways, like metabolism, that may selectively kill MYC-overexpressing cells have attractive therapeutic potential. Indeed, the concept of specifically targeting metabolism to induce synthetic lethality in a MYC-dependent manner was pioneered by Shim et al[16], and expanded upon by many others[17,18].

The ability of MYC to dynamically regulate cellular metabolism in cancer is well established[19,20]. However, it is important to note that many studies describing MYC's ability to reprogram tumor cell metabolism have been conducted in vitro, primarily using inducible/repressible transgenic and human cancer cell line models[19,20]. While the importance and utility of in vitro cell culture models is undeniable, results from these models must be considered with caution when studying a process such as metabolism that is dependent on tumor cell environment[21]. Further, the dynamic nature of metabolic stressors and plasticity in vivo is difficult to model in vitro, particularly en masse. Primary

tumors develop to form a complex tissue that is exposed to varying levels of oxygenation, and fluctuating concentrations of glucose, glutamine, amino acids and countless other metabolites that cannot be readily modelled in tissue culture[21]. Recent studies have also revealed an intimate connection between circadian rhythms and tissue-specific metabolism that has yet to be fully considered in the context of cancer metabolism[22]. This last point is particularly prescient given the recent demonstration by Altman et al that MYC itself can dysregulate circadian gene expression and metabolism[23], however, these findings have yet to be validated in vivo.

The disparate nature of in vitro and in vivo metabolism is exemplified by a recent study that took advantage of two transgenic mouse models of KRAS-driven non-small cell lung cancer (NSCLC)[24]. Davidson et al found that both models displayed increased utilization of glucose-derived carbon to fuel the tricarboxylic acid (TCA) cycle compared to normal lung in vivo, while neither tumor nor non-tumor utilized glutamine-derived carbon for the TCA cycle to a large extent. This is in stark contrast to a cell line derived from one of the transgenic models, which in vitro decreases its utilization of glucose for the TCA cycle and increases its utilization of glutamine to that end[24]. Thus, glutamine oxidation in this model system appears to be an artifact of the in vitro culture methods and is not observed in vivo. Such results thus raise doubt about the utility of targeting the glutamine pathway as a therapeutic target for primary KRAS-driven lung tumors.

Given the dynamic nature of MYC's function in diverse cellular contexts, and the potential for cell culture to confound our understanding of tumor metabolism, the goal of this review is to focus on the regulation of cancer metabolism by MYC in vivo. To clarify, our definition of in vivo refers to studies of metabolism with findings based on de novo

MYC-driven tumorigenesis, usually in the form of transgenic mouse models. While we acknowledge that many findings from in vitro studies of MYC-driven cancer metabolism hold true in vivo[19,20], we will discuss here the various models used to study the regulation of cancer metabolism by MYC in vivo (summarized in Table 1), and provide broader context on some of the questions that remain to be answered.

Use of transgenic mouse models and consideration of tissue-specific effects

The study of cancer metabolism in vivo is of course limited by the methods and unique challenges and considerations that the metabolism of complex tissues warrants[21]. One particularly important consideration is the difference between "snap-shot" strategies of studying metabolism versus kinetic flux analyses, and how the use of chemically labelled metabolites factors into both approaches. The most common snap-shot method for studying metabolism is mass spectrometry-based metabolomics, which can be "targeted" for known metabolites or "untargeted" for unbiased detection of all metabolites present within a particular sample, and does not require any labelled metabolite[25]. A second snap-shot strategy is ^{13}C tracer analysis, in which a ^{13}C-labelled metabolite is infused or fed to the subject, and mass spectrometry is used to identify downstream metabolite labelling patterns[26]. The use of ^{13}C-labelled metabolites shifts from a snap-shot tracing study to a formal kinetic flux analysis when a much more complex series of considerations (metabolite uptake and secretion, as well as the kinetics of the biochemical reaction network to be probed) are taken into account[26]. A common approach to achieve flux analysis is with constant infusion of an isotopically labelled tracer, ^{13}C-glucose for example, that will achieve isotopic steady state as ^{13}C enrichment becomes stable over time[26]. Understanding the differences between these methods, and the conclusions that can be drawn from them, is vital. In particular, snap-shot metabolomics is often used to prematurely draw conclusions about the activity of a metabolic pathway, when the elevation or decrease of a particular metabolite does not necessarily reflect activation or inhibition of an entire pathway[25,26]. Moreover, interpretation and validation of metabolic data is critical, as for example, accumulation of

a particular metabolite could have multiple potential interpretations (i.e. increased activity of an upstream anabolic pathway or decreased activity of a downstream catabolic pathway). An important caveat to the study of in vivo metabolism is that tumor tissue is often analyzed at a bulk level, and as the work of Aran et al and many others has demonstrated, the composition of solid tumors includes a number of different cell types[27] whose metabolism is rarely accounted for in such bulk analyses.

With a cadre of strategies in hand, the study of cancer metabolism in vivo then becomes a function of the models or the clinical samples available for analysis. In this section, we will address some of the most thoroughly used models to study the metabolism of MYC-driven cancer (Table 1). The overall message is that while MYC-driven metabolism during tumorigenesis is quite tissue-specific, some shared pathways also emerge (Figure 1).

MYC dysregulates glucose and glutamine metabolism

In hepatocellular carcinoma (HCC), MYC is found to be frequently amplified and/or overexpressed, and is associated with poorly differentiated tumors and poor prognosis[28–32]. In addition, MYC expression is commonly found to be upregulated in hepatoblastoma (HB), a liver tumor type that predominates in pediatric patients[33].

To study MYC-dependent metabolism in HCC, we and others have utilized the MYC-driven LAP-tTA/TRE-MYC (LT2-MYC) transgenic mouse model of liver cancer initially developed in the lab of J.M. Bishop, which allows for MYC overexpression specifically in hepatocytes in the absence of doxycycline[28]. Importantly, mRNA expression analysis reveals that LT2-MYC tumors effectively model poorly differentiated, aggressive liver cancer[29]. Using this model, we probed for changes in glycolytic metabolism using hyperpolarized ^{13}C-pyruvate magnetic resonance spectroscopic imaging (MRSI) during de novo tumorigenesis and inducible tumor regression. More specifically, hyperpolarized ^{13}C-pyruvate MRSI allows for in vivo flux analysis of pyruvate to lactate and/or alanine conversion. With this modality, we found that MYC induction led to increased pyruvate to alanine conversion in the liver that preceded overt tumor formation, while full-blown tumors displayed increased pyruvate to lactate conversion. Both of these phenotypes were reversed during tumor regression. Mechanistically, mRNA expression analysis revealed coordinate changes in the levels of TCA cycle and glycolytic enzymes that supported the observed metabolic changes. In particular, there was a specific elevation of glutamate pyruvate transaminase 1, which converts pyruvate to alanine, in pre-tumorigenic liver, while lactate dehydrogenase A (LDHA), which converts pyruvate to lactate, was specifically upregulated in tumors[34].

Studies such as this indicate that imaging of downstream glycolysis pathway events can identify the earliest stages of tumor formation and regression and that these metabolic changes are indeed MYC dependent.

The notion that MYC drives increased glycolysis in liver cancer was further bolstered by a parallel study of MYC-driven metabolism using the same LT2-MYC model. Yuneva et al utilized a combination of steady-state profiling techniques including nuclear magnetic resonance spectroscopy with or without ^{13}C-glucose and ^{13}C-glutamine labeling, as well as ^{18}F-fluorodeoxyglucose positron emission tomography and mass spectrometry[35]. The authors found that MYC-driven liver tumors displayed increased glucose uptake and catabolism to lactate and TCA cycle intermediates, as well as increased glutamine catabolism to support the TCA cycle. These findings were supported by increased expression of LDHA, hexokinase 2 (Hk2), and glutaminase 1 (Gls1), and decreased expression of glutamine synthetase (Glul). The importance of glutamine catabolism in MYC-driven HCC was further demonstrated by Xiang et al who demonstrated that genetic ablation of one copy of Gls1 or treatment with two different inhibitors of Gls1 could significantly prolong survival in this same model[36]. This was in direct contrast to glucose and glutamine utilization in transgenic MYC-driven lung tumors[37,38]. Unlike MYC-driven liver tumors, MYC-driven lung tumors displayed elevated lactate and glutamine levels, which was suggestive of increased glucose catabolism, but not glutamine catabolism. MYC-driven lung tumors displayed increased LDHA, Hk2, Gls1 as well as Glul. Likewise, a similar model of transgenic MYC-driven lung cancer displayed increased LDHA and Hk2, as well as enzymes from several other metabolic pathways, at the mRNA level[39].

Although MYC pathway activation is elevated in the majority of renal cell carcinoma (RCC) cases, a formal study of MYC's role in the pathogenesis and the metabolism of RCC had been lacking. To study MYC in RCC, Shroff et al created an inducible transgenic model of renal cell carcinoma (GGT-tTA/TRE-MYC) in which MYC is specifically overexpressed in the kidney in the absence of doxycycline[40]. Using desorption electrospray ionization mass spectrometry imaging (DESI-MSI), the authors studied the metabolic profiles of non-tumor kidney, MYC-driven kidney tumors at 2 and 4 weeks post MYC induction, and regressed tumors after 4 weeks of switching MYC off. The authors noted multiple metabolic changes, including in the relative abundance of a variety of long-chain fatty acids in tumors compared to non-tumor kidneys and regressed tumors. Schroff and colleagues focused on glutamine metabolism after mRNA expression analysis revealed a downregulation in many glycolytic genes, but an upregulation in genes associated with glutaminolysis. The authors confirmed that glutamate and TCA cycle intermediates were elevated in tumors using DESI-MSI, and found that their transgenic tumors, as well as MYC^{high} human RCC, stained positively for Gls1 and Gls2, suggesting an elevation in glutaminolysis. Decreased staining of the transgenic tumors for Hk1 and LDHA further supported diminished glycolysis. Finally, the authors found that pharmacological inhibition of Gls1 with bis-2-(5-phenylacetamido-1,2,4-thiadiazol-2-yl) ethyl sulfide (BPTES) abrogated the growth of MYC-driven kidney tumors[40], implicating glutamine utilization as critical for MYC-driven RCCs, similar to what was found in MYC-driven HCC[36].

Additional evidence that MYC dysregulates glutamine metabolism was provided by a recent study that found elevation of the glutamine synthetase (Glul) enzyme and

glutamine abundance in a transgenic mouse model of dual MYC and KRAS-driven pancreatic cancer, compared to tumors driven by KRAS alone[41]. These studies suggested Glul is induced by MYC. Further support that MYC dysregulates glucose metabolism was provided when mass spectrometry-based metabolomic analysis was used to compare the metabolic profiles of established transgenic mouse models of MYC- or AKT-driven prostate cancer[42,43], as well as human prostate cancer samples that had been profiled for activated phospho-AKT and MYC levels. The authors found coordinately decreases in glucose-related metabolites and downregulation of HK2 and the glucose transporter GLUT-1 in mouse and human prostate tumors that were MYC^{high}, compared to control tissue and AKT^{high} tumors. In addition, the authors found specific dysregulation of several long-chain fatty acids in MYC^{high} tumors, but the functional significance of these changes was not addressed[44].

In summary, the ability of MYC to alter glucose and glutamine metabolism in cancer is clear. However, the studies of MYC-driven liver, lung, kidney, pancreatic and prostate cancers studied above highlight the fact that MYC can up- or downregulate either or both of these pathways depending on tissue context. Furthermore, Shroff et al were the only group to formally demonstrate that dysregulation of one of these pathways leads to a reliance upon it that may have therapeutic potential[40]. Further studies in the remaining cancer types discussed above will be necessary to determine if targeting glucose or glutamine metabolism will have therapeutic utility.

MYC regulates downstream glutamine utilization

Although the LT2-MYC model had multiple changes in glucose and glutamine metabolism[34,35], other metabolic pathways had not been fully explored. Using the conditional MYC-driven liver cancer model we conducted global mRNA expression and mass spectrometry-based metabolomic analyses on LT2-MYC tumors versus control uninduced transgenic livers[30]. Using an integrated bioinformatics approach, we probed for metabolic pathways coordinately dysregulated in both transcript and metabolite levels. Of the six pathways identified: glutathione metabolism; glycine, serine, and threonine metabolism; aminoacyl-tRNA biosynthesis; cysteine and methionine metabolism; ABC transporters; and mineral absorption, we focused on glutathione metabolism[30]. We found a marked decrease in the reduced and oxidized form of glutathione, as well as the enzyme responsible for de novo glutathione biosynthesis, glutamate-cysteine ligase, catalytic subunit (GCLC). Because glutathione is synthesized downstream of glutamine conversion to glutamate, we performed mass spectrometry-based tracing analysis with ^{13}C-glutamine in a somatic transgenic model of MYC-driven liver cancer[45]. We found that glutamine-derived carbons preferentially fueled the TCA cycle versus glutathione production in MYC-driven liver tumors compared to control liver tissue. Mechanistically, we found that GCLC expression was downregulated by miR-18a in a MYC-dependent manner. Treatment of LT2-MYC tumor-bearing mice with a locked-nucleic acid antagonist of miR-18a significantly rescued GCLC expression and glutathione levels in vivo. In addition, miR-18a was significantly elevated in human HCC compared to non-tumor liver, was negatively correlated with GCLC expression in human HCC, and was positively correlated with alpha-fetoprotein (AFP) expression, which is

associated with aggressive liver cancer. Finally, we found that LT2-MYC tumors displayed increased sensitivity to an oxidative stress inducer, diquat, compared to non-tumor liver. In particular, diquat-treated tumors displayed a specific and significant increase in cell loss, TUNEL staining as a marker of apoptosis, and decreased MYC expression[30]. Notably, it had been previously demonstrated in vitro that MYC-dependent suppression of miR-23a/b results in increased Gls1 and glutaminolysis activity[46,47]. Thus, MYC can alter the expression of specific miRNAs (i.e. miR18a and miR23a) which in turn regulate glutamine metabolism. MYC-dependent regulation of miRNAs may be a common mechanism through which MYC reprograms tumor metabolism (Figure 2) and deserves broader consideration beyond HCC.

In neuroblastoma, the MYC-related transcription factor MYCN is found to be amplified in ~20% of neuroblastomas, and its amplification is associated with poor prognosis[48]. To study the role of MYCN in neuroblastoma metabolism, Carter & Sutton et al utilized the TH-MYCN transgenic model of MYCN-driven neuroblastoma in which MYCN is overexpressed in cells of the neural crest[49]. Using mass spectrometry-based metabolomics, the authors performed global metabolic profiling of MYCN-driven neuroblastoma at multiple time-points representing hyperplastic ganglia, early tumors, and advanced tumors. Grouping the metabolomic data into pathway analysis, it was found that glutathione metabolism was the most significantly dysregulated pathway, with all metabolites associated with glutathione biosynthesis elevated in MYCN-driven tumors compared to control ganglia. Interestingly, the majority of enzymes associated with glutathione biosynthesis, including GCLC, were found to be downregulated at the mRNA level. Therefore, the authors speculated that increased protein biosynthesis,

which was evidenced by a significant increase in the expression of ribosome biogenesis genes, was responsible for the observed increase in glutathione, although this contention was not formally tested. Regardless, the increase in glutathione led the authors to hypothesize that MYCN-driven neuroblastoma could have an increased dependence upon glutathione metabolism. Indeed, the authors found that BSO, an inhibitor of GCLC, could reduce sympathetic ganglia hyperplasia and delay tumor onset when given prophylactically. In addition, GCLC inhibitors did not have an effect on the growth of established tumors when given alone, but did have a significant benefit when given with the clinically relevant chemotherapeutic agent vincristine, compared to BSO alone or vincristine alone[48]. Thus, in both MYC driven liver and neuroblastoma models GCLC expression is suppressed, though the effects on glutathione production appear to be contextually dependent. We postulate that in the setting of low GCLC expression, and consequently low GSH production that some MYC-driven tumors, such as liver cancers, may be especially sensitive to exogenous oxidative stress[30].

Terunuma et al conducted mass spectrometry-based metabolomics on primary breast cancer samples and adjacent non-tumor tissue[50]. The authors found a number of differences in metabolite abundance between tumor and non-tumor samples, and probed further into the differences between ER-positive and ER-negative tumors as well as tumors from individuals with African ancestry versus European ancestry. The authors chose to focus on 2-hydroxyglutarate (2-HG), a known “oncometabolite,” which was found to be preferentially elevated in ER-negative tumors. Interestingly, 2-HG accumulation normally occurs in the context of isocitrate dehydrogenase (IDH) 1 or 2 mutation, but the authors did not find evidence of IDH mutation in breast cancer. It was

recently demonstrated that 2-HG can be produced via LDHA in the context of hypoxia[51,52], but Terunuma et al did not address whether hyoxia could explain 2-HG production in the breast tumors analyzed. However, they did find a strong correlation between 2-HG levels, MYC pathway activity, glutaminolysis-associated metabolites, and Gls1 expression. Further, the authors provided in vitro evidence that 2-HG production occurs during glutamine catabolism, and that MYC is both necessary and sufficient for elevated 2-HG levels[50] in breast cell lines. These data suggest that MYC, albeit via a yet unclear mechanism, is able to promote glutamine utilization for 2-HG production in cancer. It is of course tempting to speculate that MYC-dependent regulation of LDHA, as discussed above, may contribute to the 2-HG production observed, but this remains to be determined.

In summary, MYC's regulation of glutamine metabolism is extensive. In the case of glutathione, relative decreases[30] and increases[48] were observed depending on the cancer type. With a decrease, tumors were found to be sensitive to an inducer of oxidative stress[30], while an increase led the tumors to be sensitive to GCLC inhibition during the early phase of tumor formation[48]. Interestingly, in neuroblastoma the elevation of glutathione occurred despite a downregulation in GCLC mRNA levels. It would be interesting to determine if the decrease in GCLC observed in neuroblastoma is miR-18a-dependent. An alternative downstream use of glutamine to generate 2-HG has also been postulated in primary breast cancers. It remains unclear how MYC activity could induce 2-HG production, thus the therapeutic utility and potential to target this pathway have not been explored[50].

MYC dysregulates lipid metabolism

The role of MYC in HB metabolism has not been studied as extensively as HCC[53], but it is worth noting that a recent study performed global mRNA expression analysis in a somatic transgenic model of β-catenin/YAP-driven HB performed in mice with either MYC-wildtype (WT) or MYC-knockout (KO) hepatocytes. The authors found that MYC promoted tumor progression, but not initiation, and were able to identify several metabolic pathways with differential enzyme expression and pathway activity in MYC-WT vs MYC-KO tumors[33]. For example, MYC-KO tumors displayed reduced expression of the fatty acid transporter CD36, with a concomitant decrease in lipid droplet levels and fatty acid oxidation (FAO)[33]. Given these results in HB, it would be interesting to determine if MYC also dysregulated lipid metabolism in HCC. To that end, Perry et al utilized DESI-MSI to not only detect differential abundance of lipid species in non-tumor liver, early LT2-MYC tumors, late tumors, and regressed tumors, but also generate a spatial localization of the detected lipids with ~200μm resolution[54]. The authors found that a number of lipid species displayed differential abundance in tumor vs non-tumor tissue, but did not pursue the functional significance of these changes.

The work of Perry et al in MYC-driven liver cancer later led the same lab to use DESI-MSI to study MYC-driven lymphoma. MYC is known to be broadly dysregulated in aggressive lymphomas, and in Burkitt's lymphoma the MYC gene is translocated next to the immunoglobulin heavy chain enhancer in virtually all cases[8,11]. To study MYC-driven lymphoma Eberlin et al utilized the conditional Eμ-tTA/TRE-MYC transgenic mouse model in which MYC is specifically expressed in lymphocytes only in the absence of doxycycline[55]. The authors reported a number of lipids that displayed differential

abundance in MYC-driven lymphoma compared to control non-tumor thymus. In addition, the authors performed DESI-MSI on 15 human lymphoma samples, including 5 cases of Burkitt's lymphoma, that were profiled for MYC expression such that they were classified as MYC^{high} or MYC^{low}. Interestingly, there were many similarities between the lipid profiles of the mouse MYC-driven lymphomas and the human MYC^{high} lymphomas, and both were distinct from the human MYC^{low} lymphomas[11]. Interestingly, some of the most differentially increased lipids in MYC-driven lymphomas were multiple cardiolipin species, which are known to play critical roles in mitochondrial membrane integrity. Thus, although Eberlin et al did not pursue the functional significance of dysregulated lipid metabolism, these changes could support alternative aspects of MYC-driven metabolism in lymphoma. Additionally, it is interesting that Eberlin et al acknowledge in their discussion a potential relationship between altered lipid abundance and FAO, and a separate study indeed found that inhibition of FAO was able to significantly delay tumorigenesis in a constitutive model of transgenic MYC-driven lymphoma (Eμ-MYC)[56,57].

As mentioned above, we and others have demonstrated that MYC expression is disproportionately elevated in TNBC compared to receptor-positive (RP) tumors[9,10]. Thus, we were particularly interested in the use of the MYC-driven MMTV-rtTA/TRE-MYC (MTB-TOM) transgenic mouse model of breast cancer, in which MYC is overexpressed specifically in mammary epithelial cells in a doxycycline-inducible manner[58]. It is important to note that while MYC is certainly overexpressed in this model, which mimics the clinically observed increase in MYC expression in TNBC, it was also confirmed by unbiased clustering of mRNA expression analysis that the MTB-

TOM model does resemble the Basal/TN subtype of breast cancer[59]. Using this model, we performed steady-state metabolomics and ^{13}C-tracing analysis and found that FAO was dysregulated. We then used a ^{14}C-oleic acid oxidation assay to confirm that FAO was elevated specifically in MYC-overexpressing TNBC. Given the elevation in FAO, a pathway known to fuel the TCA cycle and ATP production, we hypothesized this pathway could be required to fuel bioenergetic metabolism in MYC-overexpressing TNBC, and could have therapeutic potential. To address this hypothesis in a more clinically relevant model, we utilized a recently described panel of breast cancer patient-derived xenografts (PDX)[60]. Using a specific inhibitor of the FAO pathway, etomoxir, we found that inhibition of FAO decreased bioenergetic metabolism and inhibited tumorigenesis in a MYC^{high} TN PDX, but did not inhibit tumorigenesis in a MYC^{low} TN PDX model[61]. Notably, a separate study found elevated FAO in TNBC, and described an additional downstream role for FAO in promoting autophosphorylation and activation of the oncogenic Src kinase[62]. It remains to be seen whether or not there is a functional interaction between MYC and Src in TNBC, and whether Src could be a mechanism of FAO upregulation in MYC-driven TNBC, or vice versa. In addition, as mentioned above, Terunuma et al found elevation of acyl-carnitines, the bottleneck intermediate of FAO, in ER-negative human tumors compared to ER-positive or non-tumor tissue[50], supporting our findings of dysregulated FAO in TNBC[61].

Although several studies have now indicated that MYC is capable of dysregulating lipid metabolism, and in particular FAO, no study has yet to validate a downstream mechanism by which MYC activation dysregulates lipid metabolism and/or FAO in vivo. It is worth noting that several potential mechanisms have been described

in vitro, including MYC-dependent induction of mitochondrial biogenesis[63], which has been functionally linked to FAO in the context of MYC inhibition[64]. In addition, there are several other hypotheses supported by the literature that are worth noting. First, we found a marked downregulation in acetyl-CoA carboxylase 2 (ACC2) protein expression in MYC^{high}, but not MYC^{low} PDXs, and it has been demonstrated that downregulation of ACC2 in transgenic mice is sufficient to upregulate FAO in vivo[65]. Second, fatty acid binding proteins (FABPs) are known to play a supporting role in fatty acid oxidation as they are responsible for trafficking fatty acids throughout the cell[66]. In ovarian cancer that metastasizes to the omentum it was demonstrated that FABP4 is upregulated in tumor cells and expressed in omental adipocytes, and is necessary in both cell types to support metastatic tumorigenesis[66]. Furthermore, FABP5 has been found to be upregulated in TNBC, and is associated with poor prognosis and recurrence-free survival in TNBC[67]. Thus, we postulate that MYC reprograms lipid metabolism in TNBCs via coordinated suppression of fatty acid synthesis and upregulation of oxidation to support tumor metabolic demands.

Finally, we and others recently described the necessity for PIM kinase activity in MYC-overexpressing TNBC[68,69]. PIM expression can promote PGC1α expression, a master regulator of FAO[70]. In addition, a recent study suggests that there may be functional redundancy between PIM and PI3K in breast cancer, and because PI3K is a known regulator of glycolysis, PIM may then play a role in regulation of glycolysis in MYC-overexpressing TNBC[71,72]. Further studies are necessary to determine which, if any, of these potential mechanisms are indeed at play in the regulation of FAO in MYC-overexpressing TNBC.

In summary, MYC is capable of dysregulating lipid metabolism in multiple cancer types, but a mechanism has yet to described. Given that our work found that inhibition of FAO is a therapeutic strategy against MYC-overexpressing TNBC[61], and a separate study found similar results in a model of MYC-driven lymphoma[57], it will be interesting to determine if this strategy could be expanded to MYC-driven HB and/or HCC.

Studies of protein and nucleotide metabolism in MYC-driven lymphoma

In addition to studies of lipid metabolism, the Eμ-MYC model has also been used for studies of protein and nucleotide metabolism. Eμ-MYC lymphomas display elevated protein translation, a common of feature of many cancer types[73]. Barna et al created a bi-allelic model in which haploinsufficiency of the ribosomal protein RPL24 results in reduced protein translation back to non-tumor levels. When this model was bred to the Eμ-MYC model it resulted in decreased tumorigenesis[73]. With this model, the same lab recently utilized NMR-based metabolomic analysis to profile changes in a number of metabolic pathways in non-tumor lymphocytes, pre-tumor MYC-driven lymphocytes, lymphocytes with reduced translation, MYC-driven lymphocytes with normalized translation, and tumorigenic MYC-driven lymphocytes. Cunningham et al found that the most notable translation-dependent difference detected was a reduction in nucleotide-related metabolites, specifically inosine monophosphate and adenosine mono-, di- and triphosphate. The authors then demonstrated that a single enzyme, phosphoribosyl-pyrophosphate synthetase 2 (PRPS2), is responsible for increased nucleotide metabolism in MYC-driven lymphoma via a cis-regulatory element in its 5' UTR that is activated by translation initiation factor eIF4E, which is itself hyperactivated in tumors. Additionally, MYC-driven lymphomagenesis is at least in part dependent upon PRPS2 as Eμ-MYC crossed with PRPS2-null mice have a significant delay in tumor initiation as well as a significant increase in survival[74]. Interestingly, elevated protein synthesis in this model has also been linked to increased activation of the unfolded protein response, which ultimately promotes tumor cell survival via autophagy[75]. Thus, a

combined increase in translation and autophagy may contribute to MYC-driven metabolic adaptation in lymphomas.

Regulation of MYC by metabolism

While MYC reprograms metabolism, there is also mounting evidence of metabolic regulation of MYC in cancer and tissue homeostasis. One notable example is the regulation of MYC protein levels by HMG-CoA reductase, which has been demonstrated in the Eμ-tTA/TRE-MYC model of lymphoma, as well as the LT2-MYC model of liver cancer [76,77]. Mechanistically, HMG-CoA reductase inhibition via atorvastatin reduced RAS and ERK1/2 signaling in lymphoma, resulting in decreased ERK-dependent MYC phosphorylation, and reduced MYC levels[76]. In liver cancer, however, atorvastatin was found to decrease MYC phosphorylation and protein levels downstream of Rac GTPase activity[77]. The broader implication of this finding is that a HMG-CoA reductase inhibitor such as atorvastatin deserves further consideration in MYC-overexpressing tumor types, and indeed atorvastatin did have anti-tumorigenic activity in the aforementioned models of MYC-driven liver cancer and lymphoma[76,77]. A second example is the regulation of MYC protein levels by the enzyme O-linked N-acetylglucosamine transferase (OGT), which catalyzes post-translational O-GlcNAcylation of proteins. This phenomenon was demonstrated in a transgenic mouse model of liver cancer with elevated OGT activity[78]. Interestingly, it has been previously demonstrated that MYC can be glycosylated on threonine 58, a key regulatory residue that is also phosphorylated, but the functional significance of this modification remains to be elucidated[79].

Studying MYC and metabolism in human patients

While transgenic and PDX mouse models are invaluable in studying the role of MYC in cancer metabolism, the ultimate goal of these studies is to translate the findings from mouse models to the clinic. The study of cancer metabolism in the clinic has actually been a common practice for more than two decades via the use of the glucose analogue ^{18}F-fluorodeoxyglucose (FDG)[80]. Specifically, intravenous injection of ^{18}F-FDG coupled with positron emission tomography (PET) allows for the imaging of a variety of tumor types, which preferentially take up glucose to a higher degree than most non-tumor tissues[80]. Upregulation of hexokinase, which is very likely a MYC transcriptional target in at least some tumor tissues given it's strong MYC-dependent regulation as discussed above and elsewhere[81], results in phosphorylation and trapping of the FDG probe in cancers[80]. Although ^{18}F-FDG-PET imaging has generally been used to detect tumors, recent advancements in our understanding of the biology of tumorigenesis have led to much more specific uses for ^{18}F-FDG-PET. For example, Palaskas et al reasoned that a correlation between the expression of some mRNAs and ^{18}F-FDG uptake may allow ^{18}F-FDG-PET to identify the driver oncogene(s) or oncogenic pathway(s) active in a patient's tumor. The authors integrated mRNA expression analysis and ^{18}F-FDG uptake from a panel of cancer cell lines and 18 patients with breast cancer. Gene set enrichment analysis revealed a number of upregulated molecular pathways in the cell lines and patients with higher ^{18}F-FDG uptake including, not surprisingly, glycolysis. The authors then probed further for associations between the ^{18}F-FDG signature and breast cancer subtypes and molecular drivers, and found that the ^{18}F-FDG signature correlated best with the TN/basal subtype and MYC-dependent transcriptional activity. In addition,

the authors retrospectively stained biopsies from the 18 breast cancer patients, and found a significant increase in MYC protein staining of the tumors with high ^{18}F-FDG uptake[82]. To our knowledge, further studies correlating MYC expression with ^{18}F-FDG uptake in human tumors have not been conducted, but should be of further consideration.

Although glucose uptake measurement via ^{18}F-FDG-PET is an invaluable clinical tool, some tumors are inherently ^{18}F-FDG-negative[80]. Likewise, some non-tumor tissues demonstrate high glucose ultilization (i.e. brain and liver), making discernment of tumors via ^{18}F-FDG-PET challenging. Thus, alternative metabolites with high avidity for certain tumor types are needed. To that end, preclinical studies have been performed in the MTB-TOM MYC-driven breast cancer model with ^{18}F-(2S,4R)4-fluoroglutamine[83], which could be useful in a number of MYC-driven tumors that upregulate glutaminolysis as discussed above. In addition, acetate was recently described by two studies as a critical carbon fuel for a variety of primary tumors and tumors that have metastasized to the brain[84,85]. The critical acetate oxidation enzyme in cancer appears to be the acetyl-CoA synthetase enzyme ACSS2, which was found to be essential for tumorigenesis in a MYC-driven model of liver cancer, and increased expression of ACSS2 was associated with poor prognosis in TNBC[84]. Notably, this study that focused on both primary brain tumors and tumors that metastasized to the brain. Four patients were infused with [1,2-^{13}C]acetate during surgical resection of their tumors. Post-operative NMR revealed de novo oxidation of acetate to fuel the TCA cycle[85]. Thus, acetate deserves broader consideration as a bioenergetics substrate in MYC-overexpressing tumors, both in terms of therapeutic targeting and for imaging purposes. Finally, hyperpolarized 1-^{13}C-

pyruvate MRSI has been used preclinically[34], but has also been adopted for imaging of patient tumors as part of a first-in-man clinical trial[86]. Indeed, there is clear interest and opportunity for this modality to enter the clinic, especially with expanded probes beyond 1-^{13}C-pyruvate, which so far has been the most well studied[87].

Finally, it is worth taking note of several studies that focused almost entirely on the analysis of clinical samples. Importantly, these studies did not make a functional connection between the metabolic phenotypes observed and MYC activity, even though MYC has established functional roles in the cancer types studied. For those interested, we refer to metabolic profiling performed on primary tumors and serum samples from patients with HCC[88,89], as well as breast cancer[90–92]. In addition, integrated metabolomic and proteomic analysis has been performed on primary RCC tumors[93].

Broader implications

In this review, we have focused on the role of MYC in regulating cancer metabolism in vivo. The majority of studies to date have used transgenic mouse models or primary tumors. Thus, there remains a tremendous amount of work to be done looking outside the confines of the primary tumor to the role of MYC in metastatic tumors, as well as cells within the microenvironment and non-adjacent normal tissue, both of which will ultimately have tremendous influence on which therapeutic strategies can be translated to the clinic. With respect to metastasis, we recently performed single-cell mRNA expression analysis on de novo low- and high-burden metastases from orthotopic TNBC PDXs and found that MYC expression was significantly elevated in high-burden metastases[94]. Given that cancer cell metabolism has been shown to change in metastasis initiating cells[95], when the metastatic cells are in circulation[96], and depending on which organ the metastatic tumor colonizes[97], further studies will need to determine whether the reliance on FAO, glucose, glutamine or other metabolites present in primary MYC-overexpressing TNBC is maintained in high-burden metastases.

Another aspect of the microenvironment that deserves significant consideration is the immune cell component. A recent study demonstrated that tumors with elevated glucose consumption effectively drain glucose from the microenvironment, resulting in decreased T-effector cell function, which also relies upon glucose oxidation[98]. Notably, one of the effectors used in this study to promote glycolysis in a tumor line that would otherwise succumb to T-effector surveillance was MYC[98]. Of course, T-effector cells are just one of a large number of immune cell types present in the tumor microenvironment,

and the metabolic reliance of each of them could be effected by either the tumor itself or therapies that specifically target metabolism. The metabolism of other non-tumor cell types beyond the immune compartment are also important to consider with respect to MYC. Indeed, a recent study demonstrated that mice heterozygous for MYC throughout their entire body are smaller, live longer, and are more metabolically active[99]. Thus, targeting MYC-dependent metabolism in cancer could likely impact MYC-dependent metabolism in non-tumor cell types.

Conclusion

In summary, the role of MYC in the regulation of cancer metabolism is as complex as the diverse functions of MYC itself. What becomes clear after considering the multitude of studies conducted is that the function of MYC, like other oncogenes such as KRAS, is incredibly tissue-specific. However, while the overall metabolic phenotype is usually tissue-specific, dysregulation of individual metabolic pathways are often conserved across tissues, and the combination of these considerations should inform treatment decisions. Cancer research seeks to develop better and potentially curative treatments for MYC driven tumors. Studies of specific oncogene-driven transgenic cancer models allow for discoveries of new metabolic pathways that are deregulated in primary tumors, which could not be otherwise identified in cultured cells. We anticipated that effectively translating findings from studying cancer metabolism and its regulation by oncogenes like MYC or KRAS to the clinic will be accelerated through our understanding of how these oncogenes affect tissue specific metabolism in vivo.

Acknowledgements

This material is based upon work supported by NIH R01-CA170447, and NIH U19 CA179512, UCSF Liver Center grant P30DK026743, a Lymphoma Scholar Award, CDMRP Breast Cancer Research Program (W81XWH-12-1-0272 and W81XWH-16-1-0603) (to A.G.) and the NIH F99CA212488 (to R.C.). The authors would also like to thank Dror Assa for providing the drawing in Figure 1. We apologize to our colleagues for omitting some studies of MYC's regulation of metabolism due to consideration of space.

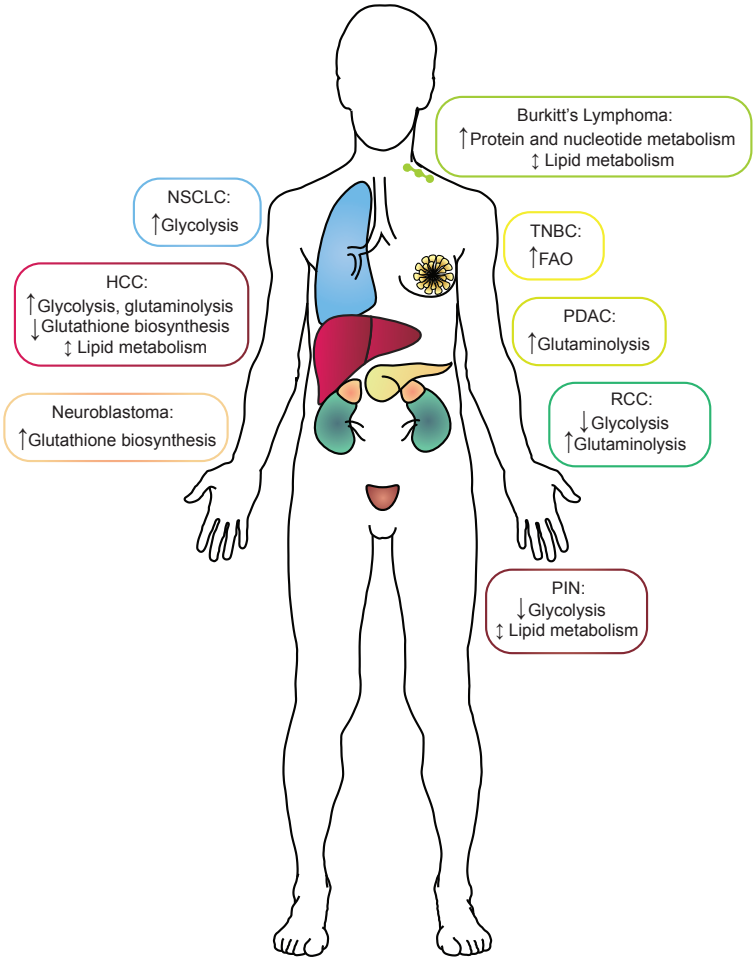

Figure 1: A summary of the metabolic alterations found in each MYC-driven cancer type by tissue of origin. Boxes surrounding each cancer indication are color-coded to match the tissue of origin. HCC, hepatocellular carcinoma; NSCLC, non-small-cell lung cancer; RCC, renal cell carcinoma; PDAC, pancreatic ductal adenocarcinoma; PIN, prostatic intraepithelial neoplasia; TNBC, triple-negative breast cancer.

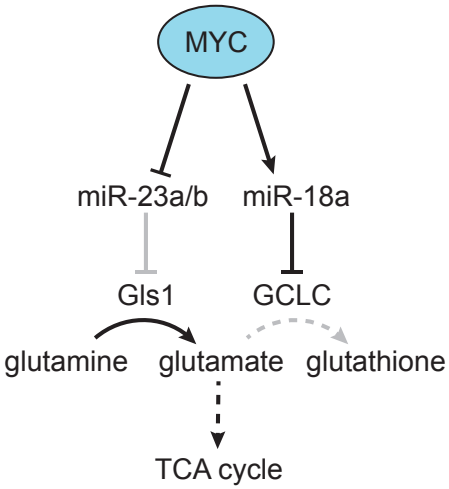

Figure 2: MYC-dependent miRNA regulation of glutamine metabolism. MYC was found to downregulate miR-23a/b, which targets Gls, resulting in increased production of glutamate from glutamine[46]. In addition, MYC was found to upregulate miR-18a, which targets GCLC, resulting in decreased production of glutathione from glutamate, and increased flow of glutamine-derived carbon into the TCA cycle[30]. Grey lines indicate a decreased effect, and dotted lines indicate a multi-step metabolic pathway.

Table 1: *In vivo* transgenic models of MYC-driven cancer (excluding hydrodynamic models)		
Tissue/cancer specificity	Model	MYC-dependent metabolic pathways altered
Liver - HCC	LAP-tTA/TRE-MYC	Glycolysis[25,26], glutaminolysis[26], glutathione biosynthesis[23], lipid metabolism[41]
Lung - NSCLC	SPC-rtTA/TRE-MYC	Glycolysis[26]
Kidney - RCC	GGT-tTA/TRE-MYC	Glycolysis[30], glutaminolysis[30]
Pancreatic - PDAC	Pdx1-Cre/LSL-KRASG12D/R26-LSL-MYC	Glutaminolysis[31]
Prostate - PIN	Pbsn-MYC	Glycolysis[34], lipid metabolism[34]
Neural crest - NB	TH-MYCN	Glutathione biosynthesis[38]
Lymphocytes - BL	Eμ-tTA/TRE-MYC Eμ-MYC/RPL24$^{+/-}$	Lipid metabolism[11] Protein metabolism[58], nucleotide metabolism[59]
Breast - TNBC	MMTV-rtTA/TRE-MYC	Fatty acid oxidation[48]

Table 1: A summary of the transgenic mouse models used thus far to study MYC-driven cancer metabolism in vivo. The tissue of origin, specific transgenes and primary altered metabolic pathway(s) studied in each model are noted. References for the models can be found in the main text. HCC, hepatocellular carcinoma; NSCLC, non-small-cell lung cancer; RCC, renal cell carcinoma; PDAC, pancreatic ductal adenocarcinoma; PIN, prostatic intraepithelial neoplasia; NB, neuroblastoma; BL, Burkitt's lymphoma; TNBC, triple-negative breast cancer.

References

1. Vander Heiden, M. G., Cantley, L. C. & Thompson, C. B. Understanding the Warburg effect: the metabolic requirements of cell proliferation. *Science* 324, 1029–33 (2009).
2. DeBerardinis, R. J., Lum, J. J., Hatzivassiliou, G. & Thompson, C. B. The Biology of Cancer: Metabolic Reprogramming Fuels Cell Growth and Proliferation. *Cell Metab.* 7, 11–20 (2008).
3. Hanahan, D. & Weinberg, R. a. Hallmarks of cancer: The next generation. *Cell* 144, 646–674 (2011).
4. Hay, N. Reprogramming glucose metabolism in cancer: can it be exploited for cancer therapy? *Nat. Rev. Cancer* 16, 1–15 (2016).
5. Altman, B. J., Stine, Z. E. & Dang, C. V. From Krebs to clinic: glutamine metabolism to cancer therapy. *Nat. Rev. Cancer* 16, 619–634 (2016).
6. Cairns, R. A. & Mak, T. W. The current state of cancer metabolism. *Nat. Rev. Cancer* 16, 613–614 (2016).
7. Galluzzi, L., Kepp, O., Vander Heiden, M. G. & Kroemer, G. Metabolic targets for cancer therapy. *Nat Rev Drug Discov* 12, 829–846 (2013).
8. Meyer, N. & Penn, L. Z. Reflecting on 25 years with MYC. *Nat. Rev. Cancer* 8, 976–990 (2008).
9. Horiuchi, D., Kusdra, L., Huskey, N. E., Chandriani, S., Lenburg, M. E., Gonzalez-Angulo, a. M., Creasman, K. J., Bazarov, a. V., Smyth, J. W., Davis, S. E., Yaswen, P., Mills, G. B., Esserman, L. J. & Goga, a. MYC pathway activation in triple-negative breast cancer is synthetic lethal with CDK inhibition. *J. Exp. Med.*

209, 679–696 (2012).

10. Koboldt, D. C., Fulton, R. S., McLellan, M. D., Schmidt, H., Kalicki-Veizer, J., McMichael, J. F., Fulton, L. L., Palchik, J. D., *et al.* Comprehensive molecular portraits of human breast tumours. *Nature* 490, 61–70 (2012).
11. Eberlin, L. S., Gabay, M., Fan, A. C., Gouw, A. M., Tibshirani, R. J., Felsher, D. W. & Zare, R. N. Alteration of the lipid profile in lymphomas induced by MYC overexpression. *Proc. Natl. Acad. Sci. U. S. A.* 111, 10450–5 (2014).
12. Kress, T. R., Sabò, A. & Amati, B. MYC: connecting selective transcriptional control to global RNA production. *Nat. Rev. Cancer* 15, 593–607 (2015).
13. Sloan, E. J. & Ayer, D. E. Myc, Mondo, and Metabolism. *Genes Cancer* 1, 587–596 (2010).
14. McKeown, M. R. & Bradner, J. E. Therapeutic Strategies to Inhibit MYC. *Cold Spring Harb. Perspect. Med.* 4, a014266–a014266 (2014).
15. Lockwood, W. W., Zejnullahu, K., Bradner, J. E. & Varmus, H. Sensitivity of human lung adenocarcinoma cell lines to targeted inhibition of BET epigenetic signaling proteins. *Proc. Natl. Acad. Sci.* 109, 19408–13 (2012).
16. Shim, H., Dolde, C., Lewis, B. C., Wu, C. S., Dang, G., Jungmann, R. A., Dalla-Favera, R. & Dang, C. V. c-Myc transactivation of LDH-A: implications for tumor metabolism and growth. *Proc. Natl. Acad. Sci. U. S. A.* 94, 6658–63 (1997).
17. Yuneva, M., Zamboni, N., Oefner, P., Sachidanandam, R. & Lazebnik, Y. Deficiency in glutamine but not glucose induces MYC-dependent apoptosis in human cells. *J. Cell Biol.* 178, 93–105 (2007).
18. Dang, C. V. Therapeutic targeting of Myc-reprogrammed cancer cell metabolism.

Cold Spring Harb. Symp. Quant. Biol. 76, 369–374 (2011).

19. Stine, Z. E., Walton, Z. E., Altman, B. J., Hsieh, A. L. & Dang, C. V. MYC, metabolism, and cancer. *Cancer Discov.* 5, 1024–1039 (2015).
20. Wahlström, T. & Henriksson, M. A. Impact of MYC in regulation of tumor cell metabolism. *Biochim. Biophys. Acta* (2014). doi:10.1016/j.bbagrm.2014.07.004
21. Mayers, J. R. & Heiden, M. G. Vander. Famine versus feast : understanding the metabolism of tumors in vivo. *Trends Biochem. Sci.* 40, 1–11 (2015).
22. Abbondante, S., Eckel-Mahan, K. L., Ceglia, N. J., Baldi, P. & Sassone-Corsi, P. Comparative circadian metabolomics reveal differential effects of nutritional challenge in the Serum and Liver. *J. Biol. Chem.* 291, 2812–2828 (2016).
23. Altman, B. J., Hsieh, A. L., Sengupta, A., Krishnanaiah, S. Y., Stine, Z. E., Walton, Z. E., Gouw, A. M., Venkataraman, A., Li, B., Goraksha-Hicks, P., Diskin, S. J., Bellovin, D. I., Simon, M. C., Rathmell, J. C., Lazar, M. A., Maris, J. M., Felsher, D. W., Hogenesch, J. B., Weljie, A. M. & Dang, C. V. MYC Disrupts the Circadian Clock and Metabolism in Cancer Cells. *Cell Metab.* 22, 1009–1019 (2015).
24. Davidson, S. M., Papagiannakopoulos, T., Olenchock, B. A., Heyman, J. E., Keibler, M. A., Luengo, A., Bauer, M. R., Jha, A. K., O'Brien, J. P., Pierce, K. A., Gui, D. Y., Sullivan, L. B., Wasylenko, T. M., Subbaraj, L., Chin, C. R., Stephanopolous, G., Mott, B. T., Jacks, T., Clish, C. B. & Van Der Heiden, M. G. Environment impacts the metabolic dependencies of ras-driven non-small cell lung cancer. *Cell Metab.* 23, 517–528 (2016).
25. Medina-Cleghorn, D. & Nomura, D. K. Exploring metabolic pathways and regulation through functional chemoproteomic and metabolomic platforms. *Chem.*

Biol. 21, 1171–1184 (2014).

26. Buescher, J. M., Antoniewicz, M. R., Boros, L. G., Burgess, S. C., Brunengraber, H., Clish, C. B., DeBerardinis, R. J., Feron, O., Frezza, C., Ghesquiere, B., Gottlieb, E., Hiller, K., Jones, R. G., Kamphorst, J. J., Kibbey, R. G., Kimmelman, A. C., Locasale, J. W., Lunt, S. Y., Maddocks, O. D. K., Malloy, C., Metallo, C. M., Meuillet, E. J., Munger, J., N??h, K., Rabinowitz, J. D., Ralser, M., Sauer, U., Stephanopoulos, G., St-Pierre, J., Tennant, D. A., Wittmann, C., Vander Heiden, M. G., Vazquez, A., Vousden, K., Young, J. D., Zamboni, N. & Fendt, S. M. A roadmap for interpreting 13C metabolite labeling patterns from cells. *Curr. Opin. Biotechnol.* 34, 189–201 (2015).

27. Aran, D., Sirota, M. & Butte, A. J. Systematic pan-cancer analysis of tumour purity. *Nat. Commun.* 6, 8971 (2015).

28. Shachaf, C. M., Kopelman, A. M., Arvanitis, C., Karlsson, A., Beer, S., Mandl, S., Bachmann, M. H., Borowsky, A. D., Ruebner, B., Cardiff, R. D., Yang, Q., Bishop, J. M., Contag, C. H. & Felsher, D. W. MYC inactivation uncovers pluripotent differentiation and tumour dormancy in hepatocellular cancer. *Nature* 431, 1112–7 (2004).

29. Lim, L., Balakrishnan, A., Huskey, N., Jones, K. D., Jodari, M., Ng, R., Song, G., Riordan, J., Anderton, B., Cheung, S. T., Willenbring, H., Dupuy, A., Chen, X., Brown, D., Chang, A. N. & Goga, A. MicroRNA-494 within an oncogenic microRNA megacluster regulates G<inf>1</inf>/S transition in liver tumorigenesis through suppression of mutated in colorectal cancer. *Hepatology* 59, 202–215 (2014).

30. Anderton, B., Camarda, R., Balakrishnan, S., Balakrishnan, A., Kohnz, R., Lim, L., Evason, K., Momcilovic, O., Kruttwig, K., Huang, Q., Xu, G., Nomura, D. & Goga, A. MYC-driven inhibition of the glutamate-cysteine ligase promotes glutathione depletion in liver cancer. *EMBO Rep.* (2017). doi:10.15252/embr.201643068

31. Calvisi, D. F. & Thorgeirsson, S. S. Molecular mechanisms of hepatocarcinogenesis in transgenic mouse models of liver cancer. *Toxicol. Pathol.* 33, 181–184 (2005).

32. Kaposi-Novak, P., Libbrecht, L., Woo, H. G., Lee, Y. H., Sears, N. C., Conner, E. A., Factor, V. M., Roskams, T. & Thorgeirsson, S. S. Central role of c-Myc during malignant conversion in human hepatocarcinogenesis. *Cancer Res.* 69, 2775–2782 (2009).

33. Wang, H., Lu, J., Edmunds, L. R., Kulkarni, S., Dolezal, J., Tao, J., Ranganathan, S., Jackson, L., Fromherz, M., Beer-Stolz, D., Uppala, R., Bharathi, S., Monga, S. P., Goetzman, E. S. & Prochownik, E. V. Coordinated Activities of Multiple Myc-dependent and Myc-independent Biosynthetic Pathways in Hepatoblastoma. *J. Biol. Chem.* 291, 26241–26251 (2016).

34. Hu, S., Balakrishnan, A., Bok, R. a., Anderton, B., Larson, P. E. Z., Nelson, S. J., Kurhanewicz, J., Vigneron, D. B. & Goga, A. 13C-pyruvate imaging reveals alterations in glycolysis that precede c-Myc-induced tumor formation and regression. *Cell Metab.* 14, 131–142 (2011).

35. Yuneva, M. O., Fan, T. W. M., Allen, T. D., Higashi, R. M., Ferraris, D. V., Tsukamoto, T., Matés, J. M., Alonso, F. J., Wang, C., Seo, Y., Chen, X. & Bishop, J. M. The metabolic profile of tumors depends on both the responsible genetic

lesion and tissue type. *Cell Metab.* 15, 157–170 (2012).

36. Xiang, Y., Stine, Z. E., Xia, J., Lu, Y., O'Connor, R. S., Altman, B. J., Hsieh, A. L., Gouw, A. M., Thomas, A. G., Gao, P., Sun, L., Song, L., Yan, B., Slusher, B. S., Zhuo, J., Ooi, L. L., Lee, C. G. L., Mancuso, A., McCallion, A. S., Le, A., Milone, M. C., Rayport, S., Felsher, D. W. & Dang, C. V. Targeted inhibition of tumor-specific glutaminase diminishes cell-autonomous tumorigenesis. *J. Clin. Invest.* 125, 2293–2306 (2015).

37. Wang, R., Ferrell, L. D., Faouzi, S., Maher, J. J. & Bishop, J. M. Activation of the Met receptor by cell attachment induces and sustains hepatocellular carcinomas in transgenic mice. *J. Cell Biol.* 153, 1023–34 (2001).

38. Allen, T. D., Zhu, C. Q., Jones, K. D., Yanagawa, N., Tsao, M. S. & Bishop, J. M. Interaction between MYC and MCL1 in the genesis and outcome of non-small-cell lung cancer. *Cancer Res.* 71, 2212–2221 (2011).

39. Ciribilli, Y., Singh, P., Inga, A. & Borlak, J. c-Myc targeted regulators of cell metabolism in a transgenic mouse model of papillary lung adenocarcinoma. *Oncotarget* 7, 65514–65539 (2016).

40. Shroff, E. H., Eberlin, L. S., Dang, V. M., Gouw, A. M., Gabay, M., Adam, S. J., Bellovin, D. I., Tran, P. T., Philbrick, W. M., Garcia-Ocana, A., Casey, S. C., Li, Y., Dang, C. V, Zare, R. N. & Felsher, D. W. MYC oncogene overexpression drives renal cell carcinoma in a mouse model through glutamine metabolism. *Proc. Natl. Acad. Sci. U. S. A.* 112, 6539–6544 (2015).

41. Bott, A. J., Peng, I. C., Fan, Y., Faubert, B., Zhao, L., Li, J., Neidler, S., Sun, Y., Jaber, N., Krokowski, D., Lu, W., Pan, J. A., Powers, S., Rabinowitz, J.,

Hatzoglou, M., Murphy, D. J., Jones, R., Wu, S., Girnun, G. & Zong, W. X. Oncogenic Myc Induces Expression of Glutamine Synthetase through Promoter Demethylation. *Cell Metab.* 22, 1068–1077 (2015).

42. Ellwood-Yen, K., Graeber, T. G., Wongvipat, J., Iruela-Arispe, M. L., Zhang, J., Matusik, R., Thomas, G. V & Sawyers, C. L. Myc-driven murine prostate cancer shares molecular features with human prostate tumors. *Cancer Cell* 4, 223–38 (2003).

43. Majumder, P. K., Yeh, J. J., George, D. J., Febbo, P. G., Kum, J., Xue, Q., Bikoff, R., Ma, H., Kantoff, P. W., Golub, T. R., Loda, M. & Sellers, W. R. Prostate intraepithelial neoplasia induced by prostate restricted Akt activation: the MPAKT model. *Proc. Natl. Acad. Sci. U. S. A.* 100, 7841–7846 (2003).

44. Priolo, C., Pyne, S., Rose, J., Regan, E. R., Zadra, G., Photopoulos, C., Cacciatore, S., Schultz, D., Scaglia, N., McDunn, J., De Marzo, A. M. & Loda, M. AKT1 and MYC induce distinctive metabolic fingerprints in human prostate cancer. *Cancer Res.* 74, 7198–7204 (2014).

45. Tward, A. D., Jones, K. D., Yant, S., Kay, M. A., Wang, R. & Bishop, J. M. Genomic progression in mouse models for liver tumors. *Cold Spring Harb. Symp. Quant. Biol.* 70, 217–24 (2005).

46. Gao, P., Tchernyshyov, I., Chang, T.-C., Lee, Y.-S., Kita, K., Ochi, T., Zeller, K. I., De Marzo, A. M., Van Eyk, J. E., Mendell, J. T. & Dang, C. V. c-Myc suppression of miR-23a/b enhances mitochondrial glutaminase expression and glutamine metabolism. *Nature* 458, 762–5 (2009).

47. Kota, J., Chivukula, R. R., O'Donnell, K. A., Wentzel, E. A., Montgomery, C. L.,

Hwang, H. W., Chang, T. C., Vivekanandan, P., Torbenson, M., Clark, K. R., Mendell, J. R. & Mendell, J. T. Therapeutic microRNA Delivery Suppresses Tumorigenesis in a Murine Liver Cancer Model. *Cell* 137, 1005–1017 (2009).

48. Carter, D. R., Sutton, S. K., Pajic, M., Murray, J., Sekyere, E. O., Fletcher, J., Beckers, A., De Preter, K., Speleman, F., George, R. E., Haber, M., Norris, M. D., Cheung, B. B. & Marshall, G. M. Glutathione biosynthesis is upregulated at the initiation of MYCN-driven neuroblastoma tumorigenesis. *Mol. Oncol.* 10, 866–78 (2016).

49. Weiss, W. A., Aldape, K., Mohapatra, G., Feuerstein, B. G. & Bishop, J. M. Targeted expression of MYCN causes neuroblastoma in transgenic mice. *EMBO J.* 16, 2985–2995 (1997).

50. Terunuma, A., Putluri, N., Mishra, P., Mathé, E. a., Dorsey, T. H., Yi, M., Wallace, T. a., Issaq, H. J., Zhou, M., Keith Killian, J., Stevenson, H. S., Karoly, E. D., Chan, K., Samanta, S., Prieto, D., Hsu, T. Y. T., Kurley, S. J., Putluri, V., Sonavane, R., Edelman, D. C., Wulff, J., Starks, A. M., Yang, Y., Kittles, R. a., Yfantis, H. G., Lee, D. H., Ioffe, O. B., Schiff, R., Stephens, R. M., Meltzer, P. S., Veenstra, T. D., Westbrook, T. F., Sreekumar, A. & Ambs, S. MYC-driven accumulation of 2-hydroxyglutarate is associated with breast cancer prognosis. *J. Clin. Invest.* 124, 398–412 (2014).

51. Intlekofer, A. M., DeMatteo, R. G., Venneti, S., Finley, L. W. S., Lu, C., Judkins, A. R., Rustenburg, A. S., Grinaway, P. B., Chodera, J. D., Cross, J. R. & Thompson, C. B. Hypoxia Induces Production of L-2-Hydroxyglutarate. *Cell Metab.* 22, 304–311 (2015).

52. Oldham, W. M., Clish, C. B., Yang, Y. & Loscalzo, J. Hypoxia-Mediated Increases in l-2-hydroxyglutarate Coordinate the Metabolic Response to Reductive Stress. *Cell Metab.* 22, 291–303 (2015).

53. Cairo, S., Armengol, C., De Reyniès, A., Wei, Y., Thomas, E., Renard, C.-A., Goga, A., Balakrishnan, A., Semeraro, M., Gresh, L., Pontoglio, M., Strick-Marchand, H., Levillayer, F., Nouet, Y., Rickman, D., Gauthier, F., Branchereau, S., Brugières, L., Laithier, V., Bouvier, R., Boman, F., Basso, G., Michiels, J.-F., Hofman, P., Arbez-Gindre, F., Jouan, H., Rousselet-Chapeau, M.-C., Berrebi, D., Marcellin, L., Plenat, F., Zachar, D., Joubert, M., Selves, J., Pasquier, D., Bioulac-Sage, P., Grotzer, M., Childs, M., Fabre, M. & Buendia, M.-A. Hepatic stem-like phenotype and interplay of Wnt/beta-catenin and Myc signaling in aggressive childhood liver cancer. *Cancer Cell* 14, 471–84 (2008).

54. Perry, R. H., Bellovin, D. I., Shroff, E. H., Ismail, A. I., Zabuawala, T., Felsher, D. W. & Zare, R. N. Characterization of MYC-induced tumorigenesis by in situ lipid profiling. *Anal. Chem.* 85, 4259–4262 (2013).

55. Felsher, D. W. & Bishop, J. M. Reversible tumorigenesis by MYC in hematopoietic lineages. *Mol. Cell* 4, 199–207 (1999).

56. Harris, A. W., Pinkert, C. A., Crawford, M., Langdon, W. Y., Brinster, R. L. & Adams, J. M. The E mu-myc transgenic mouse. A model for high-incidence spontaneous lymphoma and leukemia of early B cells. *J. Exp. Med.* 167, 353–71 (1988).

57. Pacilli, A., Calienni, M., Margarucci, S., D'Apolito, M., Petillo, O., Rocchi, L., Pasquinelli, G., Nicolai, R., Koverech, A., Calvani, M., Peluso, G. & Montanaro, L.

Carnitine-acyltransferase system inhibition, cancer cell death, and prevention of myc-induced lymphomagenesis. *J. Natl. Cancer Inst.* 105, 489–498 (2013).

58. D'Cruz, C. M., Gunther, E. J., Boxer, R. B., Hartman, J. L., Sintasath, L., Moody, S. E., Cox, J. D., Ha, S. I., Belka, G. K., Golant, a, Cardiff, R. D. & Chodosh, L. a. c-MYC induces mammary tumorigenesis by means of a preferred pathway involving spontaneous Kras2 mutations. *Nat. Med.* 7, 235–239 (2001).

59. Pfefferle, A. D., Herschkowitz, J. I., Usary, J., Harrell, J. C., Spike, B. T., Adams, J. R., Torres-Arzayus, M. I., Brown, M., Egan, S. E., Wahl, G. M., Rosen, J. M. & Perou, C. M. Transcriptomic classification of genetically engineered mouse models of breast cancer identifies human subtype counterparts. *Genome Biol.* 14, R125 (2013).

60. DeRose, Y. S., Wang, G., Lin, Y., Bernard, P. S., Buys, S. S., Ebbert, M. T. W., Factor, R., Matsen, C., Milash, B. a, Nelson, E., Neumayer, L., Randall, R. L., Stijleman, I. J., Welm, B. E. & Welm, A. L. Tumor grafts derived from women with breast cancer authentically reflect tumor pathology, growth, metastasis and disease outcomes. *Nature Medicine* 17, 1514–1520 (2011).

61. Camarda, R., Zhou, A. Y., Kohnz, R. A., Balakrishnan, S., Mahieu, C., Anderton, B., Eyob, H., Kajimura, S., Tward, A., Krings, G., Nomura, D. K. & Goga, A. Inhibition of fatty acid oxidation as a therapy for MYC-overexpressing triple-negative breast cancer. *Nat. Med.* 22, 427–432 (2016).

62. Park, J. H., Vithayathil, S., Kumar, S., Sung, P.-L., Dobrolecki, L. E., Putluri, V., Bhat, V. B., Bhowmik, S. K., Gupta, V., Arora, K., Wu, D., Tsouko, E., Zhang, Y., Maity, S., Donti, T. R., Graham, B. H., Frigo, D. E., Coarfa, C., Yotnda, P., Putluri,

N., Sreekumar, A., Lewis, M. T., Creighton, C. J., Wong, L.-J. C. & Kaipparettu, B. A. Fatty Acid Oxidation-Driven Src Links Mitochondrial Energy Reprogramming and Oncogenic Properties in Triple-Negative Breast Cancer. *Cell Rep.* 14, 2154–65 (2016).

63. Li, F., Wang, Y., Zeller, K. I., Potter, J. J., Wonsey, D. R., Donnell, K. a O., Kim, J., Yustein, J. T., Lee, L. a & Dang, C. V. Myc Stimulates Nuclearly Encoded Mitochondrial Genes and Mitochondrial Biogenesis Myc Stimulates Nuclearly Encoded Mitochondrial Genes and Mitochondrial Biogenesis †. *Mol. Cell. Biol.* 25, 6225–6234 (2005).

64. Zirath, H., Frenzel, A., Oliynyk, G., Segerström, L., Westermark, U. K., Larsson, K., Munksgaard Persson, M., Hultenby, K., Lehtiö, J., Einvik, C., Påhlman, S., Kogner, P., Jakobsson, P.-J. & Henriksson, M. A. MYC inhibition induces metabolic changes leading to accumulation of lipid droplets in tumor cells. *Proc. Natl. Acad. Sci. U. S. A.* 110, 10258–63 (2013).

65. Abu-Elheiga, L., Matzuk, M. M., Abo-Hashema, K. a & Wakil, S. J. Continuous fatty acid oxidation and reduced fat storage in mice lacking acetyl-CoA carboxylase 2. *Science* 291, 2613–2616 (2001).

66. Nieman, K. M., Kenny, H. a, Penicka, C. V, Ladanyi, A., Buell-Gutbrod, R., Zillhardt, M. R., Romero, I. L., Carey, M. S., Mills, G. B., Hotamisligil, G. S., Yamada, S. D., Peter, M. E., Gwin, K. & Lengyel, E. Adipocytes promote ovarian cancer metastasis and provide energy for rapid tumor growth. *Nat. Med.* 17, 1498–1503 (2011).

67. Liu, R. Z., Graham, K., Glubrecht, D. D., Germain, D. R., Mackey, J. R. &

Godbout, R. Association of FABP5 expression with poor survival in triple-negative breast cancer: Implication for retinoic acid therapy. *Am. J. Pathol.* 178, 997–1008 (2011).

68. Horiuchi, D., Camarda, R., Zhou, A. Y., Yau, C., Momcilovic, O., Balakrishnan, S., Corella, A. N., Eyob, H., Kessenbrock, K., Lawson, D. A., Marsh, L. A., Anderton, B. N., Rohrberg, J., Kunder, R., Bazarov, A. V, Yaswen, P., McManus, M. T., Rugo, H. S., Werb, Z. & Goga, A. PIM1 kinase inhibition as a targeted therapy against triple-negative breast tumors with elevated MYC expression. *Nat. Med.* 22, 1321–1329 (2016).

69. Brasó-Maristany, F., Filosto, S., Catchpole, S., Marlow, R., Quist, J., Francesch-Domenech, E., Plumb, D. A., Zakka, L., Gazinska, P., Liccardi, G., Meier, P., Gris-Oliver, A., Cheang, M. C. U., Perdrix-Rosell, A., Shafat, M., Noël, E., Patel, N., McEachern, K., Scaltriti, M., Castel, P., Noor, F., Buus, R., Mathew, S., Watkins, J., Serra, V., Marra, P., Grigoriadis, A. & Tutt, A. N. PIM1 kinase regulates cell death, tumor growth and chemotherapy response in triple-negative breast cancer. *Nat. Med.* 22, 1303–1313 (2016).

70. Beharry, Z., Mahajan, S., Zemskova, M., Lin, Y.-W., Tholanikunnel, B. G., Xia, Z., Smith, C. D. & Kraft, A. S. The Pim protein kinases regulate energy metabolism and cell growth. *Proc. Natl. Acad. Sci. U. S. A.* 108, 528–33 (2011).

71. Le, X., Antony, R., Razavi, P., Treacy, D. J., Luo, F., Ghandi, M., Castel, P., Scaltriti, M., Baselga, J. & Garraway, L. A. Systematic functional characterization of resistance to PI3K inhibition in breast cancer. *Cancer Discov.* 6, 1134–1147 (2016).

72. Hu, H., Juvekar, A., Lyssiotis, C. A., Lien, E. C., Albeck, J. G., Oh, D., Varma, G., Hung, Y. P., Ullas, S., Lauring, J., Seth, P., Lundquist, M. R., Tolan, D. R., Grant, A. K., Needleman, D. J., Asara, J. M., Cantley, L. C. & Wulf, G. M. Phosphoinositide 3-Kinase Regulates Glycolysis through Mobilization of Aldolase from the Actin Cytoskeleton. *Cell* 164, 433–446 (2016).

73. Barna, M., Pusic, A., Zollo, O., Costa, M., Kondrashov, N., Rego, E., Rao, P. H. & Ruggero, D. Suppression of Myc oncogenic activity by ribosomal protein haploinsufficiency. *Nature* 456, 971–975 (2008).

74. Cunningham, J. T., Moreno, M. V., Lodi, A., Ronen, S. M. & Ruggero, D. Protein and nucleotide biosynthesis are coupled by a single rate-limiting enzyme, PRPS2, to drive cancer. *Cell* 157, 1088–1103 (2014).

75. Hart, L. S., Cunningham, J. T., Datta, T., Dey, S., Tameire, F., Lehman, S. L., Qiu, B., Zhang, H., Cerniglia, G., Bi, M., Li, Y., Gao, Y., Liu, H., Li, C., Maity, A., Thomas-Tikhonenko, A., Perl, A. E., Koong, A., Fuchs, S. Y., Diehl, J. A., Mills, I. G., Ruggero, D. & Koumenis, C. ER stress-mediated autophagy promotes Myc-dependent transformation and tumor growth. *J. Clin. Invest.* 122, 4621–4634 (2012).

76. Shachaf, C. M., Perez, O. D., Youssef, S., Fan, A. C., Elchuri, S., Goldstein, M. J., Shirer, A. E., Sharpe, O., Chen, J., Mitchell, D. J., Chang, M., Nolan, G. P., Steinman, L. & Felsher, D. W. Inhibition of HMGcoA reductase by atorvastatin prevents and reverses MYC-induced lymphomagenesis. *Blood* 110, 2674–2684 (2007).

77. Cao, Z., Fan-Minogue, H., Bellovin, D. I., Yevtodiyenko, A., Arzeno, J., Yang, Q.,

Gambhir, S. S. & Felsher, D. W. MYC phosphorylation, activation, and tumorigenic potential in hepatocellular carcinoma are regulated by HMG-CoA reductase. *Cancer Res.* 71, 2286–97 (2011).

78. Burén, S., Gomes, A. L., Teijeiro, A., Fawal, M.-A., Yilmaz, M., Tummala, K. S., Perez, M., Rodriguez-Justo, M., Campos-Olivas, R., Megías, D. & Djouder, N. Regulation of OGT by URI in Response to Glucose Confers c-MYC-Dependent Survival Mechanisms. *Cancer Cell* 30, 290–307 (2016).

79. Chou, T. Y., Hart, G. W. & Dang, C. V. c-Myc is glycosylated at threonine 58, a known phosphorylation site and a mutational hot spot in lymphomas. *Journal of Biological Chemistry* 270, 18961–18965 (1995).

80. Fletcher, J. W., Djulbegovic, B., Soares, H. P., Siegel, B. a, Lowe, V. J., Lyman, G. H., Coleman, R. E., Wahl, R., Paschold, J. C., Avril, N., Einhorn, L. H., Suh, W. W., Samson, D., Delbeke, D., Gorman, M. & Shields, A. F. Recommendations on the use of 18F-FDG PET in oncology. *J. Nucl. Med.* 49, 480–508 (2008).

81. Kim, J., Gao, P., Liu, Y.-C., Semenza, G. L. & Dang, C. V. Hypoxia-inducible factor 1 and dysregulated c-Myc cooperatively induce vascular endothelial growth factor and metabolic switches hexokinase 2 and pyruvate dehydrogenase kinase 1. *Mol. Cell. Biol.* 27, 7381–93 (2007).

82. Palaskas, N., Larson, S. M., Schultz, N., Komisopoulou, E., Wong, J., Rohle, D., Campos, C., Yannuzzi, N., Osborne, J. R., Linkov, I., Kastenhuber, E. R., Taschereau, R., Plaisier, S. B., Tran, C., Heguy, A., Wu, H., Sander, C., Phelps, M. E., Brennan, C., Port, E., Huse, J. T., Graeber, T. G. & Mellinghoff, I. K. 18F-fluorodeoxy-glucose positron emission tomography marks MYC-overexpressing

human basal-like breast cancers. *Cancer Res.* 71, 5164–5174 (2011).

83. Lieberman, B. P., Ploessl, K., Wang, L., Qu, W., Zha, Z., Wise, D. R., Chodosh, L. a, Belka, G., Thompson, C. B. & Kung, H. F. PET imaging of glutaminolysis in tumors by 18F-(2S,4R)4-fluoroglutamine. *J. Nucl. Med.* 52, 1947–55 (2011).

84. Comerford, S. A., Huang, Z., Du, X., Wang, Y., Cai, L., Witkiewicz, A. K., Walters, H., Tantawy, M. N., Fu, A., Manning, H. C., Horton, J. D., Hammer, R. E., McKnight, S. L. & Tu, B. P. Acetate dependence of tumors. *Cell* 159, 1591–602 (2014).

85. Mashimo, T., Pichumani, K., Vemireddy, V., Hatanpaa, K. J., Singh, D. K., Sirasanagandla, S., Nannepaga, S., Piccirillo, S. G., Kovacs, Z., Foong, C., Huang, Z., Barnett, S., Mickey, B. E., DeBerardinis, R. J., Tu, B. P., Maher, E. A. & Bachoo, R. M. Acetate Is a Bioenergetic Substrate for Human Glioblastoma and Brain Metastases. *Cell* 159, 1603–1614 (2014).

86. Nelson, S. J., Kurhanewicz, J., Vigneron, D. B., Larson, P. E. Z., Harzstark, A. L., Ferrone, M., van Criekinge, M., Chang, J. W., Bok, R., Park, I., Reed, G., Carvajal, L., Small, E. J., Munster, P., Weinberg, V. K., Ardenkjaer-Larsen, J. H., Chen, A. P., Hurd, R. E., Odegardstuen, L.-I., Robb, F. J., Tropp, J. & Murray, J. A. Metabolic imaging of patients with prostate cancer using hyperpolarized [1-^{13}C]pyruvate. *Sci. Transl. Med.* 5, 198ra108 (2013).

87. Kurhanewicz, J., Vigneron, D. B., Brindle, K., Chekmenev, E. Y., Comment, A., Cunningham, C. H., Deberardinis, R. J., Green, G. G., Leach, M. O., Rajan, S. S., Rizi, R. R., Ross, B. D., Warren, W. S. & Malloy, C. R. Analysis of cancer metabolism by imaging hyperpolarized nuclei: prospects for translation to clinical

research. *Neoplasia* 13, 81–97 (2011).

88. Huang, Q., Tan, Y., Yin, P., Ye, G., Gao, P., Lu, X., Wang, H. & Xu, G. Metabolic characterization of hepatocellular carcinoma using nontargeted tissue metabolomics. *Cancer Res.* 73, 4992–5002 (2013).

89. Liu, Y., Hong, Z., Tan, G., Dong, X., Yang, G., Zhao, L., Chen, X., Zhu, Z., Lou, Z., Qian, B., Zhang, G. & Chai, Y. NMR and LC/MS-based global metabolomics to identify serum biomarkers differentiating hepatocellular carcinoma from liver cirrhosis. *Int. J. Cancer* 135, 658–668 (2014).

90. Kanaan, Y. M., Sampey, B. P., Beyene, D., Esnakula, A. K., Naab, T. J., Ricks-Santi, L. J., Dasi, S., Day, A., Blackman, K. W., Frederick, W., Copeland, R. L., Gabrielson, E. & Dewitty, R. L. Metabolic profile of triple-negative breast cancer in African-American women reveals potential biomarkers of aggressive disease. *Cancer Genomics Proteomics* 11, 279–94 (2014).

91. Cao, M. D., Lamichhane, S., Lundgren, S., Bofin, A., Fjøsne, H., Giskeødegård, G. F. & Bathen, T. F. Metabolic characterization of triple negative breast cancer. *BMC Cancer* 14, 941 (2014).

92. Cui, M., Wang, Q. & Chen, G. Serum metabolomics analysis reveals changes in signaling lipids in breast cancer patients. *Biomed. Chromatogr.* 30, 42–47 (2016).

93. Wettersten, H. I., Hakimi, A. A., Morin, D., Bianchi, C., Johnstone, M. E., Donohoe, D. R., Trott, J. F., Abu Aboud, O., Stirdivant, S., Neri, B., Wolfert, R., Stewart, B., Perego, R., Hsieh, J. J. & Weiss, R. H. Grade-dependent metabolic reprogramming in kidney cancer revealed by combined proteomics and metabolomics analysis. *Cancer Res.* 75, 2541–2552 (2015).

94. Lawson, D. A., Bhakta, N. R., Kessenbrock, K., Prummel, K. D., Yu, Y., Takai, K., Zhou, A., Eyob, H., Balakrishnan, S., Wang, C., Yaswen, P., Goga, A. & Werb, Z. Single-cell analysis reveals a stem-cell program in human metastatic breast cancer cells. *Nature* 526, 131–5 (2015).

95. Pascual G, Avgustinova A, Mejetta S, Martín M, Attolini C, Berenguer A, Toll A, Hueto J, Bescós C, Croce LD, B. S. Targeting metastasis stem cells through the fatty acid receptor CD36. *Nature* 1, 1–25 (2016).

96. LeBleu, V. S., O'Connell, J. T., Gonzalez Herrera, K. N., Wikman, H., Pantel, K., Haigis, M. C., de Carvalho, F. M., Damascena, A., Domingos Chinen, L. T., Rocha, R. M., Asara, J. M. & Kalluri, R. PGC-1α mediates mitochondrial biogenesis and oxidative phosphorylation in cancer cells to promote metastasis. *Nat. Cell Biol.* 16, 992–1003, 1–15 (2014).

97. Dupuy, F., Tabariès, S., Andrzejewski, S., Dong, Z., Blagih, J., Annis, M. G., Omeroglu, A., Gao, D., Leung, S., Amir, E., Clemons, M., Aguilar-Mahecha, A., Basik, M., Vincent, E. E., St-Pierre, J., Jones, R. G. & Siegel, P. M. PDK1-Dependent Metabolic Reprogramming Dictates Metastatic Potential in Breast Cancer. *Cell Metab.* 22, 577–89 (2015).

98. Chang, C. H., Qiu, J., O'Sullivan, D., Buck, M. D., Noguchi, T., Curtis, J. D., Chen, Q., Gindin, M., Gubin, M. M., Van Der Windt, G. J. W., Tonc, E., Schreiber, R. D., Pearce, E. J. & Pearce, E. L. Metabolic Competition in the Tumor Microenvironment Is a Driver of Cancer Progression. *Cell* 162, 1229–1241 (2015).

99. Hofmann, J. W., Zhao, X., De Cecco, M., Peterson, A. L., Pagliaroli, L., Manivannan, J., Hubbard, G. B., Ikeno, Y., Zhang, Y., Feng, B., Li, X., Serre, T.,

Qi, W., Van Remmen, H., Miller, R. A., Bath, K. G., De Cabo, R., Xu, H., Neretti, N. & Sedivy, J. M. Reduced expression of MYC increases longevity and enhances healthspan. *Cell* 160, 477–488 (2015).

Chapter 2

Inhibition of fatty acid oxidation as a therapy for MYC-overexpressing triple-negative breast cancer

Summary

Expression of the oncogenic transcription factor MYC is disproportionately elevated in triple-negative breast cancer (TNBC), as compared to estrogen receptor–, progesterone receptor– or human epidermal growth factor 2 receptor–positive (RP) breast cancer[1,2]. We and others have shown that MYC alters metabolism during tumorigenesis[3,4]. However, the role of MYC in TNBC metabolism remains mostly unexplored. We hypothesized that MYC-dependent metabolic dysregulation is essential for the growth of MYC-overexpressing TNBC cells and may identify new therapeutic targets for this clinically challenging subset of breast cancer. Using a targeted metabolomics approach, we identified fatty acid oxidation (FAO) intermediates as being dramatically upregulated in a MYC-driven model of TNBC. We also identified a lipid metabolism gene signature in patients with TNBC that were identified from The Cancer Genome Atlas database and from multiple other clinical data sets, implicating FAO as a dysregulated pathway that is critical for TNBC cell metabolism. We found that pharmacologic inhibition of FAO catastrophically decreased energy metabolism in MYC-overexpressing TNBC cells and blocked tumor growth in a MYC-driven transgenic TNBC model and in a MYC-overexpressing TNBC patient–derived xenograft. These findings demonstrate that MYC-overexpressing TNBC shows an increased bioenergetic reliance on FAO and identify the inhibition of FAO as a potential therapeutic strategy for this subset of breast cancer.

Results

We hypothesized that MYC-dependent metabolic dysregulation is essential for MYC-overexpressing TNBC. To test this hypothesis, we investigated tumor metabolism in a conditional doxycycline-inducible transgenic model of MYC-overexpressing TNBC (MTB-TOM)[5,6]. We used mass spectrometry to compare the global metabolic profile of MTB-TOM tumors to that of naive mammary glands from MTB-TOM transgenic mice in which MYC was not induced. Metabolite analysis revealed a number of dysregulated pathways in MTB-TOM tumors that are commonly associated with tumorigenesis—including glycolysis, the tricarboxylic acid (TCA) cycle and fatty acid metabolism (Fig. 1a, Supplementary Fig. 1 and Supplementary Table 1). Although fatty acid synthesis (FAS) is upregulated in many types of cancer, a MYC-dependent role for FAO in breast tumorigenesis has not previously been described[4,7,8]. Considering the proximity of primary breast tumors to the adipose-rich mammary gland, we chose to focus on the dysregulation of FAO in MYC-overexpressing TNBC cells.

To investigate the role of MYC in FAO upregulation in TNBC cells, we returned to our MTB-TOM metabolomic data (Supplementary Table 1). Acylcarnitines are an essential intermediate and are involved in the first committed step of FAO[9]. To catabolize long-chain fatty acids (such as palmitate) to acetyl–coenzyme A (acetyl-CoA), a major fuel for biosynthetic and bioenergetic metabolism, acyl-CoAs must be enzymatically converted to acylcarnitines across the outer mitochondrial membrane by carnitine palmitoyltransferase 1 (CPT1A or CPT1B)[9]. We found that all six acylcarnitine intermediates detected in our metabolomic analysis were significantly elevated in MTB-TOM tumors than in control tissue (Fig. 1b). To further validate these steady-state

findings in vivo, we assayed acylcarnitine production in MTB-TOM tumors 4 h after intraperitoneal (i.p.) injection of [^{13}C]palmitate into tumor-bearing mice. Tumor tissue had a fourfold increase in [^{13}C]palmitoyl-carnitine production, as compared to that in control mammary gland tissue (Fig. 1c). Because [^{13}C]palmitoyl-carnitine production was not normalized to overall uptake in this experiment, this increase could reflect a relative increase in fatty acid uptake, fatty acid utilization via oxidation or both. Nevertheless, taken together, these data indicate that the first committed step of FAO is upregulated in MYC-overexpressing TNBC cells.

To determine how FAO is altered in TNBC, we analyzed RNA expression data from primary human tumors (771 patient samples from The Cancer Genome Atlas (TCGA)). Of 336 genes associated with fatty acid metabolism in the Gene Ontology database (GO:0006631), we found that 244 (73%) were significantly dysregulated (false-discovery rate (FDR) < 0.05) in triple-negative (TN) versus RP breast tumors (Supplementary Table 2). We also found that TN tumors showed upregulation of many genes that encode activators of FAO (including the gene encoding the master transcriptional regulator PPARG coactivator 1 alpha (also known as PGC-1α; encoded by PPARGC1A)) and downregulation of many genes that encode activators of fatty acid synthesis (FAS) (including fatty acid synthase (FASN) and acetyl-coA carboxylase beta (ACACB; also known as ACC2)) (Supplementary Table 2). We applied the fatty acid metabolism signature identified from TCGA samples (Fig. 2a) to four additional breast cancer clinical cohorts (2,119 total patients including those from TCGA) and confirmed that this signature was highly correlated with TNBC tumor samples (Supplementary Fig. 2 and Supplementary Table 3)[10–13]. Next we confirmed upregulation of key FAO

activators and downregulation of key FAS activators at the protein level in TN versus RP human breast cancer cell lines (Fig. 2b)[4,14,15]. Notably, whereas FASN and ACC2 were markedly downregulated in TN cell lines as compared to RP cells, ACACA (ACC1) was expressed equivalently in TN and RP cell lines. To directly test whether FAO is increased in MYC^{high} TNBC cells, we measured [^{14}C]oleic acid conversion to $^{14}CO2$ and found an ~50% increase in FAO in MYC^{high} TNBC cells as compared to MYC^{low} TNBC cells or to RP cells (Fig. 2c). Taken together, these data suggest that FAO is upregulated in MYC^{high} TNBC cells.

TNBC is the most aggressive subtype of breast cancer and is characterized by poor clinical outcome[1,2]. To determine whether FAO gene expression is associated with prognosis, we performed univariate analysis of the 336 fatty acid metabolism genes on a patient cohort with long-term distant recurrence-free survival data (Supplementary Table 4)[11]. We found that decreased expression of ACACB—which encodes the ACC2 enzyme that produces malonyl-CoA to directly inhibit CPT1A and CPT1B, and therefore FAO—was associated with worse prognosis for all patients, as well as for the TNBC cohort (Fig. 2d)[9]. Although decreased ACACB expression was also associated with worse outcome for patients with RP tumors, the median time to distant recurrence-free survival was not reached in this cohort, suggesting that FAO may be a less important marker of tumor recurrence in RP cancers (Fig. 2d). These patient data suggest that decreased ACACB expression, and thus increased FAO, may contribute to the aggressiveness of breast tumors, with the worst outcome occurring in the TNBC subset.

FAO is the primary bioenergetic pathway in many non-tumor tissues[9]. We therefore investigated whether this pathway is essential for energy production in MYC-

overexpressing TNBC. We used etomoxir (a clinically tested, specific inhibitor of CPT1)[16] to determine the effects of FAO inhibition on ATP and NAD(P)H production. We first examined nine human breast cancer cell lines (six TN and three RP) with various levels of MYC expression[15]. Etomoxir treatment dramatically inhibited ATP production in TNBC cell lines expressing high amounts of MYC, whereas TN and RP cell lines expressing low amounts of MYC were significantly less affected (Fig. 3). Analysis of cell proliferation and apoptosis revealed that etomoxir-treated MYC^{high} cells show decreased proliferation without a decrease in viability (Supplementary Fig. 3 and Supplementary Data).

To validate the requirement for FAO in MYC-overexpressing TNBC, we used an orthogonal approach in which we extracted data from the Project Achilles data set[17] for the knockdown of CPT1B. Specifically, the growth of 216 cancer cell lines was measured after each line was treated independently with five shRNAs specific for CPT1B[17]. To determine whether CPT1B expression was required for breast cancer growth, we focused on the 13 breast cancer cell lines tested (of which there was no overlap with the lines used above): BT20, CAL120, CAL51, HCC1187, HCC1395, HCC70, MDAMB453, BT474, EFM19, HCC1954, HCC2218, MCF7 and ZR7530. We categorized these lines as RP, TN MYC^{low} and TN MYC^{high} (as in Fig. 3a) on the basis of MYC expression levels (data not shown). We found that the growth of TN MYC^{high} cells was significantly more sensitive to CPT1B knockdown than that of RP or TN MYC^{low} cells (Fig. 3b). Additionally, we used siRNA to deplete CPT2, which encodes another essential FAO enzyme[9]. CPT2 knockdown markedly decreased proliferation of MYC^{high} TN cells, but it had a significantly weaker growth inhibitory effect on RP cells

(Fig. 3c and Supplementary Fig. 4). Thus, the results obtained with small-molecule inhibition or with knockdown of CPT1B, as well as with knockdown of CPT2, suggest that FAO is an essential metabolic pathway in MYC-overexpressing TNBC cells.

FAO has been shown to be important for cells that have become detached from matrix and that are grown in nutrient-deprived conditions[18,19]. We therefore asked whether TN receptor and MYC status affect the response to FAO inhibition for tumor cells that are either not attached to matrix or deprived of glucose. To model matrix detachment, we used ultra-low-adhesion plates and grew breast cancer cell lines as spheres. Whereas TN MYC^{high}, TN MYC^{low} and RP cells were all able to form viable spheres upon matrix detachment, TN MYC^{high} cells were significantly ($P < 0.0001$) more sensitive to FAO inhibition (Supplementary Fig. 5). Next we tested the additive effect of FAO inhibition and glucose deprivation. Both TN MYC^{high} and TN MYC^{low} cells showed an increased sensitivity to glucose deprivation, as compared to that for RP cells (Supplementary Fig. 6), consistent with the well-established dependence on glycolysis for TNBC cell growth[20]. Concurrent depletion of glucose and inhibition of FAO resulted in an additive effect on ATP depletion in TN, but not in RP, cells (Supplementary Fig. 6). These results are consistent with previous findings that FAO is important for breast cancer cell survival and NADPH production, for conditions of limited glycolysis[21], and suggest that TN MYC^{high} cells are more reliant on FAO for survival than MYC^{low} cells under conditions of matrix detachment or nutrient deprivation.

To confirm that the observed bioenergetic reliance for FAO in MYC-overexpressing TNBC cells is a MYC-dependent phenotype, we examined whether conditional MYC expression alters the sensitivity of cells to FAO inhibition. We used two

approaches; the first was to use non-tumor human mammary epithelial (HMEC) cells expressing a 4-hydroxytamoxifen (TAM)-inducible MYC–estrogen receptor (ER) fusion protein (hereafter referred to as $HMEC^{MYC\text{-}ER}$ cells), and the second was to use two RP lines, each stably transduced with a MYC overexpression construct or control vector[1,15] (Supplementary Fig. 7). TAM-induced $HMEC^{MYC\text{-}ER}$ and MYC-transduced RP cells were significantly more sensitive to etomoxir than uninduced $HMEC^{MYC\text{-}ER}$ and vector-transduced RP cells, respectively (Fig. 3d). Furthermore, siRNA-mediated knockdown of MYC significantly rescued etomoxir sensitivity in three of four MYC^{high} TNBC cell lines tested (Fig. 3e and Supplementary Fig. 8). Finally, MYC protein expression significantly correlated with bioenergetic sensitivity to FAO inhibition in our panel of human breast cancer cell lines (Fig. 3f). Although MYC expression was not tightly correlated with FAO or FAS protein expression (Figs. 2b and 3f), it did correlate well with FAO-inhibition sensitivity and FAO activity (Figs. 2c and 3f). These data suggest that MYC expression is both necessary and sufficient to induce a bioenergetic reliance for FAO in breast epithelial and breast cancer cells.

Given that our initial observation of dysregulated FAO was made in MYC-driven breast tumors, we sought to test the effects of FAO inhibition on the metabolism of MYC-overexpressing TNBC in vivo. We obtained a panel of human TN and RP breast cancer patient–derived xenografts (PDX) with various MYC levels (Fig. 4a)[22]. We administered etomoxir (60 mg per kg of body weight (mg/kg)) or vehicle by i.p. injection to mice bearing orthotopic HCI-002 MYC^{high} TNBC PDXs at two time points (0 and 24 h) (Fig. 4a)[22]. Metabolite analysis of HCI-002 tumors harvested at 26 h revealed a significant reduction in long-chain acylcarnitine levels, as well as a reduction in TCA

cycle intermediates (especially α-ketoglutarate) in drug-treated tumors, as compared to vehicle-treated tumors (Fig. 4b and Supplementary Table 5). Etomoxir-treated tumors had a significant increase in phosphorylated AMPK (pAMPK) levels, a well-established marker of bioenergetic stress, as compared to control-treated tumors (Fig. 4c). In a second metabolomic study, as compared to vehicle-treated tumors, MTB-TOM tumors that were treated with 20 mg/kg etoxomir for 14 d showed a marked reduction in the levels of the majority of TCA cycle intermediates measured, as well as in the level of ATP, and also showed a significant ($P < 0.05$) increase in AMP/ATP, ADP/ATP, UMP/UTP and UDP/UTP ratios (Supplementary Fig. 9 and Supplementary Table 6). These data indicate that treatment with an FAO inhibitor decreases bioenergetic metabolism in vivo in both transgenic and PDX models of TNBC.

This observed reduction in bioenergetic metabolism prompted us to analyze the effects of prolonged FAO inhibition on the growth of MYC-overexpressing TNBC tumors. We performed orthotopic transfer of MTB-TOM or HCI-002 PDX tumors into the mammary fat pad of syngeneic FVB/N or immunodeficient NOD/SCID mice, respectively. In the case of MTB-TOM allograft-bearing mice, we administered 40 mg/kg etomoxir or vehicle by i.p. injection daily for 14 d; in the case of HCI-002 PDX–bearing mice, we administered 40 or 60 mg/kg etomoxir or vehicle by i.p. injection daily for 21 d. Etomoxir treatment resulted in a significant attenuation of tumor growth in both models and a significant extension of the time to ethical end point in the PDX model (Fig. 4d,e). In contrast, we observed no significant attenuation in tumor growth of mice with HCI-009 MYC^{low} TNBC PDX tumors that were treated with 40 mg/kg etomoxir (Fig. 4f). HCI-009 showed a moderate level of ACC2 expression (Fig. 4a), suggesting that FAO might be

attenuated in these tumors and explaining their resistance to etomoxir. The efficacy of etoxomir in both MYC^{high} transgenic and PDX models, but not in a MYC^{low} PDX model, suggests that high MYC expression, as well as low ACC2 expression, may serve as a biomarker of sensitivity to FAO inhibition.

Next we determined the effects of FAO inhibition on cell proliferation and death. HCI-002 PDX–bearing mice that were treated with 60 mg/kg etomoxir showed significantly decreased staining of the cell proliferation marker Ki-67 in the tumors (indicative of decreased cell proliferation), as compared to tumors from vehicle-treated mice, and a dose-dependent increase in TUNEL staining (indicative of increased apoptosis) (Fig. 4g,h). In contrast, etomoxir treatment of cultured MYC-overexpressing TNBC cell lines had a marked effect on cell proliferation but no appreciable effects on cell death (Supplementary Fig. 3). These contrasting results suggest that FAO has a more critical role for in vivo tumor cell viability than it does in vitro.

Elevated MYC expression was recently discovered to be a defining factor of TNBC[1,2]. The present study is among the first to investigate the role of MYC in TNBC metabolism in vivo[20]. Here we show that FAO is upregulated in MYC-overexpressing TNBC cells and that TNBC is sensitive to FAO inhibition in a MYC-dependent manner, as shown using several models of MYC-overexpressing TNBC in vitro and PDX and transgenic models in vivo. This work supports a critical role for FAO in TNBC, and it identifies high levels of MYC expression as a marker for this dependence. On the basis of our findings, inhibition of FAO as a therapeutic strategy for MYC-overexpressing TNBC should be further investigated.

Experimental procedures

Patient-derived xenograft models. All human samples used to generate PDX tumors, as well as the human non-tumor samples, were previously described[22].

MTB-TOM tumor generation. All protocols described in this and other sections regarding animal studies were approved by the UCSF Institutional Animal Care and Use Committee. MTB-TOM (MMTV-rtTA/TetO-MYC) mice were generated as previously described[5]. Mice were bred and maintained off of doxycycline. At 12–15 weeks of age, female mice were put on doxycycline (200 mg/kg doxy chow, Bio-Serv) to induce MYC expression and tumorigenesis. Mice were monitored daily for tumor growth by inspection and caliper measurement in two dimensions. Mice were sacrificed as per ethical guidelines (tumors reaching 2 cm in any single dimension) and tumor(s) or mammary gland(s) were flash-frozen in liquid nitrogen.

Metabolomics. For U-[^{13}C]palmitate flux analyses, the labeled palmitate (Cambridge Isotope Laboratories Inc., CLM-409-0.5) or unlabeled palmitate (Sigma) was diluted in PEG40 (Spectrum) via sonication and was administered via intraperitoneal injection at 100 mg/kg. 4 h after the injection, the animals were sacrificed and the tumors were flash-frozen. Nonpolar metabolites were extracted using a Dounce homogenizer in 4 ml of 2:1:1 chloroform:methanol:PBS spiked with 10 nmol of internal standards (C12:0 dodecylglycerol and pentadecanoic acid; Sigma). Separation of organic and aqueous layers was achieved via centrifugation at 1,000g for 5 min at 4 °C. Secondary extraction of the aqueous layer was performed using 0.1% formic acid followed by addition of 2 ml

chloroform and further centrifugation. After combining the organic extractions, the lipid-containing mixture was dried under nitrogen (N2) and dissolved in 120 µl chloroform. Single-reaction monitoring (SRM) liquid chromatography–coupled to tandem mass spectrometry (LC-MS/MS)—on an Agilent 6400 series QQQ using 10 µl of sample—was achieved using a reverse-phase C5 column (Phenomenex, Luna 50 mm × 4.6 mm, 5-µm particle diameter). Mobile phases were buffer A (composed of 95:5 water:methanol) and buffer B (60:35:5 2-propanol:methanol:water). Solvent modifiers were 0.1% formic acid with 5 mM ammonium formate or 0.1% ammonium hydroxide for positive and negative ionization modes, respectively. For polar metabolites, frozen tissue was homogenized using a TissueLyser in 300 µl of 40:40:20 acetonitrile:methanol:water with the addition of 1 nM (final concentration) of D3-[15N]serine as an internal extraction standard (Cambridge Isotopes Laboratories Inc, DNLM-6863). 10 µl of cleared supernatant (via centrifugation at 15,000 r.p.m., 10 min, at 4 °C) was used for SRM–LC-MS/MS using a normal-phase Luna NH2 column (Phenomenex). Mobile phases were buffer A (composed of 100% acetonitrile) and buffer B (composed of 95:5 water:acetonitrile). Solvent modifiers were 0.1% formic acid or 0.2% ammonium hydroxide with 50 mM ammonium acetate for positive and negative ionization modes, respectively. All metabolites were analyzed using the MassHunter software package (Agilent Technologies) by quantifying the transition from parent precursor mass to product ions for each individual metabolite.

Gene expression analysis. TCGA breast-invasive carcinoma data set was sourced from data generated by TCGA Research Network (http://cancergenome.nih.gov), made

available on the University of California, Santa Cruz (UCSC) Cancer Browser. Series matrix files for ISPY1 (accession code GSE22226) and a neoadjuvant chemotherapy–treated cohort (accession code GSE25066) were downloaded from the Gene Expression Omnibus (GEO) site and processed using the GEOquery R package[10,11,23]. A chemotherapy-naive cohort and an aggressively treated early-stage cohort were obtained from the UCSC Cancer Browser[12,13]. Multiple probes corresponding to the same gene were collapsed using the 'MaxMean' method in the weighted correlation network analysis (WGCNA) R package[24,25]. A fatty acid metabolism gene set was compiled using genes containing the Gene Ontology term, GO:0006631 (http://geneontology.org). An average expression profile (centroid) of these genes was calculated for the triple- negative subset of samples within the breast-invasive carcinoma data set from TCGA. Similarities between this centroid and the gene expression profiles of samples from the four independent clinical cohorts were then quantified using a Pearson correlation metric. Heat maps and clustering analyses were performed using the 'gplots' (http://cran.r-project.org/web/packages/gplots/index.html) and 'cluster' (http://cran.r-project.org/web/packages/cluster/index.html) R packages respectively. To generate Kaplan-Meier plots, samples were grouped by receptor status and dichotomized by ACC2 expression at an optimal threshold, yielding groups with the most significant difference in distant recurrence-free survival based on the log-rank test. Kaplan-Meier plots were then generated for the respective groups using the 'survival' (http://cran.r-project.org/web/packages/survival/ index.html) R package. Univariate Cox proportional-hazards regression analysis was performed using the 'survival' R package to assess the correlation of fatty acid metabolism gene expression to distant recurrence-

free survival in the pooled neoadjuvant chemotherapy–treated cohort[11]. This was conducted for all tumors, TN tumors and RP tumors.

Cell lines and propagation. A panel of established TN and RP human breast cancer cell lines, and their culture conditions, have previously been described[15]. Primary human mammary epithelial (HMEC) cells were derived from histologically normal breast tissues and cultured as previously described[26]. The cells were infected with a lentivirus expressing shRNA specific for the p16 isoform–encoding sequence of CDKN2A (as meant by 'p16 shRNA') and were then infected with the pBabe-MycER virus and named B1389-shp16-MycER (HMECMYC-ER) cells, as previously described[27,28]. Although expression of p16 shRNA delays senescence, the cells are not immortalized and undergo spontaneous senescence when continuously cultured. Therefore, these cells were not used beyond 12 passages after their derivation. HMECMYC-ER cells were treated with 4-hydroxytamoxifen (TAM) at 500 nM to induce MYC activation. RP (HCC1428 and T47D) cells stably overexpressing MYC have been previously described[1]. No cell line used in this paper is listed in the database of commonly misidentified cell lines that is maintained by the International Cell Line Authentication Committee (ICLAC) (http://iclac.org/databases/cross-contaminations/). All lines were found to be negative for mycoplasma contamination.

Immunoblot analysis. Proteins were extracted using RIPA buffer (50 mM Tris-HCl pH 7.6, 150 mM NaCl, 0.5% sodium deoxycholate, 1% Triton X-100, 0.1% SDS, 2 mM EDTA) and proteinase (Roche) plus phosphatase (Roche) inhibitor cocktails. Protein

extracts were resolved using 4–12% SDS-PAGE gels (Life Technologies) and transferred to nitrocellulose membranes (Life Technologies). Membranes were probed with primary antibodies overnight on a 4 °C shaker, then incubated with horseradish peroxidase (HRP)-conjugated secondary antibodies, and signals were visualized with ECL (Bio-Rad). The primary antibodies targeting the following proteins were used: β-actin (actin) (sc-47778 HRP, Santa Cruz, 1:10,000), PGC-1α (ab54481, Abcam, 1:500), BBOX1 (WH0008424M1, Sigma-Aldrich, 1:500), CPT2 (ab71435, Abcam, 1:500), FASN (SAB1403807, Sigma-Aldrich, 1:1,000), pACC1/2 (11818, Cell Signaling, 1:1,000), ACC1 (4190, Cell Signaling, 1:1,000), ACC2 (8578, Cell Signaling, 1:1,000), AMPK (2532, Cell Signaling, 1:1,000), pAMPK (2535, Cell Signaling, 1:1,000) and c-MYC (MYC) (ab32072, Abcam, 1:1,000).

ATP and NAD(P)H quantification. To determine the effects of etomoxir treatment on ATP levels, tumor cells were seeded in 96-well plates at 5,000–7,000 cells per well and cultured in the presence of 0 or 200 μM etomoxir (Sigma-Aldrich) for 48 h, with triplicate samples for each condition. Relative ATP concentrations were determined using the CellTiter-Glo Luminescent Cell Viability Assay (Promega). To determine the effects of etomoxir treatment on NAD(P)H levels, HMECMYC-ER cells were seeded in 96-well plates at 2,000 cells/well and cultured in the presence of 0 or 500 nM TAM for 48 h, then with 0 or 200 μM etomoxir for 24 h, with six samples for each condition. Relative NAD(P)H concentration was determined using CellTiter-Glo 96 AQueous One Solution Cell Proliferation Assay (Promega).

Fatty acid oxidation assay. To determine relative fatty acid oxidation pathway activity, tumor cells were seeded in 24-well plates at 100,000 cells/well in triplicate. Cells were incubated in serum-free medium for 2 h and then incubated in standard medium for 1 h. [^{14}C]oleic acid (Moravek Biochemicals, MC406) at 0.1 μCi/μl was added, 2 × 2 cm squares of Whatman paper were taped over the wells, and the cells were incubated for 3 h at 37 °C. After adding 200 μl 3 M NaOH directly to each square of Whatman paper, 100 μl 70% perchloric acid was added to each well and CO2 was captured at room temperature for 1 h. The Whatman paper was dried at room temperature and placed in a scintillation vial with 5 ml scintillation fluid. ^{14}C radioactivity was measured using a liquid scintillation counter and normalized to protein concentration.

RNAi knockdown. MYC-specific (L-003282-02-0005), CPT2-specific (M-008574-01-005) and nontargeting (D-001810-10-20) siRNAs were purchased from GE Dharmacon (SMARTpool, four siRNAs per gene). 30 pmol siRNA was used to transfect cells with the Lipofectamine RNAiMAX Transfection Reagent (Life Technologies), according to the manufacturer's instructions. Cells were incubated with siRNA for 72 h. For siMYC studies, medium was changed at 24 h, and 0 and 200 μM etomoxir was added for 48 h before ATP levels were quantified as described above. For siCPT2 studies, the relative number of cells was determined at 72 h as described below. The CPT1-knockdown data was extracted from the Project Achilles data set[17]. The viability score represents the ATARiS solution, which is the computationally derived score that quantifies the gain or loss of growth specific to knockdown of the gene from pooled shRNA screens.

Proliferation and viability assays. To determine the effects of etomoxir treatment on cell proliferation, cells were seeded in 6-well plates at 100,000–150,000 cells/well and cultured in the presence of 0 or 200 μM etomoxir. Cells were harvested at 24, 48 and 72 h. Cell counts were determined using the Countess Automated Cell Counter (Life Technologies) according to the manufacturer's instructions. Cell viability was assessed by performing the flow cytometry–based Guava ViaCount viability assay (Millipore) according to the manufacturer's instructions. To determine the effects of siCPT2 treatment on cell proliferation, cells were seeded in 6-well plates at 100,000–150,000 cells per well and transfected with siNT or siCPT2 as described above. Cells were harvested at 24, 48 and 72 h, and cell counts were determined using the Countess Automated Cell Counter (Life Technologies) according to the manufacturer's instructions. Three independent biological replicates were performed for each time point and condition.

Matrix detachment assays. To determine the effects of matrix detachment, cells were seeded in ultra-low adhesion round-bottom 96-well plates at 1,000 cells/well. Sphere formation was judged by bright-field imaging 4 d after seeding, and then spheres were subsequently cultured in 0 or 200 μM etomoxir for 48 h, with triplicate samples for each condition. Relative ATP concentrations were determined as described above.

Glucose-starvation assays. To determine the effects of glucose starvation, cells were seeded in 96-well plates at 5,000–7,000 cells/well and cultured in replete medium, glucose-depleted medium, 200 μM etomoxir or glucose-depleted medium with 200 μM

etomoxir for 24 h, with triplicate samples for each condition. Relative ATP concentration was determined as described above.

Orthotopic allograft and xenograft studies. 4-week-old WT FVB/N and immunocompromised NOD/SCID female mice were purchased from Taconic Biosciences. The derivation of HCI-002 and HCI-009 TN patient–derived xenograft tumors has been previously described[22]. Viably frozen MTB-TOM, HCI-002 and HCI-009 tumor samples were transplanted into the cleared mammary fat pads of FVB/N and NOD/SCID mice, respectively. Tumor growth was monitored daily by caliper measurement in two dimensions. Researchers were not blinded to the treatment groups. For the [^{13}C]palmitate experiment (Fig. 1c), tumors were allowed to reach ~1.5 cm3, and then the mice were randomized into experimental groups. Mice received 100 mg/kg [^{12}C]palmitate or [^{13}C]palmitate, delivered by i.p. injection at t = 0 h. The palmitate solution was prepared by sonication into PEG-40 (Spectrum). Mice were euthanized at t = 4 h, following which tumors and contralateral non-tumor mammary glands were flash-frozen in liquid nitrogen. For the HCI-002 acute etomoxir-treatment experiment (Fig. 4b), tumors were allowed to reach ~1.5 cm3, and mice were then randomized into experimental groups. Mice received vehicle or 60 mg/kg etomoxir, delivered by i.p. injection, at t = 0 and 24 h. Mice were euthanized at t = 26 h, and the tumors were flash-frozen in liquid nitrogen. For the remaining in vivo studies, tumors were allowed to reach ~1 cm3; mice were then randomized into experimental groups, and drug treatment was initiated. For the MTB-TOM studies (Fig. 4d, Supplementary Fig. 9 and Supplementary Table 6), mice received vehicle or 20 or 40 mg/kg etomoxir, delivered by

i.p. injection, daily for 14 d. Tumor growth was monitored daily by caliper measurement. Mice were euthanized after 14 d of treatment or after tumors reached 2 cm in any dimension, following which the tumors were flash-frozen in liquid nitrogen. For the HCI-002 and HCI-009 studies (Fig. 4e,f), mice received vehicle, 40 or 60 mg/kg etomoxir, delivered by i.p. injection, daily for 21 d. Tumor growth was monitored daily by caliper measurement. Mice were euthanized after 21 d of treatment or after tumors reached 2 cm in any dimension; for the HCI-002 study, two pieces of tumor from separate locations were fixed in 4% paraformaldehyde (n = 5 for vehicle; n = 7 for 40 mg/kg; n = 4 for 60 mg/kg). The remaining tumor tissue was flash-frozen in liquid nitrogen.

Immunohistochemical analysis. PFA-fixed tumor samples were paraffin-embedded, and a tissue microarray of HCI-002 tumors was created using two 2-mm punch cores per tumor. Immunohistochemical staining of tissue microarrays for Ki-67 was performed using the MIB-1 antibody clone (1:50 dilution; DAKO, Carpinteria, CA, USA), after 20 min of antigen retrieval with epitope-retrieval solution 2 (Leica Biosystems, Buffalo Grove, IL, USA). Images were scored as the percentage of Ki-67+ tumor cell nuclei per total tumor cell nuclei in each captured field using Immunoratio software (http://jvsmicroscope.uta.fi/immunoratio/). TUNEL staining was performed using the ApopTag Peroxidase In situ Apoptosis Detection Kit (Millipore) according to the manufacturer's instructions. Images were scored as the total number of TUNEL+ cells per captured field. All quantification was performed in a fashion that was blinded to treatment group.

Statistical analysis. Prism software was used to generate and analyze Pearson correlations (Fig. 3f) and the survival plot (Fig. 4e). Correlation P values were generated using a two-sided t-test. Clade-enrichment P value was generated using a Fisher's exact test. Survival plot P value was generated using a log-rank test. All differential metabolite abundance and gene expression analyses were performed using the 'limma' R package. Differential metabolite abundance between MTB-TOM tumors and non-tumor mammary glands was performed using the limma R package[29]. Metabolites that were significantly different between these groups at a false- discovery rate of 0.05 were extracted for downstream analyses. Pathway enrichment within this set of metabolites was quantified using the 'MaxMean' method within the 'piano' R package[30], based on annotations from the Kyoto Encyclopedia of Genes and Genomes (KEGG; http://www.genome.jp/kegg/). Significantly enriched pathways were identified at a P value cutoff of 0.05. For all other comparisons, unpaired two-sided t-tests were used (GraphPad). No statistical method was used to predetermine sample size. The investigators were not blinded to allocation for the in vivo experiments. The investigators were blinded to allocation for immunohistochemical analyses. For all in vivo studies, mice were randomized to treatment groups when tumors reached a predetermined volume on a per experiment basis, as described above. For each data set, the data meet the assumptions of the statistical test used, as determined by distribution and variance. The sample size for all experiments (in vitro and in vivo) was not chosen with consideration of adequate power to detect a prespecified effect size. For in vitro studies, all completed experiments are reported. For in vivo studies, the number of indicated mice represents the total number of mice treated and processed for each experiment.

No samples were fully processed for metabolomic, western blot, or immunohistochemical analysis and then excluded. For the etomoxir-treatment studies, mice were euthanized at the ethical endpoint (~2 cm) or at the study endpoint, unless they failed to meet the predetermined UCSF Institutional Animal Care and Use Committee quality-of-life guidelines. No mice that completed the studies were excluded from analyses. In the prolonged PDX-etomoxir study (Fig. 4e), two mice from the vehicle group and one mouse from the 60 mg/kg experimental group were found dead of unknown causes, and these tumors were not included in further analyses.

Code availability. Publicly available data sets were acquired as noted. Our annotations of the data sets are available (https://bitbucket.org/jeevb/brca). All code used for this project has been deposited to Github (https://github.com/snjvb/fam_study).

Acknowledgements

This work was supported, in part, by the US Department of Defense–Congressionally Directed Medical Research Programs' Era of Hope Scholar award W81XWH-12-1-0272 (A.G.), the US National Institutes of Health (NIH) grant R01 CA170447 (A.G.), the Diabetes, Endocrinology and Metabolism training grant T32 DK007418 (R.C.), the Molecular and Cellular Mechanisms of Cancer training grant T32 CA108462 (A.Y.Z.) and the Atwater Foundation (A.G.). The authors thank A. Welm for guidance in the use of patient-derived xenografts, D. Lowe and A. Beardsley for technical guidance and helpful discussions, K.A. Fontaine for helpful discussions and comments on the manuscript, and S. Samson for a helpful consumer advocate perspective and guidance on our work.

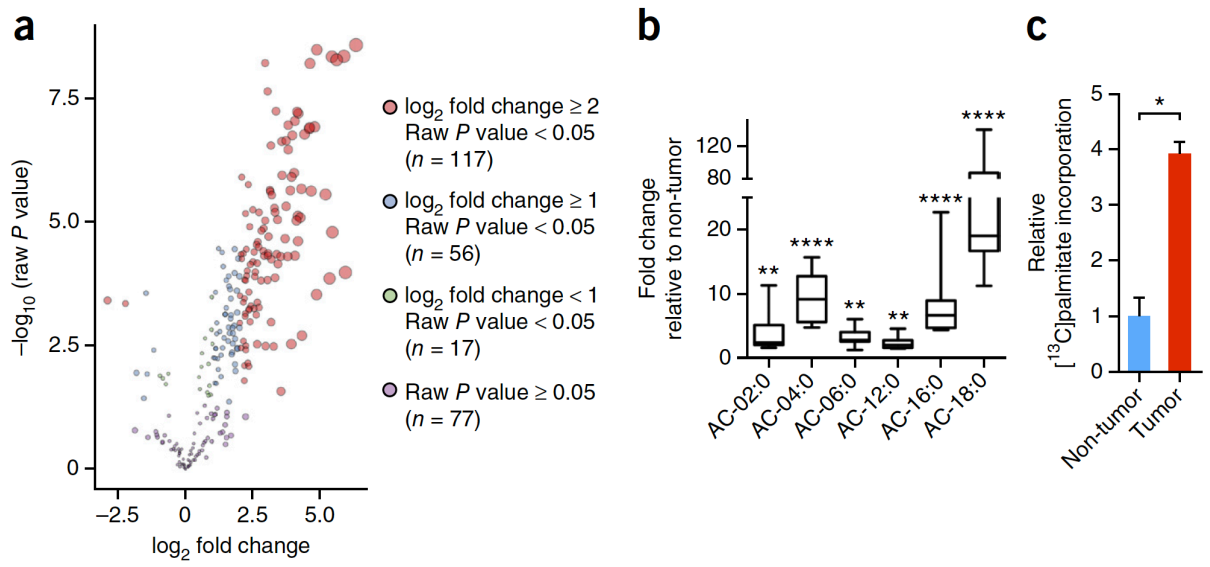

Figure 1. MTB-TOM tumors show dysregulated FAO. (a) Volcano plot for changes in metabolite concentrations in MTB-TOM tumors (seven tumors from five induced mice) as compared to those from non-tumor mammary glands (five mammary glands from four uninduced mice). (b) Fold change in acylcarnitine (AC) levels in MTB-TOM tumors versus non-tumor mammary glands, in the same mice as in a. Values are shown as minimum-to-maximum box plots. Error bars indicate range of smallest to largest value recorded. The x axis designations indicate acyl-carbon chain length followed by the location of any double bonds (e.g., 'AC-02:0' indicates a two-carbon acyl group with no double bonds). (c) [^{13}C]palmitoyl-carnitine production from [^{13}C]palmitate, as assessed by carbon flux analysis, in MTB-TOM orthotopic transplants, as compared to that in the contralateral non-tumor mammary gland in the same mouse (n = 4 mice). Throughout, the values shown are mean ± s.e.m. In c, a two-tailed unpaired t-test was used to compare non-tumor to tumor samples. In a,b, all differential metabolite-abundance analyses were performed using the 'limma' R package. *P < 0.05, **P < 0.01, ****P < 0.0001.

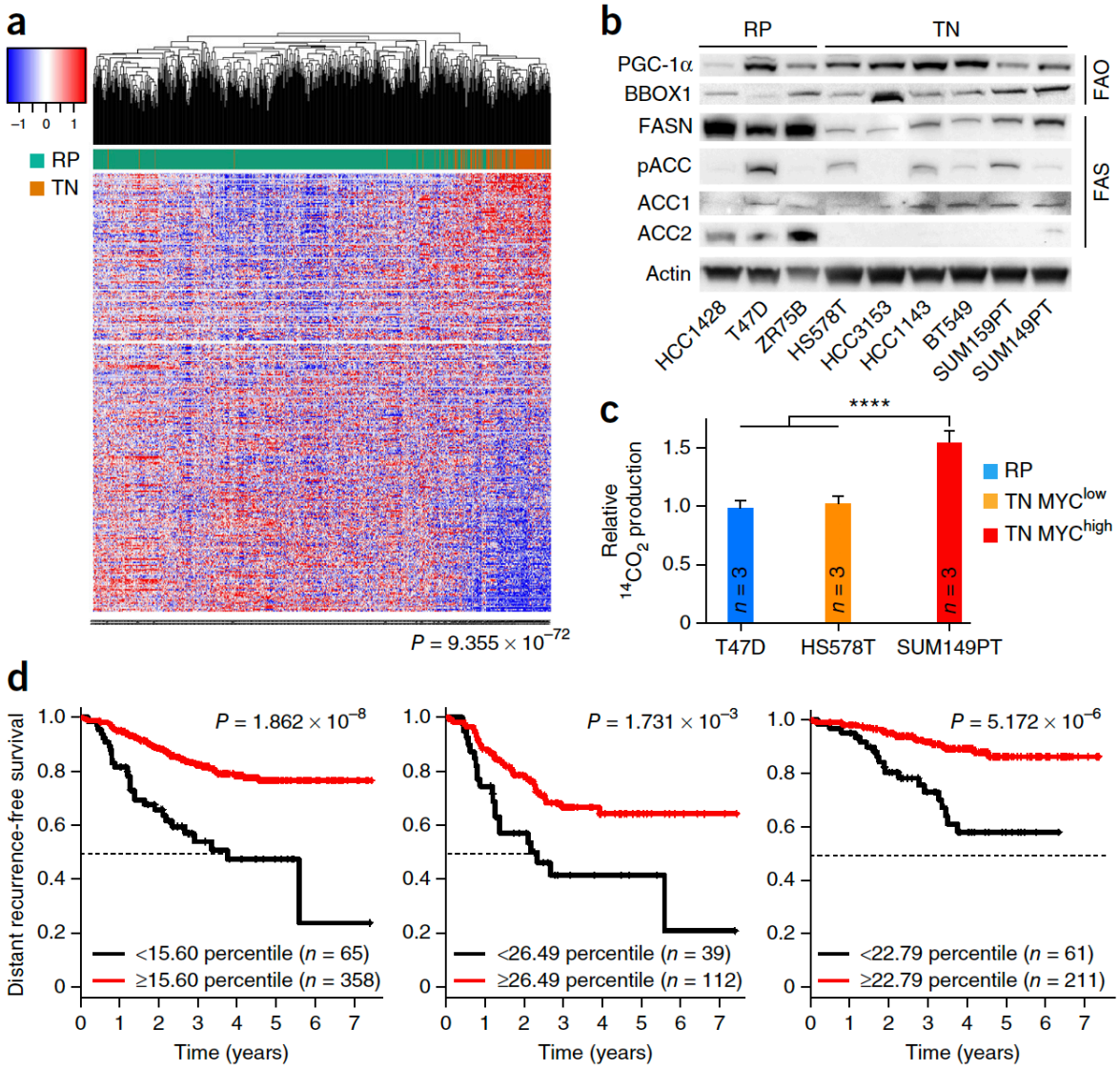

Figure 2. Human TNBC shows dysregulated FAO. (a) Hierarchical clustering of TCGA RNA-seq samples from 771 breast cancer patients for 336 fatty acid metabolism genes in TN and RP tumors. Individual gene expression is row-normalized from −1 (blue) to 1 (red). A Fisher's exact test was used to calculate the indicated P value, which demonstrated significant enrichment of genes in the clade indicated by a red box in TN tumors (116/123). (b) Immunoblot analysis showing expression levels of FAO activators PGC-1α and BBOX1 and of fatty acid synthesis enzymes FASN, ACC1, ACC2, and phosphorylated ACC1 and ACC2 (pACC) in a panel of TN and RP human cell lines (RP lines, n = 3; TN lines, n = 6). (c) Quantification of FAO assays in TN MYChigh, TN MYClow and RP cells. Relative 14CO2 production was normalized for each cell line to total protein levels. Values shown are mean ± s.e.m. A two-tailed unpaired t-test was used to compare non-tumor to tumor samples. ****P < 0.0001. (d) Kaplan-Meier survival graphs for all patients with tumors (left) or for those with TN (middle) or RP (right) tumors, from a pooled neoadjuvant chemotherapy–treated cohort

and grouped on the basis of ACACB (ACC2) mRNA expression at an optimal threshold indicated by percentile numbers. Samples with decreased ACACB expression are represented with black lines. Median survival times (MSTs) are indicated by the black dashed lines. For all tumors, ACACBlow MST = 3.76 years; for TN tumors, ACACBlow MST = 2.18 years; the MST was not reached in any other group. A log-rank test was used to calculate P values. In a, differential gene expression analyses were performed using the limma R package.

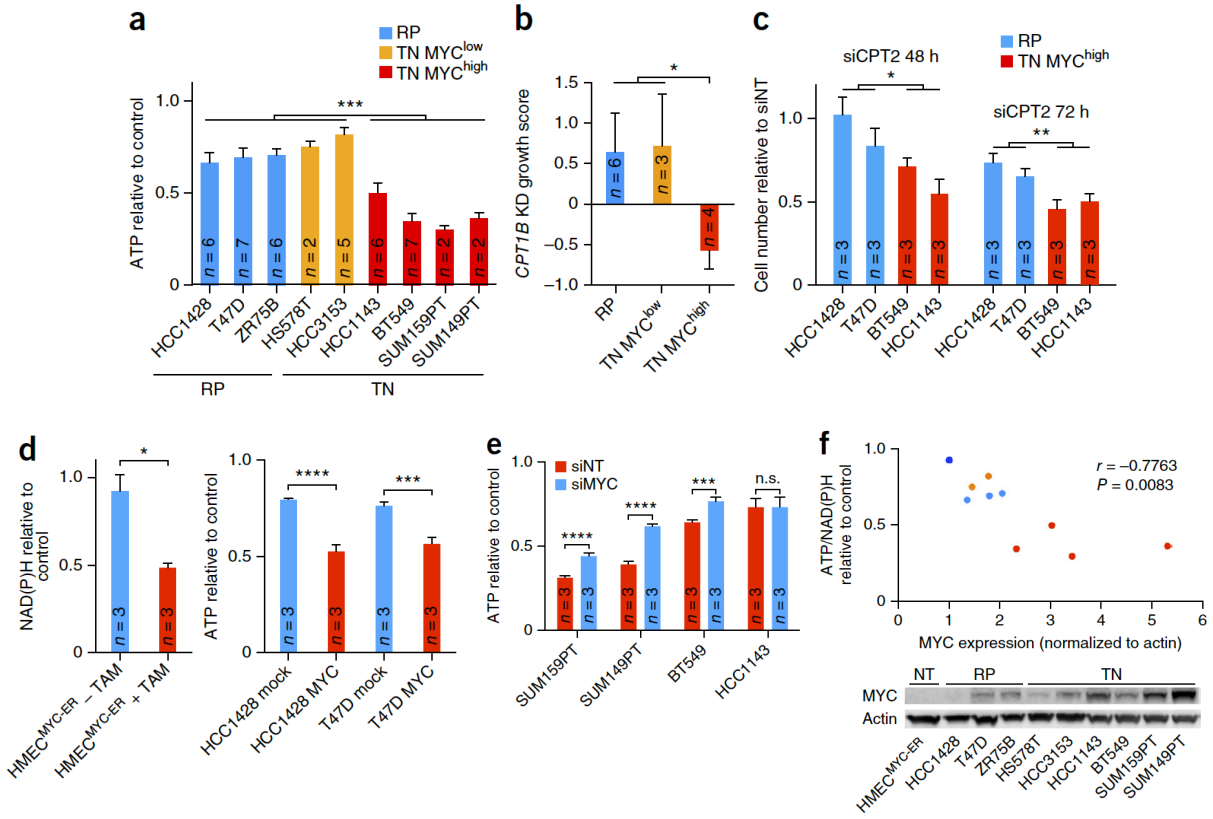

Figure 3. FAO inhibition has MYC-dependent bioenergetic effects in vitro. (a) ATP levels in TN MYC^{high}, TN MYC^{low} and RP cell lines relative to those in untreated (control) cells or in cells treated with 200 μM etomoxir for 48 h. (b) Growth response of an independent panel of TN MYC^{high}, TN MYC^{low} and RP cell lines treated with a pool of shRNAs targeting CPT1B. KD, knockdown. (c) Proliferation response of TN MYC^{high} and RP cell lines to siRNA-mediated CPT2 knockdown, 48 h and 72 h after siRNA transfection, relative to that of cells transfected with a nontargeting control siRNA (siNT). (d) Left, NAD(P)H levels in HMEC^{MYC-ER} cells ± MYC activation for 48 h, followed by treatment ± 200 μM etomoxir for 24 h. Bars represent NAD(P)H levels relative to those in control (etoxomir-untreated) cells. Right, ATP levels in RP cell lines ± MYC overexpression, following treatment ± 200 μM etomoxir for 48 h. Red bars indicate MYC-induced or MYC^{high} cells; blue bars indicate MYC^{low} cells. (e) ATP levels in TN MYC^{high} cells in the presence (siMYC) or absence (siNT) of siRNA-mediated MYC knockdown ± treatment with 200 μM etomoxir for 48 h. Bars represent ATP levels relative to those in control (etoxomir-untreated) cells. (f) Top, correlation of MYC protein expression and mean ATP/NAD(P)H response to etomoxir treatment in TN and RP cell lines in a and in HMEC^{MYC-ER} cells without MYC in b. Pearson correlation and two-tailed t-test were used to generate the correlation coefficient and associated P value. The color code is the same as in a, except that HMEC^{MYC-ER} cells are indicated in dark blue. Bottom, immunoblot analysis showing MYC protein levels in the indicated cell lines. Throughout, values shown are mean ± s.e.m. from triplicate samples (a,d,e), the indicated number of cell lines (b) or three biological replicates (c). The number of

biological replicates is indicated (a,c–e). A two-tailed unpaired t-test was used to compare experimental groups (a–e); *P ≤ 0.05, **P < 0.01, ***P < 0.001, ****P < 0.0001.

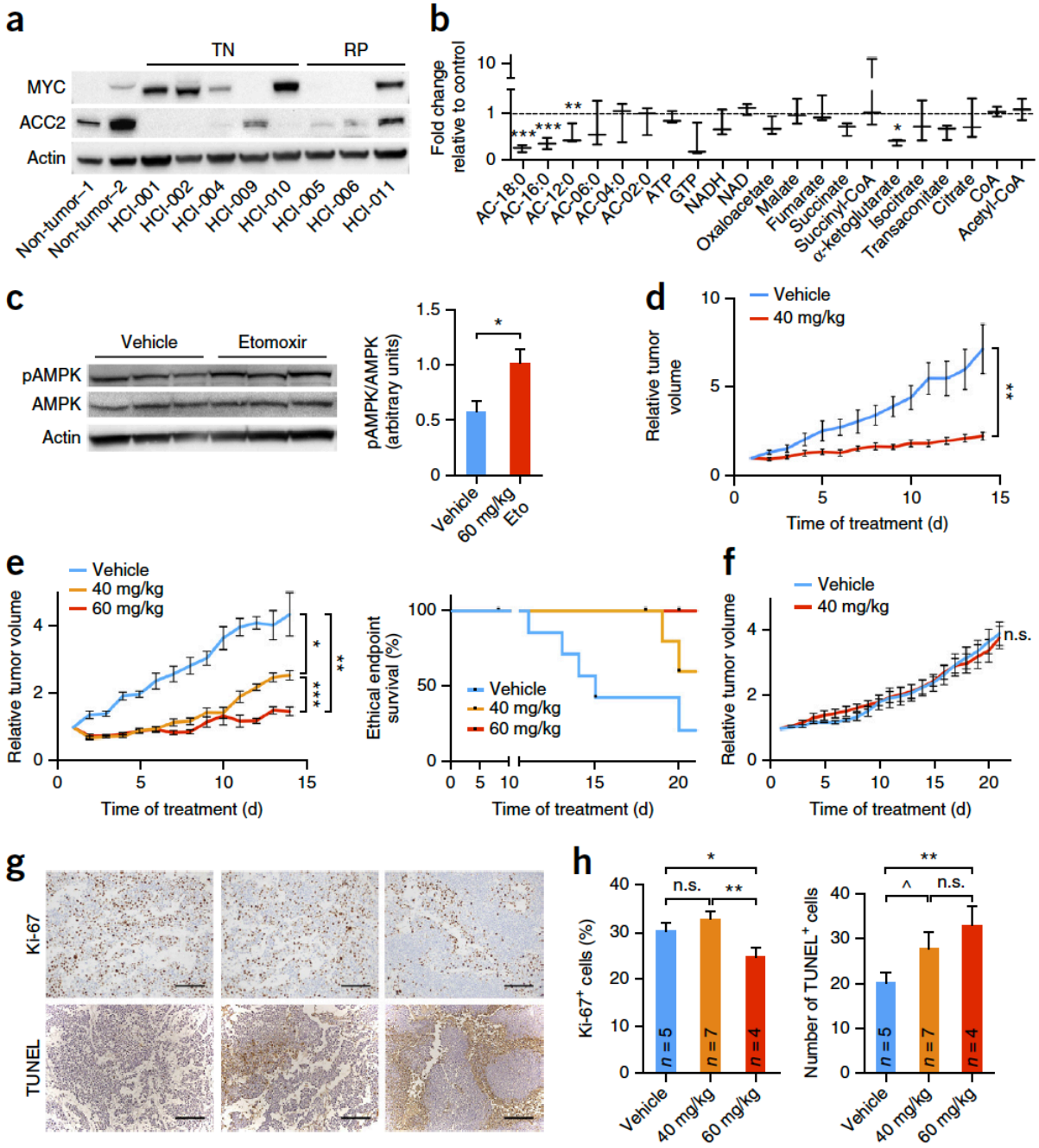

Figure 4. FAO inhibition has MYC-dependent bioenergetic and growth effects in vivo. (a) Immunoblot analysis of MYC and ACC2 protein expression in patient-derived xenografts from individuals with TN (n = 5) or RP (n = 3) tumors, as well as in human non-tumor reduction mammoplasty tissues (non-tumor–1 and non-tumor–2). (b) Fold change in metabolite levels in etomoxir-treated xenograft tumors (HCI-002) versus vehicle-treated tumors. Values are shown as minimum-to-maximum box plots for three mice in each group. (c) Left, immunoblot analysis of pAMPK and AMPK expression in etomoxir- or vehicle-treated HCI-002 tumors (n = 3 mice). Right, quantitation of the

pAMPK/AMPK ratio, normalized to β-actin levels. Eto, etomoxir. (d) Relative tumor volume of orthotopic MTB-TOM (MYC^{high}) tumor allografts in FVB/N mice that were treated with vehicle (n = 6 mice) or etomoxir (40 mg/kg; n = 7 mice) daily for 14 d. (e) Left, relative tumor volume of orthotopic HCI-002 (MYC^{high}) xenografts in NOD/SCID mice that were treated with vehicle (n = 7) or with 40 mg/kg (n = 5) or 60 mg/kg (n = 5) etomoxir daily for 21 d. Right, Kaplan-Meier analysis of mice with HCI-002 xenografts that were treated with vehicle (n = 7) or with 40 mg/kg (n = 5) or 60 mg/kg (n = 5) etomoxir. Ethical endpoint survival indicates the percentage of mice bearing xenografts <2 cm in size. P = 0.0045 by log-rank test. (f) Relative tumor volume of orthotopic HCI-009 (MYC^{low}) xenografts in NOD/SCID mice that were treated with vehicle or etomoxir (40 mg/kg) daily for 21 d (n = 3 mice per group). (g,h) Representative (of three high-powered (20×) fields from two separate areas of each tumor) Ki-67 (top) and TUNEL (bottom) staining of HCI-002 tumors in mice (killed at the end of the study) that were treated with vehicle (left) or with 40 mg/kg (middle) or 60 mg/kg (right) etomoxir (g) and quantification of Ki-67+ cells/field (h, left) and TUNEL+ cells/field (h, right). The number of mice analyzed in each treatment group is indicated in h. Scale bars, 200 μm. In b, all differential metabolite abundance analyses were performed using the limma R package. Unless otherwise specified, values shown are mean ± s.e.m. In d–f, tumor volume is shown relative to tumor volume on day 1 of treatment. A two-tailed unpaired t-test was used to compare experimental groups (c–g); ^P ≤ 0.10, *P ≤ 0.05, **P < 0.01, ***P < 0.001; n.s., not significant.

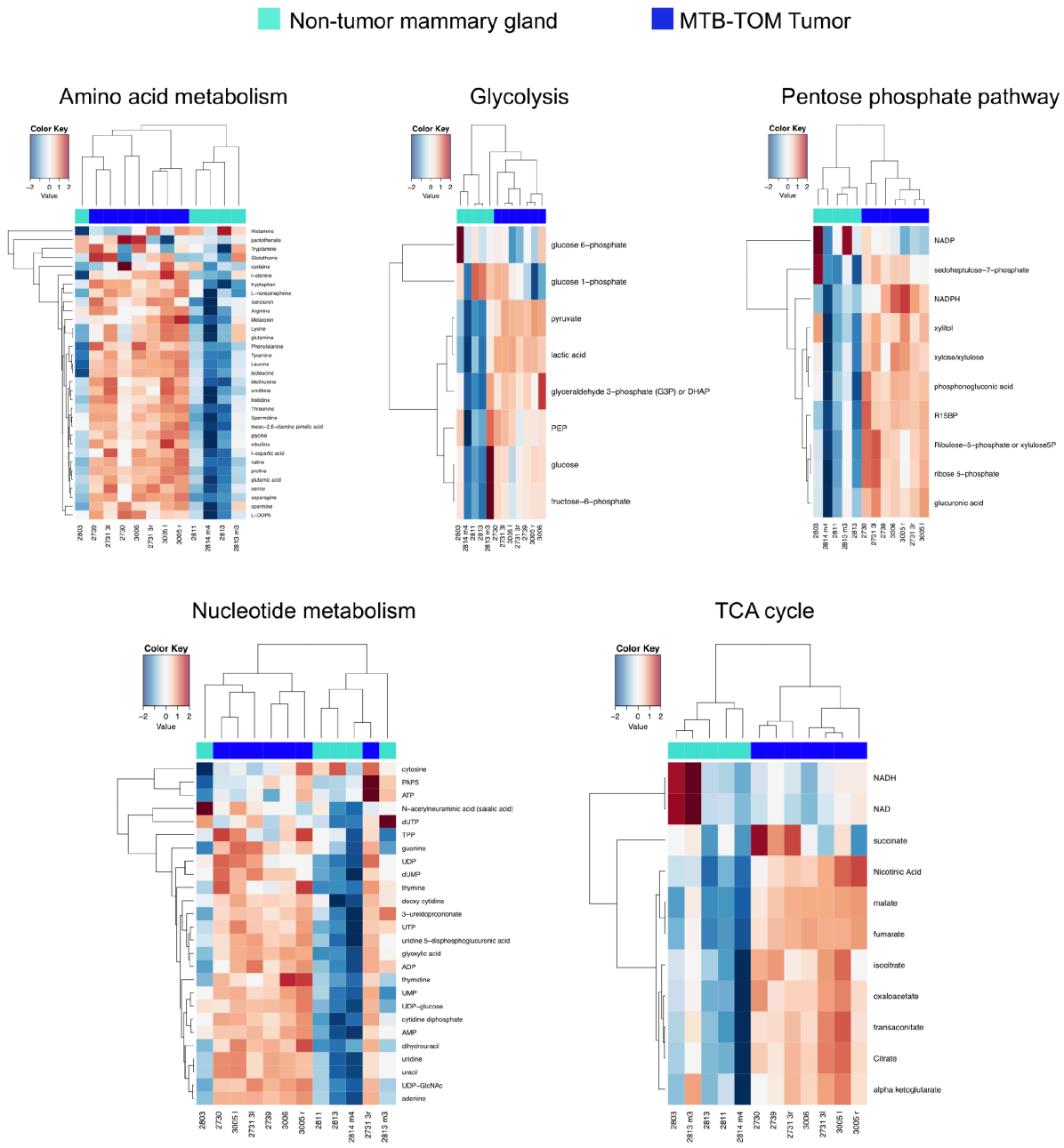

Supplemental Figure 1. Metabolic pathway alterations in MTB-TOM tumors compared to non-tumor mammary glands. Differential abundance of metabolites in five metabolic pathways commonly associated with tumorigenesis (amino acid, nucleotide, glycolysis, TCA cycle and pentose phosphate pathway) is shown. Detected metabolites were grouped by pathway (although many of these metabolites are intermediates in multiple pathways), and unbiased hierarchical clustering was used to display relative abundance of metabolites in MTB-TOM tumor versus non-tumor mammary gland. All differential metabolite abundance analyses were performed using the limma R package.

Supplemental Figure 2. Correlation analyses of TN and RP tumors to TCGA TN fatty acid metabolism centroid. A matrix of average fatty acid metabolism expression values was calculated for TCGA TN tumors. A sample-wise correlation analysis within each cohort against the TCGA TN centroid reveals the expression pattern to be significantly TN-specific (for P-values see Supplementary Table 3).

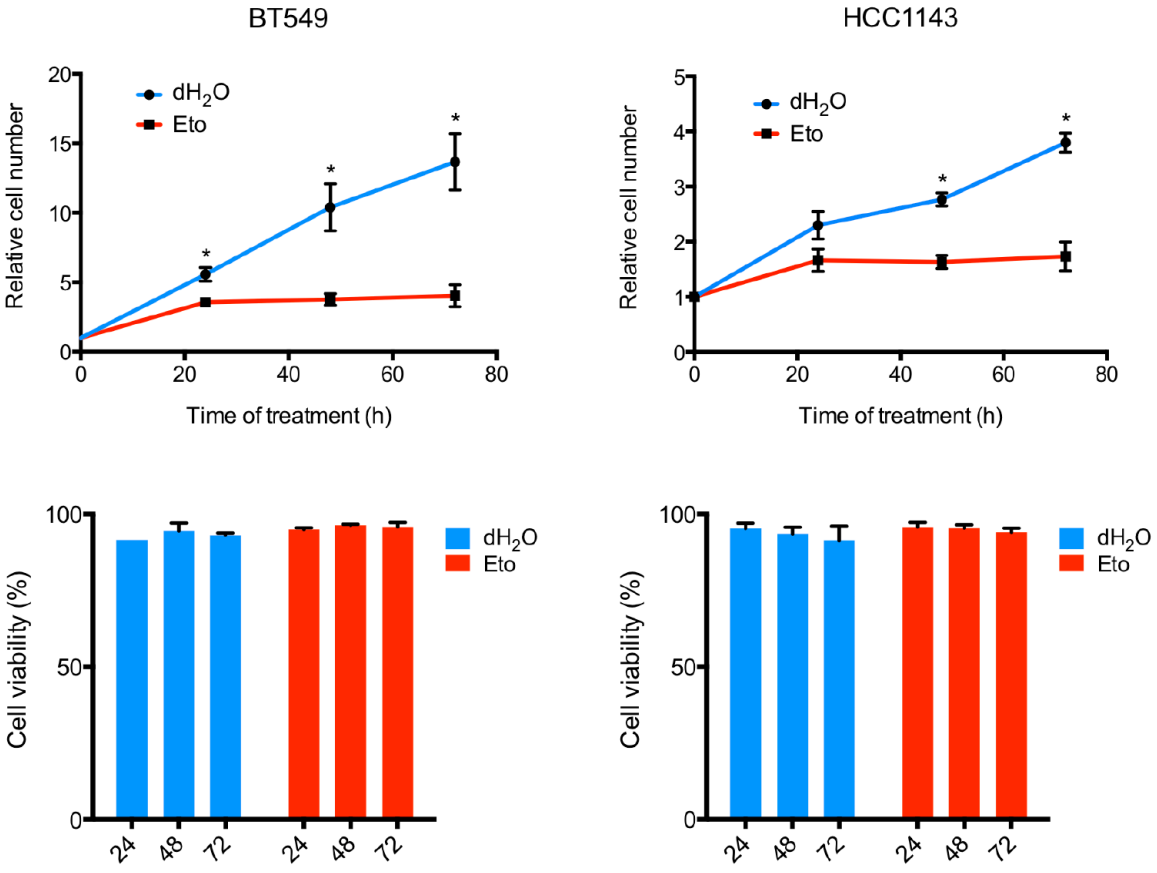

Supplemental Figure 3. Effect of etomoxir on TNBC cell proliferation and viability. Indicated cell types were treated with vehicle (dH2O) or 200 μM etomoxir for 24, 48 or 72 h. Cell growth plots showing effect of etomoxir on proliferation. Viability assay showing effect of etomoxir on viability. A two-tailed unpaired t-test was used to compare etomoxir-treated (red) to untreated (blue) cells. Values shown are mean ± s.e.m. from three biological replicates. *P ≤ 0.05

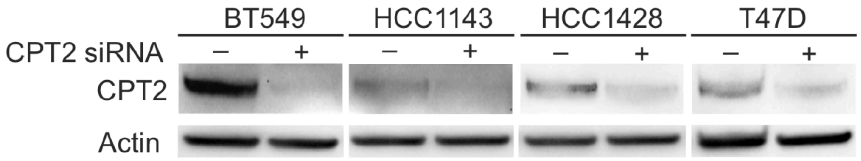

Supplemental Figure 4. CPT2 knockdown. Indicated cell types were treated with 30 pmol of CPT2 (M- 008574-01) or non-targeting (D-001810-10-20) siRNA pool for 72 h, then examined by immunoblotting for indicated protein expression.

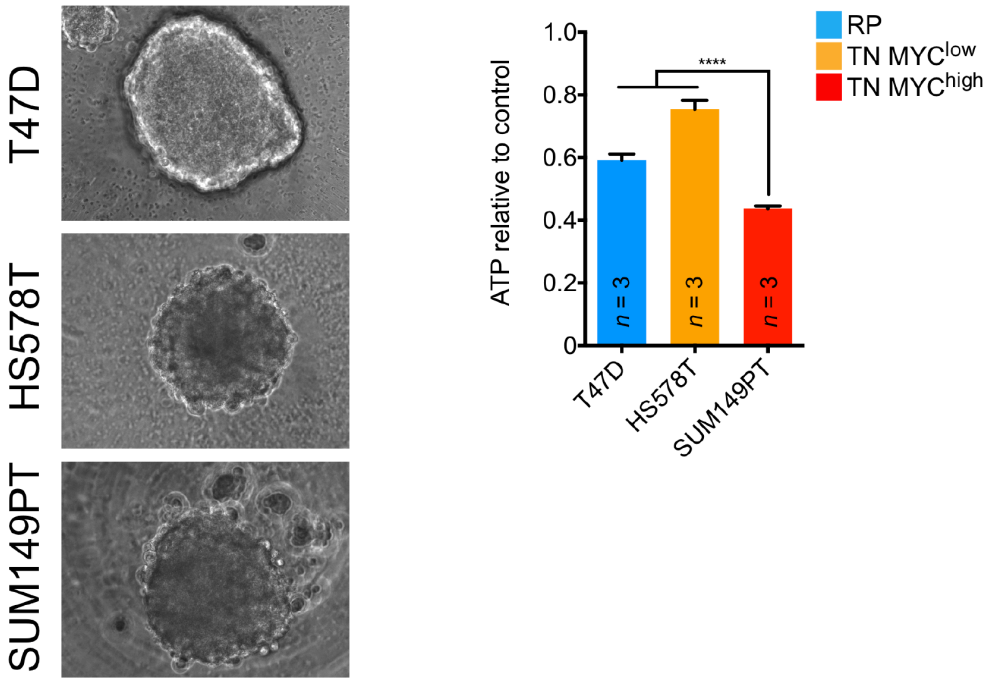

Supplemental Figure 5. Effects of matrix detachment on TN MYC^{high}, TN MYC^{low} and RP cells. Brightfield images of indicated cell lines 4 d after being seeded in ultra-low adhesion plates. After 4 d, indicated cell types were treated with 200 μM etomoxir or vehicle control for 48 h and ATP was measured. A two-tailed unpaired t-test was used to compare response of etomoxir-treated to untreated cells. Values shown are mean ± s.e.m. from five technical replicates. Number of biological replicates is indicated. ****P < 0.0001

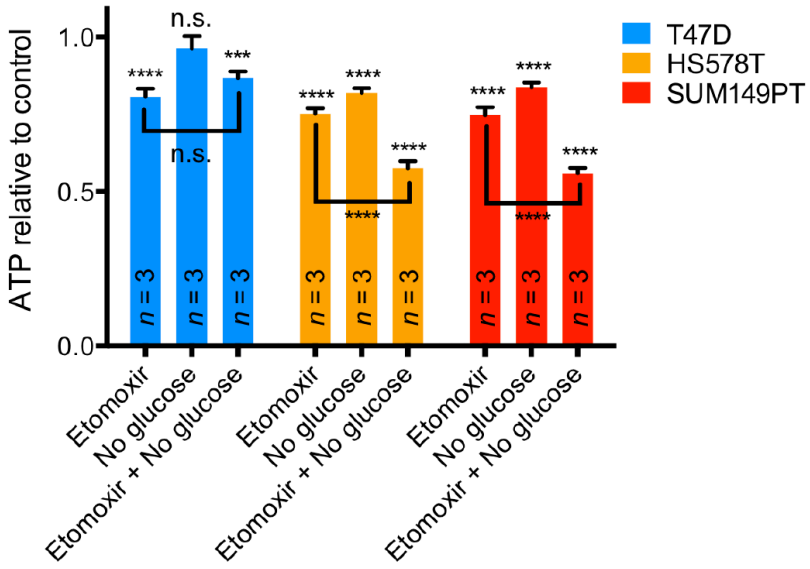

Supplemental Figure 6. Effects of glucose starvation and/or etomoxir on TN MYC^{high}, TN MYC^{low} and RP cells. Indicated cell types were treated with glucose-depleted medium and/or 200 μM etomoxir or vehicle control for 24 h and ATP was measured. A two-tailed unpaired t-test was used to compare response of treated to untreated cells. Values shown are mean ± s.e.m. from triplicate samples. Number of biological replicates is indicated. ***P < 0.001, ****P < 0.0001

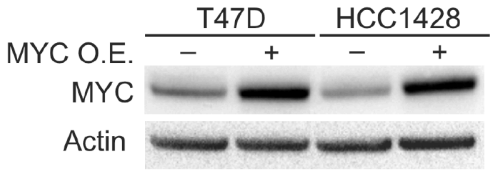

Supplemental Figure 7. MYC overexpression. Indicated cell types were examined by immunoblotting for indicated protein expression.

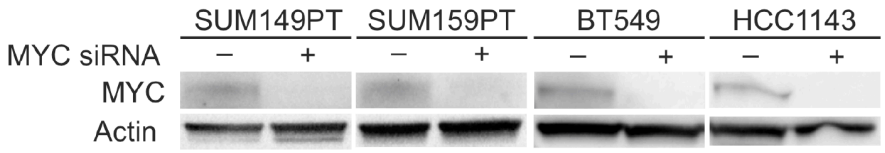

Supplemental Figure 8. MYC knockdown. Indicated cell types were treated with 30 pmol of MYC (L- 003282-02-0005) or non-targeting (D-001810-10-20) siRNA pool for 72 h, then examined by immunoblotting for indicated protein expression.

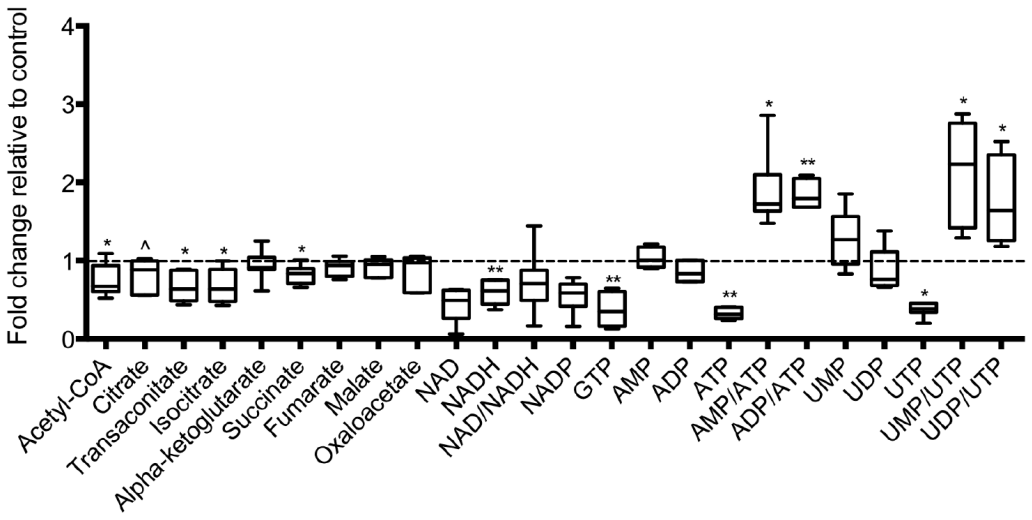

Supplemental Figure 9. Effects of etomoxir on metabolite levels in MTB-TOM tumors. MTB-TOM allografts were treated with 20 mg/kg daily via IP injection for 14 d. Fold change in metabolite levels in etomoxir-treated xenografts versus vehicle-treated tumors are shown. A two-tailed unpaired t-test was used to compare metabolite levels in etomoxir-treated to untreated tumors. Values are shown as min-to-max box plots from six mice in the control group and seven mice in the etomoxir-treated group. ^$P \leq 0.10$, *$P \leq 0.05$, **$P < 0.01$

Supplemental tables 1-6

All supplemental tables can be found using the following link:

https://www.nature.com/articles/nm.4055#supplementary-information

References

1. Horiuchi, D. et al. MYC pathway activation in triple-negative breast cancer is synthetic lethal with CDK inhibition. J. Exp. Med. 209, 679–696 (2012).

2. Koboldt, D.C. et al. Comprehensive molecular portraits of human breast tumors. Nature 490, 61–70 (2012).

3. Hu, S. et al. [^{13}C]pyruvate imaging reveals alterations in glycolysis that precede c-Myc–induced tumor formation and regression. Cell Metab. 14, 131–142 (2011).

4. Wahlström, T. & Henriksson, M.A. Impact of MYC in regulation of tumor cell metabolism. Biochim. Biophys. Acta 1849, 563–569 (2015).

5. D'Cruz, C.M. et al. c-MYC induces mammary tumorigenesis by means of a preferred pathway involving spontaneous Kras2 mutations. Nat. Med. 7, 235–239 (2001).

6. Pfefferle, A.D. et al. Transcriptomic classification of genetically engineered mouse models of breast cancer identifies human subtype counterparts. Genome Biol. 14, R125 (2013).

7. Carracedo, A. et al. A metabolic prosurvival role for PML in breast cancer. J. Clin. Invest. 122, 3088–3100 (2012).

8. Zaugg, K. et al. Carnitine palmitoyltransferase 1C promotes cell survival and tumor growth under conditions of metabolic stress. Genes Dev. 25, 1041–1051 (2011).

9. Bonnefont, J.P. et al. Carnitine palmitoyltransferases 1 and 2: biochemical, molecular and medical aspects. Mol. Aspects Med. 25, 495–520 (2004).

10. Esserman, L.J. et al. Chemotherapy response and recurrence-free survival in neoadjuvant breast cancer depends on biomarker profiles: results from the I-SPY

1 TRIAL (CALGB 150007/150012; ACRIN 6657). Breast Cancer Res. Treat. 132, 1049–1062 (2012).

11. Hatzis, C. et al. A genomic predictor of response and survival following taxane-anthracycline chemotherapy for invasive breast cancer. JAMA 305, 1873–1881 (2011).

12. Yau, C. et al. A multigene predictor of metastatic outcome in early-stage hormone receptor–negative and triple-negative breast cancer. Breast Cancer Res. 12, R85 (2010).

13. Chin, K. et al. Genomic and transcriptional aberrations linked to breast cancer pathophysiologies. Cancer Cell 10, 529–541 (2006).

14. Morris, E.M. et al. PGC-1α overexpression results in increased hepatic fatty acid oxidation with reduced triacylglycerol accumulation and secretion. Am. J. Physiol. Gastrointest. Liver Physiol. 303, G979–G992 (2012).

15. Neve, R.M. et al. A collection of breast cancer cell lines for the study of functionally distinct cancer subtypes. Cancer Cell 10, 515–527 (2006).

16. Holubarsch, C.J.F. et al. A double-blind randomized multicenter clinical trial to evaluate the efficacy and safety of two doses of etomoxir, in comparison with placebo, in patients with moderate congestive heart failure: the ERGO (etomoxir for the recovery of glucose oxidation) study. Clin. Sci. 113, 205–212 (2007).

17. Cowley, G.S. et al. Parallel genome-scale loss-of-function screens in 216 cancer cell lines for the identification of context-specific genetic dependencies. Sci. Data 1, 140035 (2014).

18. Jeon, S.M., Chandel, N.S. & Hay, N. AMPK regulates NADPH homeostasis

to promote tumor cell survival during energy stress. Nature 485, 661–665 (2012).

19. Schafer, Z.T. et al. Antioxidant and oncogene rescue of metabolic defects caused by loss of matrix attachment. Nature 461, 109–113 (2009).

20. Shen, L. et al. Metabolic reprogramming in triple-negative breast cancer through Myc suppression of TXNIP. Proc. Natl. Acad. Sci. USA 112, 5425–5430 (2015).

21. Bensaad, K. et al. Fatty acid uptake and lipid storage induced by HIF-1α contribute to cell growth and survival after hypoxia-reoxygenation. Cell Rep. 9, 349–365 (2014).

22. DeRose, Y.S. et al. Tumor grafts derived from women with breast cancer authentically reflect tumor pathology, growth, metastasis and disease outcomes. Nat. Med. 17, 1514–1520 (2011).

23. Davis, S. & Meltzer, P.S. GEOquery: a bridge between the Gene Expression Omnibus (GEO) and BioConductor. Bioinformatics 23, 1846–1847 (2007).

24. Langfelder, P. & Horvath, S. WGCNA: an R package for weighted correlation network analysis. BMC Bioinformatics 9, 559 (2008).

25. Langfelder, P. & Horvath, S. Fast R functions for robust correlations and hierarchical clustering. J. Stat. Softw. 46, i11 (2012).

26. Mukhopadhyay, R. et al. Promotion of variant human mammary epithelial cell outgrowth by ionizing radiation: an agent-based model supported by in vitro studies. Breast Cancer Res. 12, R11 (2010).

27. Narita, M. et al. Rb-mediated heterochromatin formation and silencing of E2F target genes during cellular senescence. Cell 113, 703–716 (2003).

28. Littlewood, T.D., Hancock, D.C., Danielian, P.S., Parker, M.G. & Evan, G.I. A modified estrogen receptor ligand-binding domain as an improved switch for the regulation of heterologous proteins. Nucleic Acids Res. 23, 1686–1690 (1995).

29. Smyth, G.K. in Bioinformatics and Computational Biology Solutions Using R Bioconductor (eds. Gentleman, R., Carey, V.J., Huber, W., Irizarry, R.A. & Dudoit, S.) 397–420 (Springer, 2005).

30. Väremo, L., Nielsen, J. & Nookaew, I. Enriching the gene set analysis of genome-wide data by incorporating directionality of gene expression and combining statistical hypotheses and methods. Nucleic Acids Res. 41, 4378–4391 (2013).

Chapter 3

Tumor cell-adipocyte gap junctions activate lipolysis and are essential for breast tumorigenesis

Summary

During tumorigenesis, a heterotypic interface exists between cancer and stromal cells that can both support and repress tumor growth. In the breast, studies have demonstrated a pro-tumorigenic role for adipocytes. However, the molecular mechanisms by which breast cancer cells coopt adipocytes remain elusive. Studying breast tumors and normal adjacent tissue (NAT) from several patient cohorts and mouse models, we show that lipolysis and lipolytic signaling are activated in NAT. We investigate the tumor-adipocyte interface and find that functional gap junctions form between breast cancer cells and adipocytes. As a result, cAMP, a critical lipolysis-inducing signaling molecule, is transferred from breast cancer cells to adipocytes and activates lipolysis in a gap junction-dependent manner; a fundamentally new mechanism of lipolysis activation in adipocytes. We find that gap junction formation depends upon connexin 31 (Cx31), and that Cx31 is essential for breast tumor growth and activation of lipolysis in vivo. Thus, direct tumor cell-adipocyte interaction is critical for tumorigenesis and may serve as a new therapeutic target in breast cancer.

Results

A variety of cancers, including those of the breast, arise near or within adipose tissue depots (23). Therefore, during tumor development in these organs a heterotypic cell-cell interface exists between adipocytes and cancer cells. We and others have demonstrated that triple-negative breast cancers (TNBC, estrogen/progesterone/HER2 receptor-negative) utilize and require fatty acid oxidation to fuel bioenergetic metabolism (24, 25). The origin of the fatty acids being oxidized remains largely unclear. Several studies have demonstrated that tumor cells can secrete cytokines such as tumor necrosis factor-□ that induce lipolysis in adjacent adipocytes, and that adipocyte-derived fatty acids can be taken up and oxidized by cancer cells (26–31). These studies, however, have mostly relied upon transwell co-culture methods that do not recapitulate the direct cell-cell contact observed in vivo (27–30). Furthermore, evidence of enhanced lipolysis in adipocytes adjacent to breast tumors has not been well established in clinical patient samples. Mammary adipocytes undergo enhanced lipolysis when in close proximity to non-tumor epithelial cells, suggesting that local pro-lipolytic mechanisms exist, but have yet to be identified (31, 32). Thus, we set out to study the breast cancer-adipocyte interface and determine the contribution of cell-cell contact to tumorigenesis.

To determine if lipolysis occurs in normal tissue adjacent to breast tumors (NAT), we employed four independent strategies. First, we employed three-component breast (3CB) composition measure, a radiographic imaging method derived from dual-energy mammography that allows water, lipid and protein content of a tissue to be quantified (1). We postulated that if tumors induce lipolysis in adipocytes, we would observe

differences in lipid content between NAT near the tumor compared to NAT further away. Using 3CB imaging, we assessed the lipid content of clinical breast tumors and the first 6 mm of NAT segmented into 2 mm “rings” from 46 patients with invasive breast cancer (Fig. 1A and Table S1). As we have previously demonstrated (5), we found a significant decrease in lipid content in lesions compared to NAT 0-2 mm away (R1) (Fig. 1B). This is congruent with breast tumors being epithelial in nature, while the major constituent of normal breast is adipose tissue (32). Remarkably, we also found that within NAT there was a significant stepwise decrease in lipid content comparing R3 (4-6 mm) to R2 (2-4 mm), and R2 to R1 (Fig. 1B). In addition, we asked whether changes in lipid content between R3 and R1 NAT correlate with receptor status or tumor grade (Table S1). We found that NAT surrounding triple-negative (TN) and grade 2/3 tumors trended towards a greater average change in lipid content than receptor-positive (RP) and grade 1 tumors, respectively (Fig. S1, A and B). These data suggest that adipocytes near breast tumors have partially depleted lipid stores, and that TN and higher-grade tumors may induce this phenomenon to a greater degree than RP and low-grade tumors.

Previous studies have demonstrated that adipocyte size is inversely correlated to lipolysis status in mammary tissue (33). We quantified average adipocyte size in R1 and R3 in 11 of the 46 patients for whom we had access to histological sections of treatment-naïve tumor and NAT at the time of surgical resection (Fig. 1A, Fig. S1C and Table S1). Similar to the change in lipid content observed, we found a significant decrease in adipocyte size in R1 compared to R3 in all patients analyzed, indicating that adipocytes are smaller when closer to breast tumors (Fig. 1C). Finally, we correlated the change in lipid content and adipocyte size on an individual patient basis. We found a

positive correlation (R = 0.5818, p = 0.0656) between the change in lipid content and adipocyte area (Fig. 1D). Taken together, these data suggest adipocytes are smaller and have diminished lipid content when adjacent to breast tumors, two phenotypes that are established indicators of increased lipolysis (33).

Second, we sought to determine if gene expression changes associated with lipolysis were observed in tumor-adjacent adipocytes. To first generate a lipolysis gene expression signature, we identified the 100 most upregulated genes when a differentiated adipocyte cell culture model is stimulated with cAMP, a critical pro-lipolytic signaling molecule (9). We then used a publically available dataset of gene expression data for primary breast tumors as well as matched NAT 1, 2, 3 and 4 cm away from the tumor. We sought to determine if enrichment of the lipolysis signature occurred in NAT compared to non-tumor breast tissue obtained from healthy individuals using single-set gene set enrichment analysis (10, 11). We found a significant elevation of the cAMP-dependent lipolysis signature in tumor and NAT from all regions analyzed compared to control tissue (Fig. 1E). These data indicate that lipolytic signaling is activated in breast-tumor adjacent adipocytes up to 4 cm away from the primary tumor. Adipose tissue is sparsely innervated and a recent study found that adipocytes can propagate pro-lipolytic sympathetic signals via direct transfer of cAMP through adipocyte-adipocyte gap junctions (34). Thus, tumor-adjacent adipocytes receiving a pro-lipolytic stimulus may disperse this signal to distant adipocytes via gap junctions, which might explain the elevation of cAMP signaling we observed up to 4 cm away from the tumor (Fig. 1E).

Third, we sought to determine if there are changes in protein abundance in tumor-adjacent NAT indicative of lipolysis activation. We conducted laser capture microdissection (LCM, 10,000 cells per capture) on primary breast tumors from 75 patients, representing all major PAM50 subtypes. For a subset of patients, we also collected matched stroma and/or NAT. As a control, we conducted LCM on non-tumor breast tissue from 42 healthy subjects (Table S2A). Global proteomic analysis was performed using liquid chromatography-tandem mass spectrometry (LC-MS/MS) (Table S2B). Notably, one of the most significantly upregulated proteins in NAT, and indeed one of the most NAT-specific proteins, compared to all other tissues examined was hepatocyte nuclear factor 4-α (HNF4α) (Fig. 1F). As HNF4α is an established, essential activator of lipolysis in adipose tissue (35), these data indicate lipolysis is highly activated in breast-tumor adjacent adipose tissue.

Fourth, we sought to validate the observations made in our clinical datasets using mouse models of breast cancer. Hormone sensitive lipase (HSL) is a critical lipolytic enzyme; its activation by protein kinase A (PKA) leads to phosphorylation at serine 563 (33), while prolonged activation results in down-regulation of total HSL expression through a negative feedback mechanism (21, 22). We performed immunoblot analysis to probe for HSL, phospho-HSL (S563) and HNF4α in tumor and NAT tissues from three well-characterized breast cancer patient-derived xenograft (PDX) models (HCI002, HCI009, HCI010) and a transgenic model of MYC-driven TNBC (MTBTOM) (14, 15), as well as corresponding control mammary tissues. In all models analyzed, total HSL was decreased in NAT compared to control tissues (Fig. 1, G and H). Downregulation of total HSL has been observed in obesity and in an independent

analysis of primary breast tumor NAT, and is thought to be the result of a negative feedback loop in adipocytes in response to chronic lipolysis (36, 37). Additionally, in 3 of the 4 models examined we found an increase in HNF4α or the phospho-HSL/HSL ratio (Fig. 1, G and H), both characteristic of increased lipolysis (33, 35). Taken together, our concurrent findings in 3 independent clinical datasets and several models of patient-derived and transgenic breast cancer in mice indicate that lipolysis is activated, albeit to varying degrees, in breast cancer-adjacent adipose tissue. These findings support the conclusion that “normal” tissue adjacent to tumors is in fact not normal (38); in the context of breast cancer, tumor-adjacent adipocytes have markers of activated lipolysis with corresponding diminished lipid stores.

We next sought to determine the contribution of cell-cell contact to lipolysis activation in breast tumor-adjacent adipocytes. Gap junctions are cell-cell junctions formed by a family of proteins called connexins, which are known to transport a variety of small molecules (<1 kD), including cAMP (34, 39). Connexins were long thought to play tumor-suppressive roles in cancer, but recent evidence from a variety of tumor types has challenged this notion (39–42). Given that adipocytes are capable of transferring cAMP and activating lipolysis in a homotypic interaction (34), we hypothesized that gap junctions may form between tumor cells and adipocytes in a heterotypic fashion and activate lipolysis via transfer of cAMP. Using a well-established dye transfer assay (41), we first assayed for functional gap junction formation between breast cancer cells. We tested whether the TNBC cell line HCC1143 or the more indolent RP cell line T47D could transfer gap-junction dependent dyes to the same tumor cell line. Both lines formed functional gap junctions, but dye transfer amongst

HCC1143 cells was 30-fold increased (Fig. 2A) compared to transfer amongst T47D cells. Thus, we reasoned there may be differences in sensitivity to gap junction inhibition between TN and RP cells. Furthermore, given the upregulation of the MYC oncogene in the majority of TNBC (43, 44), we asked whether MYC expression affects gap junction dependence. We examined if gap junction inhibition alters cell viability in a panel of TN and RP human breast cell lines with varying MYC levels (24). We assayed intracellular ATP levels as a proxy for cell number. Intriguingly, TNBC cell lines with high MYC expression (24), including HCC1143, was significantly more sensitive to 48 hours of treatment with the pan-gap junction inhibitor carbenoxolone (CBX) than the low MYC TNBC or RP cell lines tested (Fig. 2B). These data suggest that gap junction communication occurs between breast cancer cells, and that a threshold amount of gap junction activity may be especially important in TN breast cancer cells with high MYC.

To delineate the role of connexins in TN compared to RP breast cancer further, we examined the expression of the 21 connexin genes in 771 primary human TN (n = 123) and RP (n = 648) tumors using publically available RNAseq data from The Cancer Genome Atlas (TCGA). Of the 20 connexins for which data was available, 5/20 were significantly downregulated, 11/20 were significantly upregulated, and 4/20 were not significantly changed in TN versus RP tumors (Fig. 2C). We noted that 5 of 7 members of the GJB class of gap junction proteins were upregulated (Fig. 2C). As an independent approach to examine expression of connexins in TNBC, we performed RNAseq on MTBTOM tumors and non-tumor control tissue (Table S3). Of the 10 connexins for which data were available, 2/10 were significantly downregulated, 4/10 were significantly upregulated, and 4/10 were not significantly changed in MTBTOM tumors

versus control tissue (Fig. 2D). Connexin 31 (GJB3, Cx31) was the most significantly elevated connexin in both human TN tumors and the MYC-driven TNBC model. Thus, we focused the remainder of our studies on Cx31. In non-tumor tissues Cx31 expression has been identified in keratinocytes, the small intestine, and the colon (45, 46). Although roles for various connexins as oncogenes and/or tumor suppressors have been described (39, 40), the function of Cx31 in tumorigenesis has not been established.

Accordingly, we sought to determine if functional Cx31-containing gap junctions form between breast cancer cells and adipocytes. To model the direct cell-cell contact observed in vivo between breast cancer cells and adipocytes, we developed three independent co-culture approaches. First, we stably transduced HCC1143 (TNBC) and T47D (RP) cells with an mCherry expression plasmid. We then injected either mCherry-HCC1143 or -T47D cells directly into primary mammary adipose tissue isolated from a healthy individual (WD43177). After overnight co-culture we imaged the adipose tissue using confocal microscopy to identify regions of potential cell-cell contact. These regions were formalin-fixed and paraffin-embedded and probed for Cx31 and pan-cytokeratin expression, to distinguish epithelial tumor cells, using immunofluorescent microscopy. We found that HCC1143 cells formed close cell-cell contacts with primary adipocytes, and that both HCC1143 cells and adipocytes robustly expressed Cx31 at the plasma membrane (Fig. 3A). In contrast, T47D cells, despite forming cancer cell-cancer cell contacts, did not form close contacts with adipocytes (Fig. 3B). To further validate the presence of cancer-adipocyte gap junctions in TNBC, we examined Cx31 expression in primary patient biopsies. We found that both TN tumor cells and

adipocytes robustly express Cx31 at the plasma membrane, and that many points of direct cell-cell contact occur in vivo (Fig. 3C). These data suggest breast cancer cells are capable of forming close cell-cell contacts with adipocytes. Additionally, we note that our observations of such contacts correlated with the presence of Cx31 at both the tumor cell and adipocyte plasma membrane.

To determine whether breast cancer cells and adipocytes rely upon Cx31-dependent gap junctions, we utilized CRISPR/Cas9 technology to generate an allelic series of GJB3 knockout lines. Despite several attempts we were unable to generate any cancer cell lines with homozygous GJB3 deletion, strongly suggesting that a basal level of Cx31 expression is required for breast cancer cell growth. Therefore, we focused our studies on two TN lines, HS578T and HCC1143, that both have 3 copies of GJB3 to generate partial knockout lines. Specifically, we generated two independent clones of the HS578T line with 1 of 3 copies of GJB3 deleted (HS578T 1-GJB3+/+/- and 2-GJB3+/+/-), and from the HCC1143 line one clone with 1 of 3 copies deleted (HCC1143 GJB3+/+/-) and a second clone with 2 of 3 copies deleted (HCC1143 GJB3+/-/-) (Fig. 3D).

To determine if Cx31 expression impacted tumor cell-adipocyte communication we developed a co-culture model in which HCC1143 GJB3+/+/+, GJB3+/+/- or GJB3+/-/- cells were seeded in 2D culture and loaded with gap junction-transferable dye. We added primary mammary adipose tissue from three healthy individuals (WD42295, WD43911, WD50223) directly on top of the monolayers to ensure direct contact. Tumor cells and adipocytes were co-cultured for 5 hours and then assayed for gap junction-dependent dye transfer from the cancer cells to adipocytes. We found that robust dye

transfer occurred from the HCC1143 GJB3+/+/+ cells to mammary adipocytes of all three patients (Fig. 3E). However, reduction of Cx31 level by 1/3 or 2/3 in the GJB3+/+/- and GJB3+/-/- lines, respectively, resulted in a significant decrease in dye transfer compared to GJB3+/+/+ control cells (Fig. 3E). These data suggest functional gap junctions form between TN breast cancer cells and adipocytes in a Cx31-dependent manner.

Since adipocytes can activate lipolysis in neighboring adipocytes via gap junction-dependent transfer of cAMP (34), we suspected cAMP may be transferred via breast cancer cell-adipocyte gap junctions. To determine if breast cancer cell gap junctions are permeable to cAMP, we treated a panel of human TN and RP cell lines with CBX for 24 hours. In 5 of 6 lines tested we found marked increases in the levels of intracellular cAMP concentration in CBX-treated versus vehicle-treated cells (Fig. 3F). Additionally, significantly higher concentrations of cAMP were observed in high MYC TN cells in comparison to low MYC TN or RP cells (Fig. 3F). Given the recent observation that increased intracellular cAMP selectively decreases the viability of TN cells (47), our finding that high MYC TN cells display increased sensitivity to prolonged CBX treatment (Fig. 2B) may be due in part to increased levels of intracellular cAMP (Fig. 3F). Thus, the increase in intracellular cAMP upon pan-gap junction inhibition in 5 of 6 lines examined suggests that breast cancer cell gap junctions are indeed permeable to cAMP.

We next tested whether cAMP is directly transferred from breast cancer cells to adipocytes and if the abundance of Cx31 alters transfer. HCC1143 GJB3+/+/+, GJB3+/+/- or GJB3+/-/- cells were seeded and loaded with a fluorescent cAMP

analogue (fluo-cAMP). These monolayer cultures were then co-cultured in direct contact with primary mammary adipose tissue from three healthy individuals (WD47558, WD46812, WD50344), and incubated for 5 hours. Adipocytes were then isolated from the tumor cells and assayed for cAMP. We found that cAMP transfer occurred from control cells to adipocytes from all three patients (Fig. 3G). However, as we observed with transfer of gap junction-permeable dye (Fig. 3E), reduction of Cx31 expression resulted in a significant reduction of cAMP transfer (Fig. 3G). These results indicate that cAMP is transferred from TN breast cancer cells to adipocytes in a Cx31-dependent manner.

We next sought to determine if downstream cAMP signaling is activated in adipocytes in a tumor-adipocyte gap junction-dependent manner. To determine if cAMP signaling is activated in adipocytes upon cell-cell contact with breast cancer cells, we used a primary mouse preadipocyte model that can be differentiated to adipocytes in vitro (9). This model is ideal to study downstream signaling during co-culture because changes in adipocyte transcription can be assayed via qRT-PCR using murine-specific primers. Adipocytes were terminally differentiated and then HS578T and HCC1143 GJB3 partial knockout lines were seeded directly on top of adipocyte cultures. After co-culturing the cells for 24 hours we extracted RNA and assayed for changes in murine-specific (thus adipocyte-specific in this system) UCP1 expression, a known cAMP-responsive gene (9) to measure cAMP signaling. We also assayed for mouse aP2 expression as a marker of adipocyte differentiation. Our positive control, forskolin, which raises intracellular cAMP levels by activating adenylyl cyclase (9), robustly induced UCP1 expression compared to vehicle-treated cells (Fig. 3H). The HCC1143 GJB3+/+/+

and GJB3+/+/- lines both induced UCP1 expression, but UCP1 induction was significantly reduced with the GJB3+/-/- cells (Fig. 3H). In contrast, none of the HS578T lines, including the GJB3+/+/+ control, were capable of inducing UCP1 expression (Fig. 3H). All conditions, including forskolin treatment, resulted in reduced aP2 expression (Fig. 3H), suggesting effects on adipocyte differentiation are distinct from those observed on cAMP signaling. Given that Cx31 expression is similar in HS578T GJB3+/+/+ and HCC1143 GJB3+/-/- cells (Fig. 3D), and that neither activate cAMP signaling (Fig. 3H), it is possible that a Cx31 expression threshold is required for breast cancer cells to activate cAMP signaling in adjacent adipocytes. Although direct transfer of cAMP has been described between adipocytes in a homotypic interaction (34), here we identify for the first time a gap junction-dependent activation of lipolysis in adipocytes by tumor cells.

Finally, we sought to determine the contribution of breast cancer Cx31-dependent gap junctions to tumorigenesis. We found that HS578T 1-GJB3+/+/- and 2-GJB3+/+/-, and HCC1143 GJB3+/+/- lines did not display a difference in proliferation compared to their respective GJB3+/+/+ control lines. In contrast, HCC1143 GJB3+/-/- cells demonstrate a significant reduction in cell proliferation (Fig. 4A), but no reduction in cell viability (data not shown). These data suggest that, even in the absence of breast cancer cell-adipocyte interaction, Cx31 may promote breast cancer cell proliferation. To determine the contribution of Cx31 to breast tumorigenesis in vivo, we transplanted each of the HS578T and HCC1143 Cx31 partial knockout lines into cleared mammary fat pads of immunocompromised NOD-SCID/gamma (NSG) female mice and determined the time of tumor onset and time to reach ethical endpoint (when tumor

reaches 2cm in any dimension). Remarkably, with the HS578T lines, in which partial GJB3 knockout had no effect on cell proliferation in vitro (Fig. 4A), 0/10 mice that received HS578T 1-GJB3+/+/- or 2-GJB3+/+/- xenografts (5 per line) developed tumors within 180 days (Fig. 4B). Among the HCC1143 lines, the GJB3+/+/- line displayed a significant delay in both tumor onset and time to ethical endpoint, while only 3 of 5 mice transplanted with the GJB3+/-/- line developed tumors, and none reached ethical endpoint within 180 days (Fig. 4B). Our data indicates that Cx31 promotes breast tumorigenesis in vivo.

We sought to clarify the effects of Cx31 expression on lipolysis versus other effects on tumor growth. To determine if control and Cx31 partial knockout tumors differentially induced lipolysis, we collected tumor and NAT from HCC1143 GJB3+/+/+, GJB3+/+/- and GJB3+/-/- tumor-bearing mice, as well as residual mammary glands from the two GJB3+/-/- mice that were transplanted, but never developed tumors. Using immunoblot analysis, we probed for markers of lipolysis. Notably, a marked reduction in total HSL expression was found in 3 of 3 HCC1143 GJB3+/+/+ NAT samples compared to control tissues, consistent with persistent activation of lipolysis (Fig. 4C). In contrast, we did not observe a consistent change in HSL expression in any of the other NAT samples analyzed from tumors with partial Cx31 knockout (Fig. 4C). Interestingly, we found a marked increase in phospho-HSL/HSL ratio in both the HCC1143 GJB3+/+/+ and GJB3+/+/- NAT samples, but this difference was significantly reduced in HCC1143 GJB3+/-/- NAT (Fig. 4C). The increase in phospho-HSL/HSL in GJB3+/+/- NAT may be due to alternative modes of lipolysis activation, such as secreted pro-lipolytic cytokines (26), which is congruent with the observed increase in UCP1 expression during

GJB3+/+/--adipocyte co-culture (Fig. 3H). To further interrogate lipolytic signaling in NAT, we probed for cAMP abundance in HCC1143 GJB3+/+/+ and GJB3+/+/- tumors by mass spectrometry. We found a significant increase in intratumoral cAMP level in HCC1143 GJB3+/+/- tumors compared to the GJB3+/+/+ control tumors (Fig. 4D), consistent with diminished transfer of cAMP to NAT. We examined GJB3+/+/+ and GJB3+/+/- tumors and associated NAT, and assayed for differences in adjacent adipocyte size, as an indicator of lipolysis. Strikingly, we found a significant increase in the average size of adipocytes adjacent to GJB3+/+/- tumors compared to GJB3+/+/+ control tumors (Fig. 4E), again supporting a decreased induction of lipolysis in NAT from Cx31 partial knockout tumors. Finally, if the delay in HCC1143 GJB3+/+/- tumor onset (Fig. 4B) was due to an inability to activate lipolysis in adjacent adipocytes, we reasoned that pharmacological activation of lipolysis should rescue this phenotype. Indeed, we found that daily intra-peritoneal injection of CL316273, a specific □3-receptor agonist known to activate lipolysis in vivo (48), completely rescued the delay in tumor onset observed in HCC1143 GJB3+/+/- tumors, but did not further promote the growth of HCC1143 GJB3+/+/+ tumors (Fig. 4F). Taken together, these data indicate that cAMP signaling and lipolysis are activated in breast tumor-adjacent adipocytes in a Cx31-dependent manner in vivo.

In summary, we find that lipolysis is activated in breast cancer-adjacent adipose tissue and that functional gap junctions form between breast cancer cells, and between breast cancer cells and adipocytes. In addition, cAMP is transferred via breast cancer cell gap junctions, and cAMP signaling is activated in adipocytes adjacent to breast cancer cells in a gap junction-dependent manner. Finally, we discovered a previously

unappreciated role for Cx31-dependent gap junctions in breast tumor growth and activation of lipolysis in tumor-adjacent adipose tissue in vivo. Cx31 may represent a new therapeutic target to treat pro-lipolytic breast tumors. Furthermore, the recent discovery of gap junction formation between brain metastatic carcinoma cells and astrocytes (41) suggests that gap junction-dependent heterotypic interaction between tumor and non-tumor cells may be an emerging hallmark of tumorigenesis.

Experimental procedures

3CB imaging protocol. The 3CB method combines dual-energy X-ray mammography attenuations and a breast thickness map to solve for the three unknowns: water, lipid, and protein content (1). We used Hologic Selenia full-field digital mammography system (Hologic, Inc.) to image women with 3CB. Two dual energy mammograms were acquired on each woman's affected breast using a single compression. The first exposure was made under conditions of regular clinical screening mammogram. The second mammogram was acquired at a fixed voltage (39 kVp) and mAs for all participants. A high energy exposure (39 kVp/Rh filter) was made using an additional 3-mm plate of aluminum in the beam to increase the average energy of the high energy image. We limited the total dose of this procedure to be approximately 110% of the mean-glandular dose of an average screening mammogram. The images were collected under an investigational review board approval to measure breast composition. The breast thickness map was modeled using the SXA phantom (2). The thickness validation procedure concluded in a weekly scanning of specially designed quality assurance phantom (3). The calibration standards and 3CB algorithms are described in full elsewhere (1, 4). The region of interests of lesions and three surrounding rings of 2 mm distance outward from lesion boundary were derived for water, lipid, and protein maps. The median lipid measures of regions of interest within lesions, three rings outside of lesions, differences and ratios between lesions and rings were generated for both CC and MLO mammograms. Average values of generated variables of two views were used.

3CB patient population. Five hundred women with suspicious mammography findings (BIRADS 4 or greater) were recruited and imaged before their biopsies using a 3-component decomposition dual-energy mammography protocol (3CB) for a multicenter study with two recruitment sites: The University of California at San Francisco and Moffitt Cancer Center, Tampa, Florida (5). All patients received a biopsy of the suspicious area, and breast biopsies were clinically reviewed by the pathologists. A subset of pathology proven triple-negative (n = 6) and receptor-positive (n = 40) invasive cancers were selected for this study. All women received both cranio-caudal (CC) and mediolateral-oblique (MLO) views. Exclusion criteria for the study were no prior cancer, biopsies, or breast ipsilateral alterations, and no occult findings. This study was approved by the institutional review board of the respective institutions.

Histological sectioning, hematoxylin and eosin staining, and adipocyte area quantification. Invasive breast carcinomas were obtained from the Pathology Departments of the University of California San Francisco (San Francisco, CA) and Moffitt Cancer Center (Tampa, FL). The study population included 39 hormone receptor positive tumors (32 ER positive (+)/PR+/HER2 negative, 2 ER+/PR-/HER2-, 4 ER+/PR+/HER2+, and 1 ER+/PR-/HER2+), 6 triple negative (ER-/PR-/HER2-) tumors, and 1 ER-/PR-/HER2+ tumor. Thirty-nine tumors were invasive ductal carcinomas and 7 were invasive lobular carcinomas. Tissue was fixed in 10% formalin and embedded in paraffin, and 4 micron sections were cut for hematoxylin and eosin (H&E) and immunohistochemical ER, PR, and HER2 staining, as well as HER2 fluorescence in situ hybridization (FISH) for a subset of tumors. ER, PR, and HER2 were scored according

to ASCO/CAP guidelines (6, 7). An H&E-stained slide demonstrating tumor and sufficient (at least 0.5 cm) NAT was chosen from each of 11 tumors with available slides and subjected to whole slide scanning at 400× magnification using an Aperio XT scanner (Leica Biopsystems, Buffalo Grove, IL). Images were visualized using ImageScope software (Leica Biosystems). For each tumor, 4 representative images at 50X magnification (at least 50 adipocytes per image) from R1 and R3 were analyzed using Fiji imaging software with the open source Adiposoft v1.13 plugin (8).

cAMP-dependent lipolysis signature. The cAMP-dependent lipolysis gene signature was generated using RNA-seq data of cAMP-treated adipocytes (9). Differentially expressed genes were sorted according to their P value and the top 100 upregulated genes were chosen for the signature. This signature was then used to calculated enrichment scores using the single-set gene set enrichment analysis (ssGSEA) method (10). “cAMP 100 signature” enrichment scores were calculated for a dataset containing multiple samples from multiple regions surrounding breast tumors (11). The dataset includes samples from the tumor itself (n = 9), and NAT 1 cm (n = 7), 2 cm (n = 5), 3 cm (n = 3) and 4 cm (n = 4) away from the tumor, in addition to healthy normal samples (n = 10). The spatial data set of multiple regions surrounding breast tumors was download from EMBL-EBI ArrayExpress (Accession E-TABM-276). Raw CEL files were downloaded and processed using custom Affymetrix GeneChip Human Genome U133 Plus 2.0 CDF obtained from BrainArray (12). The processing and normalization were performed using the Robust Multi-array Average (RMA) procedure on Affymetrix microarray data.

Laser Capture Microdissection. Breast tumor tissue was sectioned at 6 μm in a Leica CM 1850 Cryostat (Leica Microsystems GmbH). The sections were mounted on uncharged glass slides without the use of embedding media and placed immediately in 70% ethanol for 30 seconds. Subsequent dehydration was achieved using graded alcohols and xylene treatments as follows: 95 % ethanol for 1 minute, 100% ethanol for 1 minute (times 2), xylene for 2 minutes and second xylene 3 minutes. Slides were then dried in a laminar flow hood for 5 minutes prior to microdissection. Then, sections were laser captured microdissected with PixCell II LCM system (Arcturus Engineering). Approximately 5000 shots using the 30 micron infra¬red laser beam will be utilized to obtain approximately 10,000 cells per dissection. All samples were microdissected in duplicate on sequential sections.

SDS-PAGE and In-gel Digestion. All membranes containing the microdissected cells from breast tumor tissue were removed and placed directly into a 1.5 mL Eppendorf tube. Membranes containing the microdissected cells were suspended in 20 □L of SDS sample buffer, reduced with DTT and heated in a 70-80C water bath for approximately 10 min. The supernatant was then electrophoresed approximately 2 cm into a 10% Bis Tris gel, stained with Colloidal Blue with destaining with water, and the region was excised and subjected to in-gel trypsin digestion using a standard protocol. Briefly, the gel regions were excised and washed with 100 mM ammonium bicarbonate for 15 minutes. The liquid was discarded and replaced with fresh 100 mM ammonium bicarbonate and the proteins reduced with 5 mM DTT for 20 minutes at 55° C. After

cooling to room temperature, iodoacetamide was added to 10 mM final concentration and placed in the dark for 20 minutes at room temperature. The solution was discarded and the gel pieces washed with 50% acetonitrile/50 mM ammonium bicarbonate for 20 minutes, followed by dehydration with 100 % acetonitrile. The liquid was removed and the gel pieces were completely dried, re-swelled with 0.5 □g of modified trypsin (Promega) in 100 mM NH4HCO3, and digested overnight at 37°C. Peptides were extracted by three changes of 60% acetonitrile/0.1% TFA, and all extracts were combined and dried in vacuo. Samples were reconstituted in 35 □L 0.1 % formic acid for LC-MS/MS analysis.

LC-MS/MS Analysis, Protein Identification and Quantitation. Peptide digests were analyzed on a Thermo LTQ Orbitrap Velos ion trap mass spectrometer equipped with an Eksigent NanoLC 2D pump and AS-1 autosampler as described previously (13). Peptide sequence identification from MS/MS spectra employed the RefSeq Human protein sequence database, release version 54, and both database and peptide library search strategies (13). For initial protein assembly, peptide identification stringency was set at a maximum of 1% reversed peptide matches, i.e., 2% peptide-to-spectrum matches (PSM) FDR and a minimum of 2 unique peptides to identify a given protein within the full data set. To minimize false-positive protein identifications, only proteins with a minimum of 6 matched spectra were considered. The full dataset contained 850,847 filtered spectra corresponding to 31,594 distinct spectrum-peptide sequence matches, which mapped to 24,946 distinct peptide sequences and 2,230 indistinguishable protein identifications. The protein-level FDR for the final assembly

was 5.14%. Spectral counts for each protein in the final assembly were calculated as the sum of peptide-spectrum matches that met the criteria described above.

Orthotopic xenograft studies. The human samples used to generate patient-derived xenograft (PDX) tumors, as well as the human non-tumor samples, were previously described (14). The generation of the MTBTOM tumor model has been previously described (15). 4-week-old WT FVB/N and immunocompromised NOD/SCID-gamma (NSG) female mice were purchased from Taconic Biosciences. Viably frozen MTBTOM, HCI002, HCI009 and HCI010 tumor samples were transplanted into the cleared mammary fat pads of FVB/N and NSG mice, respectively. Tumor growth was monitored daily by caliper measurement in two dimensions. When tumors reached 1 cm (MTBTOM) or 2 cm (PDX) in any dimension mice were euthanized, tumor and NAT were isolated, and flash-frozen in liquid nitrogen. The protocols described in this and other sections regarding animal studies were approved by the UCSF Institutional Animal Care and Use Committee. For the HCC1143 and HS578T control and Cx31 partial knockout orthotopic xenografts, 5 x 10^5 cells were resuspended 1:1 with matrigel (Corning) and injected into the cleared mammary fat pads of 4-week-old WT NSG female mice. Tumor incidence and growth were monitored daily via palpation and caliper measurement, respectively. Mice were euthanized after 180 days or after tumors reached 2cm in any dimension. For HCC1143 GJB3+/+/+ and GJB3+/+/- xenografts, a central slice of tumor and surrounding NAT from separate was fixed in 4% paraformaldehyde and embedded in paraffin for histological sectioning, H&E staining and adipocyte area quantification, while the remaining tumor and NAT tissues were

flash-frozen in liquid nitrogen. For other xenografts, NAT was isolated and flash-frozen in liquid nitrogen. For the CL316273 experiment, mice were randomized into experimental groups immediately post-orthotopic transplant. The following day, drug treatment was initiated and mice received vehicle or 1 mg/kg CL316273, delivered by intraperitoneal injection, daily until tumor incidence was recorded via palpation.

Immunoblot analysis. Proteins were extracted using RIPA buffer (Thermo) and proteinase (Roche) plus phosphatase (Roche) inhibitor cocktails. Protein extracts were resolved using 4–12% SDS-PAGE gels (Life Technologies) and transferred to nitrocellulose membranes (Life Technologies). Membranes were probed with primary antibodies overnight on a 4 °C shaker, then incubated with horseradish peroxidase (HRP)-conjugated secondary antibodies, and signals were visualized with ECL (Bio-Rad). The primary antibodies targeting the following proteins were used: β-actin (actin) (sc-47778 HRP, Santa Cruz, 1:10,000), pHSL S563 (4139, Cell Signaling, 1:1000), HSL (4107, Cell Signaling, 1:1000), HNF4α (ab41898, Abcam, 1:1000), and Cx31 (ab156582, Abcam, 1:1000). Chemiluminescent signals were acquired with the Bio-Rad ChemiDoc XRS+ System equipped with a supersensitive CCD camera. Where indicated, unsaturated band intensities were quantified using Bio-Rad Image Lab software.

Cell culture and virus production. A panel of established TN and RP human breast cancer cell lines, and their culture conditions, have previously been described (16). No cell line used in this paper is listed in the database of commonly misidentified cell lines

that is maintained by the International Cell Line Authentication Committee (ICLAC) (http://iclac.org/databases/cross-contaminations/). All lines were found to be negative for mycoplasma contamination. Lentiviruses for Cas9 and sgRNAs were produced in 293T cells using standard polyethylenimine (Polysciences Inc.) transfection protocols.

Dye transfer and FACS analysis. For cancer cell-cancer cell transfer, monolayers of indicated lines (donors) were labelled with 1 μM CalceinAM dye (Life Technologies) at 37°C for 40 min. Dye-loaded cells were washed three times with PBS, and then single-cell suspensions of 1.5 X 105 mCherry-labelled cells (recipients) were added for 5 hours. Dye transfer was quantified by BD LSRFORTESSA or BD LSR II (BD Biosciences). For cancer cell-adipocyte transfer, monolayers of indicated control or Cx31 partial knockout lines (donors) were labelled with 1 μM CalceinAM dye at 37°C for 40 min. Dye-loaded cells were washed three times with PBS, and then primary mammary adipose tissues (recipient) were added for 5 hours. Primary adipose tissue was isolated from co-culture, washed with PBS, and dye transfer was quantified by measurement of total adipose fluorescence using a Tecan fluorescent plate reader.

Gene expression analysis. TCGA breast-invasive carcinoma data set was sourced from data generated by TCGA Research Network (cancergenome.nih.gov), made available on the University of California, Santa Cruz (UCSC) Cancer Browser. For the MTBTOM data set 11 endpoint MTBTOM orthotopic xenografts generated as described above and 3 mammary glands from naïve mice were flash-frozen in liquid nitrogen. RNA was isolated using the RNAeasy kit (Qiagen). Library preparation and Illumina

RNAseq was performed by Q2Solutions (www.q2labsolutions.com). All gene expression analyses were performed using the 'limma' R package (17).

ATP quantification. To determine the effects of CBX treatment on ATP levels, tumor cells were seeded in 96-well plates at 5,000–7,000 cells per well and cultured in the presence of 0 or 150 μM CBX (Sigma) for 48 hours, with triplicate samples for each condition. Relative ATP concentrations were determined using the CellTiter-Glo Luminescent Cell Viability Assay (Promega).

Isolation of primary mammary adipose tissue. Anonymous reduction mammoplasty samples were acquired from the Cooperative Human Tissue Network (CHTN). Samples were washed in DPBS supplemented with 1 % Penicillin/Streptomycin and 0.1 % Gentamicin (all GIBCO). Mammary adipose tissue was separated mechanically from epithelial tissue using a razor blade and was then cryopreserved in freezing medium (10% DMSO (Sigma) in FBS (X&Y Cell Culture)).

Immunofluorescence staining and microscopy. For adipose tissue-cancer cell co-culture, 1 X 10^6 of the indicated mCherry-labelled cell line was injected into primary mammary adipose tissue and cultured at 37°C for 18 hours. The co-cultures were examined using fluorescent microscopy to identify regions of adipose tissue containing mCherry-positive cancer cells. These regions were isolated and fixed in 4% paraformaldehyde and embedded in paraffin. Primary TNBCs used for immunofluorescence were identified and retrieved from the clinical archives of the

University of California San Francisco (UCSF) Department of Pathology. All tumors consisted of estrogen receptor (ER)-, progesterone receptor (PR)-, and HER2-negative invasive ductal carcinomas. Breast tissue was fixed in 10% formalin and embedded in paraffin. Tumor blocks with sufficient tumor and adjacent (at least 0.5 cm) normal tissue were selected, and 4μm sections were cut on plus-charged slides for immunofluorescence. This study was approved by the UCSF institutional review board. For immunofluorescence labeling, slides were dewaxed in xylene followed by rehydration in graded ethanol (100, 95, 70%) and deionized H2O. Antigen retrieval was performed in 10mM Tris, 1mM EDTA, 0.05% Tween 20, pH 9 at 121 °C for 4 min. Subsequently, tissue sections were blocked in 1% bovine serum albumin, 2% fetal bovine serum in PBS for 5 min, and incubated with primary antibodies (Cx31, 12880, Proteintech, 1:50 and pan-cytokeratin, sc-81714, Santa Cruz, 1:50) overnight at 4 °C. Following several PBS washes, sections were incubated with Alexa Fluor-488 or -568 conjugated antibodies, counterstained with DAPI (Sigma), and mounted using Vectashield (Vector). Epifluorescence images were acquired either by spinning disk microscopy on a customized microscope setup as previously described (18–20) except that the system was upgraded with a next generation scientific CCD camera (cMyo, 293 Photometrics) with 4.5 μm pixels allowing optimal spatial sampling using a Å~60 NA 1.49 objective (CFI 294 APO TIRF; Nikon), or at the UCSF Nikon Imaging Center using a Nikon Ti Microscope equipped with an Andor Zyla 5.5 megapixel sCMOS camera and Lumencor Spectra-X 6-channel LED illuminator. Images were collected using a Plan Apo λ 20x / 0.75 lens.

Generation of Cx31 partial knockout lines. LentiCas9-Blast (Addgene plasmid #52962) and lentiGuide-Puro (Addgene plasmid #52963) were gifts from Feng Zhang. sgRNAs against Cx31 were constructed using the Feng Zhang Lab CRISPR Design Tool (crispr.mit.edu). sgRNAs used were as follows:

Cx31 exon 1 sg1: CCAGATGCGCCCGAACGCTGTGG (HS578T 1-GJB3+/+/- and HCC1143 GJB3+/+/-)

Cx31 exon 1 sg2: CCGGGTGCTGGTATACGTGGTGG (HS578T 2-GJB3+/+/- and HCC1143 GJB3+/-/-)

Lentiviral transduction was performed in DMEM supplemented with 10% FBS and polybrene 10 μg/mL. Cas9-expressing cells were enriched by Blasticidin (10-15 μg/mL Gemini BioProducts) selection for seven days. Cas9+ cells were subsequently transduced with lentiGuide-Puro (with sgRNAs targeting Cx31) followed by puromycin (1 μg/mL; Gibco) for seven days. Thereafter, clonal selection was performed and clones screened for loss of target gene protein expression by immunoblot analysis.

cAMP quantification. For in vitro studies, tumor cells were seeded in 96-well plates at 5,000–7,000 cells per well and cultured in the presence of 0 or 150 μM CBX (Sigma) for 24 hours, with triplicate samples for each condition. Changes in cAMP concentration were determined using the cAMP-Glo Assay (Promega). For in vivo studies, frozen tissue was homogenized using a TissueLyser in 300 μl of 40:40:20 acetonitrile:methanol:water with the addition of 1 nM (final concentration) of D3-[15N]serine as an internal extraction standard (Cambridge Isotopes Laboratories Inc, DNLM-6863). 10 μl of cleared supernatant (via centrifugation at 15,000 r.p.m., 10 min,

at 4 °C) was used for SRM–LC-MS/MS using a normal-phase Luna NH2 column (Phenomenex). Mobile phases were buffer A (composed of 100% acetonitrile) and buffer B (composed of 95:5 water:acetonitrile). Solvent modifiers were 0.2% ammonium hydroxide with 50 mM ammonium acetate for negative ionization mode. cAMP levels were analyzed using the MassHunter software package (Agilent Technologies) by quantifying the transition from parent precursor mass to product ions.

cAMP transfer. For cancer cell-adipocyte transfer, monolayers of indicated control or Cx31partial knockout lines (donors) were labelled with 2□M fluo-cAMP (Biolog Life Science Institute) at 37°C for 30 min. cAMP-loaded cells were washed three times with PBS, and then primary mammary adipose tissues (recipient) were added for 5 hours. Primary adipose tissue was isolated from co-culture, washed with PBS, and cAMP transfer was quantified by measurement of total adipose fluorescence using a Tecan fluorescent plate reader.

Preadipocyte differentiation and qRT-PCR. Primary mouse preadipocytes were differentiated as previously described (21). Monolayers of differentiated adipocytes were washed with PBS, and then treated with vehicle or 10μM forskolin (Sigma), or seeded with 1 X 105 of the indicated cancer lines. Total RNA was isolated from co-cultures after 20 hours using the RNeasy kit (Qiagen). One μg of total RNA was reverse transcribed using iScript cDNA synthesis kit (Bio-Rad). The relative expression of UCP1, aP2, and GAPDH was analyzed using a SYBR Green Real-Time PCR kit (Thermo) with an Applied Biosystems QuantStudio 6 Flex Real-Time PCR System thermocycler

(Thermo). Variation was determined using the ΔΔCT method (22) with GAPDH mRNA levels as an internal control. Mouse-specific primers used were as follows:

GAPDH forward CCAGCTACTCGCGGCTTTA

reverse GTTCACACCGACCTTCACCA

UCP1 forward CACCTTCCCGCTGGACACT

reverse CCCTAGGACACCTTTATACCTAATGG

aP2 forward ACACCGAGATTTCCTTCAAACTG

reverse CCATCTAGGGTTATGATGCTCTTCA

Proliferation assays. To determine the effects of Cx31 partial knockout on cell proliferation, the indicated cell lines were seeded in 6-well plates at 1.5 X 105 cells/well. Cells were harvested at 24, 48 and 72 h. Cell counts were determined using the Countess Automated Cell Counter (Life Technologies) according to the manufacturer's instructions.

Statistical analysis. Prism software was used to generate and analyze Spearman correlation (Fig. 1D) and the survival plots (Fig. 4B). Correlation P values were generated using a two-sided t-test. Survival plot P values was generated using a log-rank test. All differential expression analyses (Fig. 2, C and D) were done using the 'limma' R package (17).

Code availability. Publicly available data sets were acquired as noted. Our annotations of the TCGA data set is available at (https://bitbucket.org/jeevb/brca).

Acknowledgements

This work was supported, in part, by the US Department of Defense–Congressionally Directed Medical Research Programs' Era of Hope Scholar award W81XWH-12-1-0272 (A.G.), the US National Institutes of Health (NIH) grants R01 CA170447 (A.G.), R01 CA166945 (J.A.S.), and R01 CA056721 (Z.W.), the Atwater Foundation (A.G.), the California Breast Cancer Research Program grant CBCRP 18IB-0042 (J.A.S.), the Breast Cancer Research Fund (H.R.), the EMBO postdoctoral fellowship ALTF 159-2017 (J.W.) and the US NIH F99/K00 Predoctoral to Postdoctoral Transition Award F99CA212488 (R.C.). The authors thank A. Welm for guidance in the use of patient-derived xenografts, A. Tward for technical guidance and helpful discussions, K.A. Fontaine for helpful discussions and comments on the manuscript, and S. Samson for a helpful consumer advocate perspective and guidance on our work. R.C. and A.G. conceived of research. R.C. designed and contributed to all in vitro studies and the in vivo mouse studies, contributed to all data analysis, and wrote the manuscript. J.W. designed and contributed to in vitro studies. S.M. analyzed 3CB data. L.J.Z. designed LCM and conducted proteomic analyses. S.M. conducted the LCM. D.A. conducted lipolysis signature enrichment analysis. A.B. contributed to immunofluorescent staining and microscopy, and generation of Cx31 partial knockout lines. D.V.d.M. contributed to the CL316273 mouse study. Y.C. conducted preadipocyte differentiation. C.B. and S.L. conducted mass spectrometry for cAMP. C.M. generated Cas9-expressing cancer cell lines. J.W. and E.W. isolated primary mammary adipose tissue. J.D.G. conducted FACS analysis. K.S. provided cAMP-dependent lipolysis signature. K.M.A. supervised FACS analysis. Z.W. supervised primary mammary adipose tissue isolation and provided

valuable discussion. D.K.N. supervised mass spectrometry for cAMP and provided valuable discussion. S.K. supervised preadipocyte and cAMP-dependent lipolysis studies and provided valuable discussion. A.J.B supervised enrichment analysis. M.E.S. and D.C.L. designed and supervised LCM and proteomics. H.R. provided valuable discussion. G.K. designed and conducted histological analyses and provided valuable discussion. J.A.S. supervised the 3CB study and data analysis and provided valuable discussion. A.G. supervised the study and provided valuable discussion and intellectual input. All authors edited the manuscript. All data and code related to these studies are available in the main text, supplementary materials and indicated repositories. The raw RNAseq data will be deposited on GEO. The authors declare no competing interest.

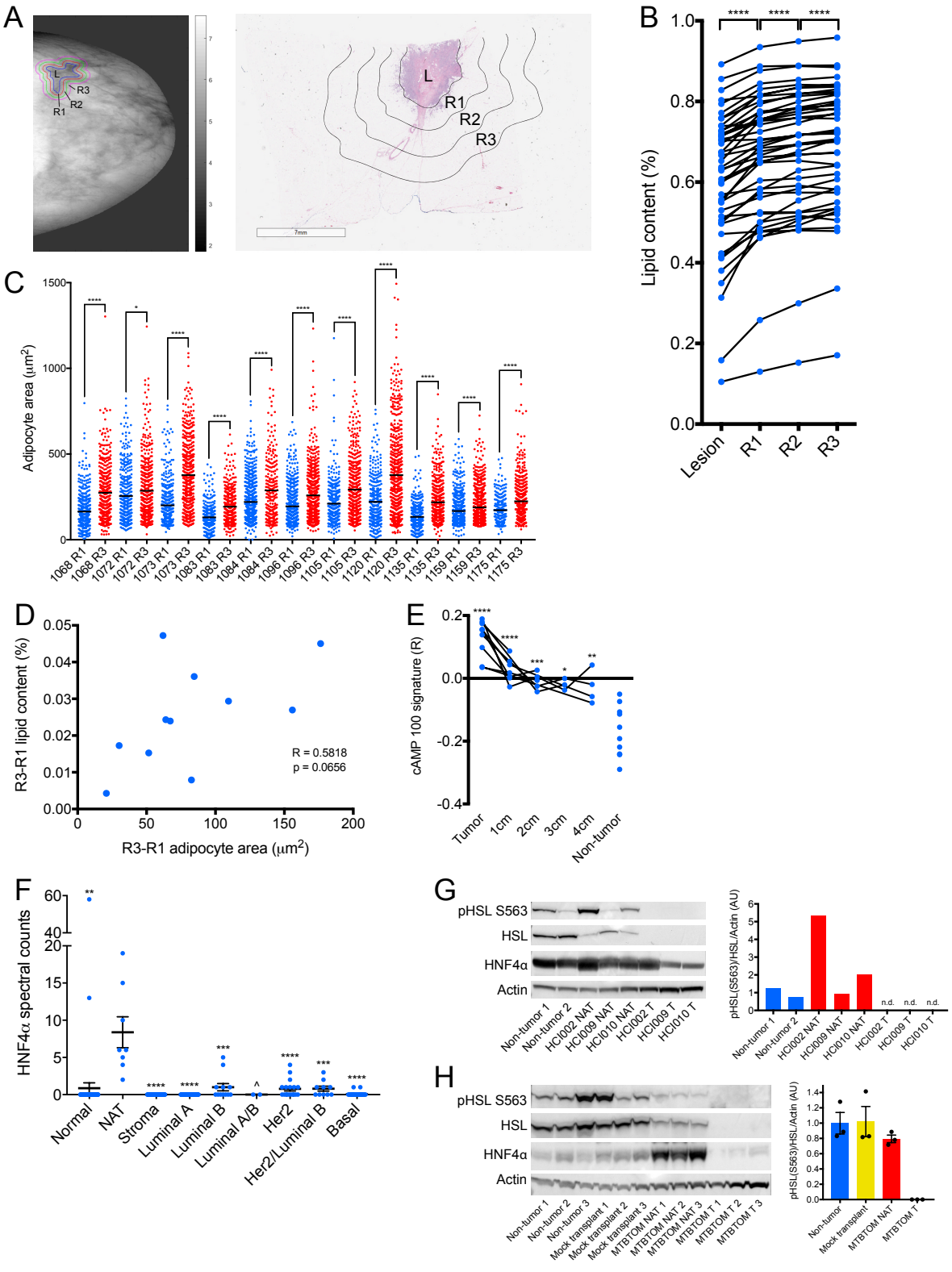

Fig. 1. Lipolysis and lipolytic signaling are activated in breast tumor-adjacent adipocytes from breast cancer patients and mouse models of breast cancer. (A) Representative

lipid content image (left) and hematoxylin and eosin stained excision specimen (right) from patients with invasive breast cancer. The lesion (L), and NAT 0-2 mm (R1), 2-4 mm (R2), and 4-6 mm (R3) away are indicated. (B) Percent lipid content (lipid content / lipid + water + protein content) of L, R1, R2 and R3 from patients (n = 46) with invasive breast cancer. (C) Adipocyte area in R1 and R3 from a subset of patients (n = 11) in B. The black line indicates mean adipocyte area, and each patient identifier is indicated. Each point represents individual adipocyte. (D) Correlation of change in lipid content in B and change in average adipocyte area in C from R3 to R1 for patients in C. Spearman correlation and two-tailed t test were used to generate the correlation coefficient and associated P value. (E) ssGSEA enrichment scores for cAMP-dependent lipolysis signature in primary breast tumors (n = 9), NAT 1 cm (n = 7), 2 cm (n = 5), 3 cm (n = 3), and 4 cm (n = 4), and healthy non-tumor breast tissue (n = 10). (F) HNF4α peptide counts from LC-MS/MS of primary tissue from healthy control breast tissue (n = 42), NAT (n = 4), stroma (n = 36), and luminal A (n = 38), luminal B (n = 6), luminal A/B (n = 1), HER2-amplified (n = 9), HER2-amplified/luminal B (n = 5), and basal (n = 16) tumors. Each point represents individual sample LCM on which LC-MS/MS was performed. LCM and LC-MS/MS was performed in technical duplicate on sequential histological slides from each patient. (G) Immunoblot analysis (left) showing expression levels of lipolysis activators HSL and HNF4α, and phosphorylated HSL (pHSL S563) in healthy non-tumor mammary gland and NAT and tumor tissues from a panel of PDXs. Quantification (right) of pHSL/HSL ratio, normalized to β-actin levels. (H) Immunoblot analysis (left) showing expression levels of lipolysis activators HSL and HNF4α, and phosphorylated HSL (pHSL S563) in healthy non-tumor mammary gland, mock-transplanted mammary gland, and NAT and tumor tissues from MTBTOM allografts. Quantification (right) of pHSL/HSL ratio, normalized to β-actin levels. For (B) and (E) black lines indicate matched samples from individual patients. For (F) and (H) mean $\pm$ s.e.m. is shown. ^P < 0.10, *P < 0.05, **P < 0.01, ***P < 0.001, ****P < 0.0001; paired two-tailed t test (B), unpaired two-tailed t test (C), (E), and (F).

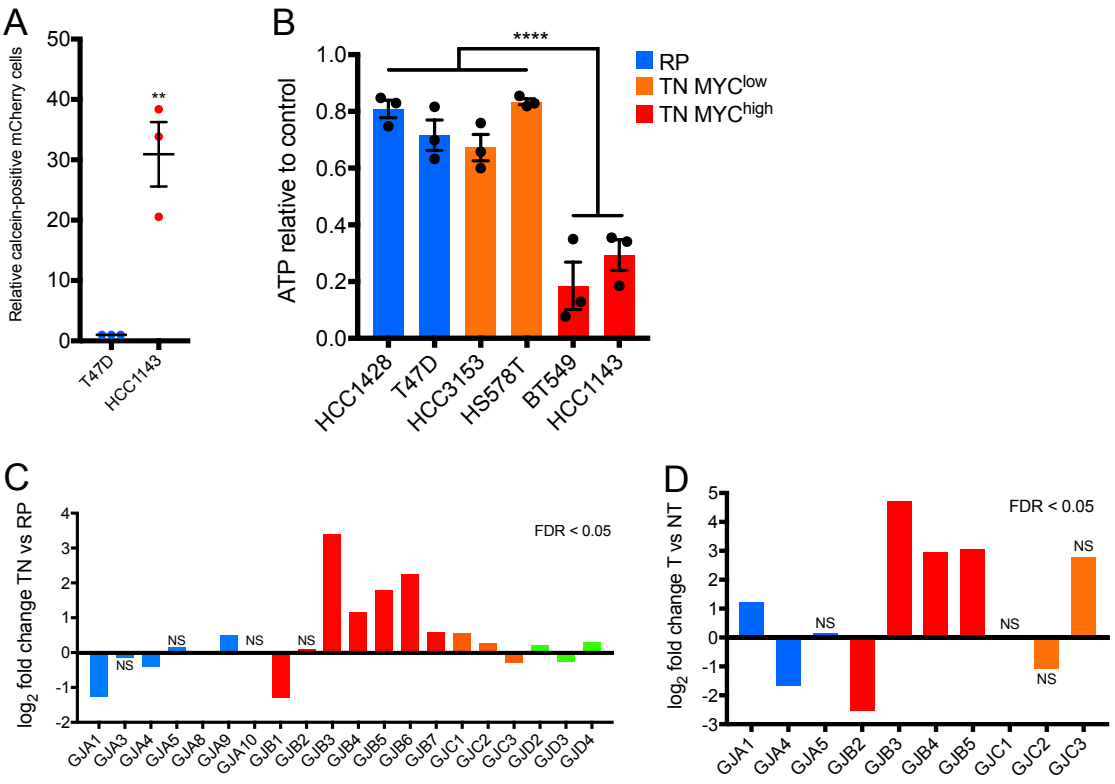

Fig. 2. Breast cancer cells form functional gap junctions and express Cx31. (A) Relative frequency of dye transfer from Calcein AM-loaded cells (donor) to mCherry-labelled cells (recipient) as determined by FACS (fluorescence-activated cell sorting) analysis. (B) ATP levels in TN high MYC, TN low MYC, and RP cell lines after treatment with 150 □M CBX for 48 hours relative to untreated (control) cells. (C) Fold change (log2) in expression of indicated connexin genes in TN (n = 123) versus RP (n = 648) tumors based on RNA-seq data acquired from TCGA of 771 breast cancer patients. (D) Fold change (log2) in expression of indicated connexin genes in T (n = 11) versus NT (n = 3) tissues based on RNA-seq data from MTBTOM allograft-bearing mice or healthy controls, respectively. For (A) and (B) mean ± s.e.m. of three independent biological replicates is shown. **P < 0.01, ****P < 0.0001; unpaired two-tailed t test (A) and (B). For (C) and (D) all differential expression analysis was done using the 'limma' R package.

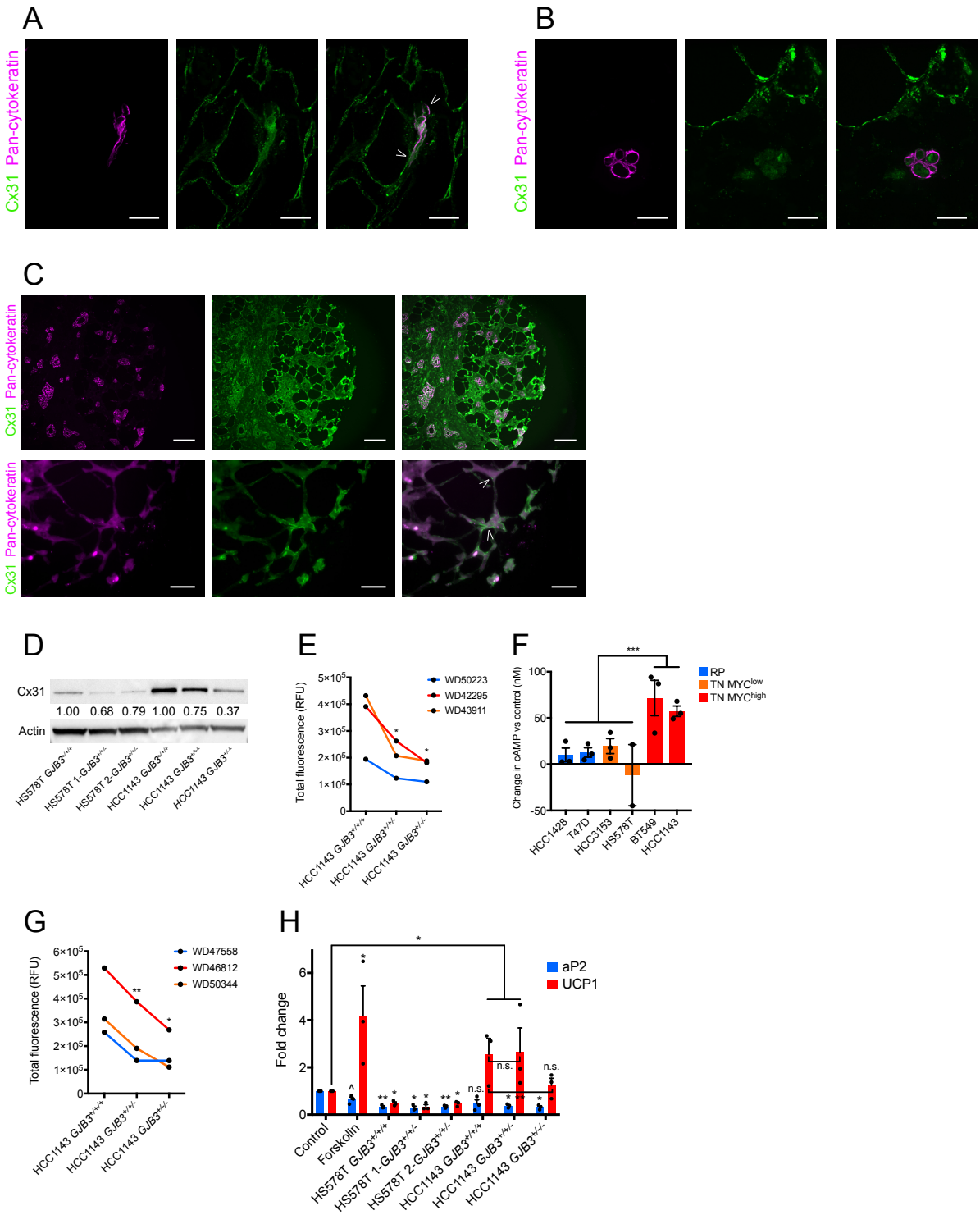

Fig. 3. Breast cancer cell-adipocyte gap junctions form, transfer cAMP, and activate lipolytic signaling in a Cx31-dependent manner. (A) Staining with Cx31 (green) and pan-cytokeratin (magenta) of primary mammary tissue from a healthy individual (WD43177) injected with TN mCherry-HCC1143 cells and co-cultured overnight. White arrowheads

indicate co-staining of Cx31 with contact point HCC1143 and adipocyte plasma membranes. Scale bar, 25 μm. (B) Staining with Cx31 (green) and pan-cytokeratin (magenta) of primary mammary adipose tissue from a healthy individual (WD43177) injected with RP mCherry-T47D cells and co-cultured overnight. Scale bar, 25 μm. (C) Staining with Cx31 (green) and pan-cytokeratin (magenta) of primary TNBC patient biopsies. Scale bar, top 100 μm, bottom 25 μm. (D) Immunoblot analysis showing expression levels of Cx31 in a panel of clonally derived control (GJB3+/+/+) and Cx31 partial knockdown TN lines. For the Cx31-knockdown lines each clone is referred to by number of GJB3 alleles expressed (e.g. GJB3+/+/- is missing 1/3 functional alleles). Quantification of Cx31 level normalized to β-actin level is indicated. (E) Dye transfer from indicated HCC1143 control and Cx31 partial knockout lines to primary mammary adipose tissue of indicated healthy individuals. (F) cAMP levels in TN high MYC, TN low MYC, and RP cell lines after treatment with 150 μM CBX for 24 hours relative to untreated (control) cells. (G) cAMP transfer from indicated HCC1143 control and Cx31-knockdown lines to primary mammary adipose tissue of indicated healthy individuals. (H) Fold change in UCP1 and aP2 expression in differentiated adipocytes after treatment with vehicle (control) or 10 μM forskolin, or co-cultured with indicated Cx31 partial knockout lines for 24 hours. For (F) and (H) mean ± s.e.m. of three independent biological replicates is shown. ^P < 0.10, *P < 0.05, **P < 0.01, ***P < 0.001; paired two-tailed t test (E), (G), and (H), unpaired two-tailed t test (F).

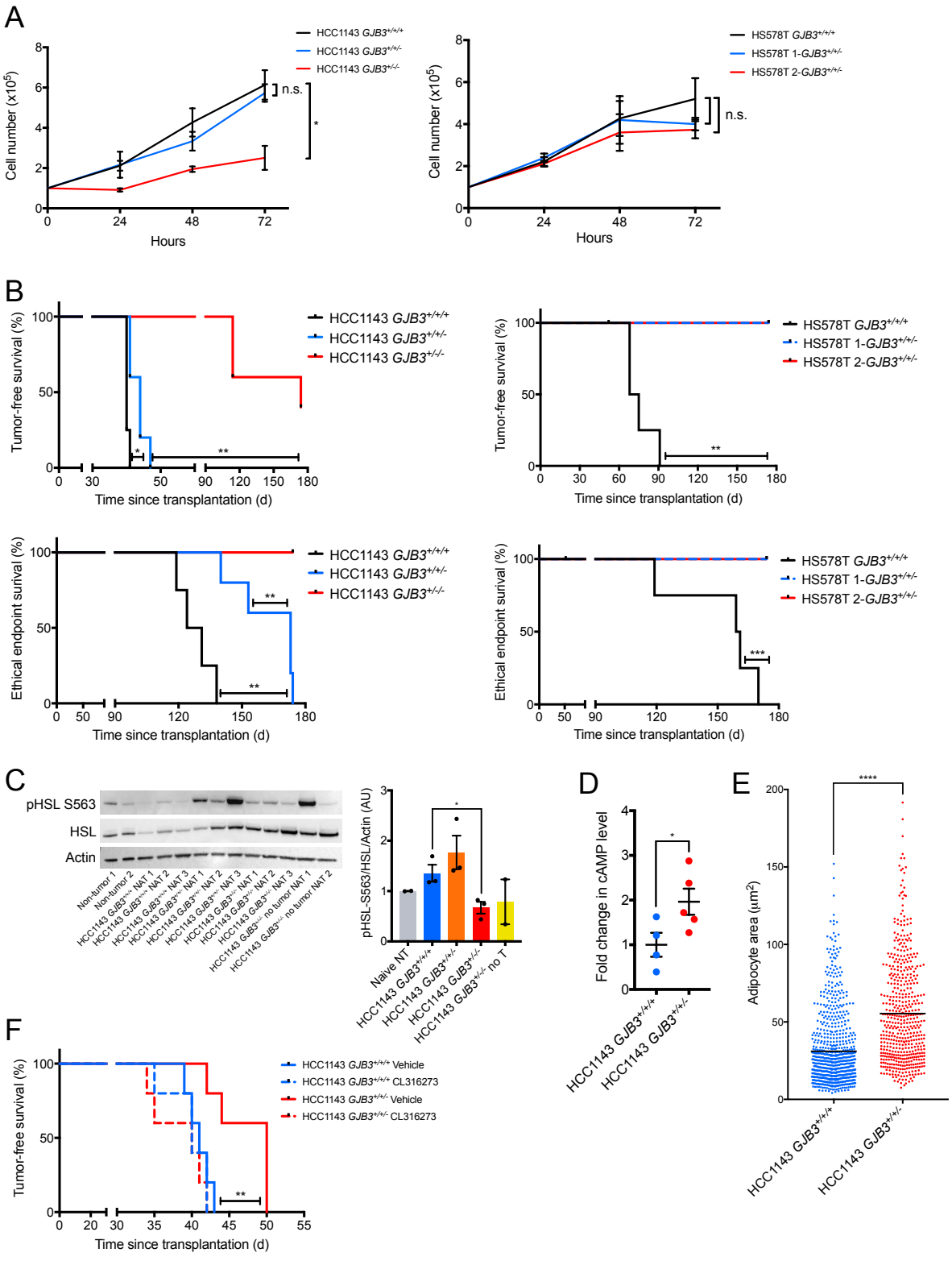

Fig. 4. Cx31 is essential for breast cancer cell growth in vitro, and tumorigenesis and activation of lipolysis in adjacent adipocytes in vivo. (A) Cell growth of indicated Cx31

partial knockout lines over 72 hours. (B) Kaplan-Meier analysis of tumor onset (top) and ethical endpoint survival (bottom) of mice bearing indicated Cx31 partial knockout orthotopic xenografts (n = 5 per group). Ethical endpoint survival indicates the percentage of mice bearing xenografts < 2cm in any dimension. (C) Immunoblot analysis (left) showing expression levels of HSL and phosphorylated HSL (pHSL S563) in healthy non-tumor mammary gland and NAT from mice bearing indicated Cx31 partial knockout xenografts or mice that were transplanted, but subsequently did not develop a tumor. Quantification (right) of pHSL/HSL ratio, normalized to β-actin levels. (D) Fold change in cAMP levels in HCC1143 GJB3+/+/- xenografts versus HCC1143 GJB3+/+/+ xenografts. (E) Adipocyte area adjacent to HCC1143 GJB3+/+/- xenografts (n = 5) and HCC1143 GJB3+/+/+ xenografts (n = 4). The black line indicates mean adipocyte area. Each point represents individual adipocyte. (F) Kaplan-Meier analysis of tumor onset of mice bearing indicated Cx31 partial knockout orthotopic xenografts (n = 5 per group) and treated with vehicle or with 1mg/kg CL316273. For (C) and (D) mean ± s.e.m. is shown. *P < 0.05, **P < 0.01, ***P < 0.001, ****P < 0.0001; unpaired two-tailed t test (A), (C), and (D), log-rank test (B) and (F).

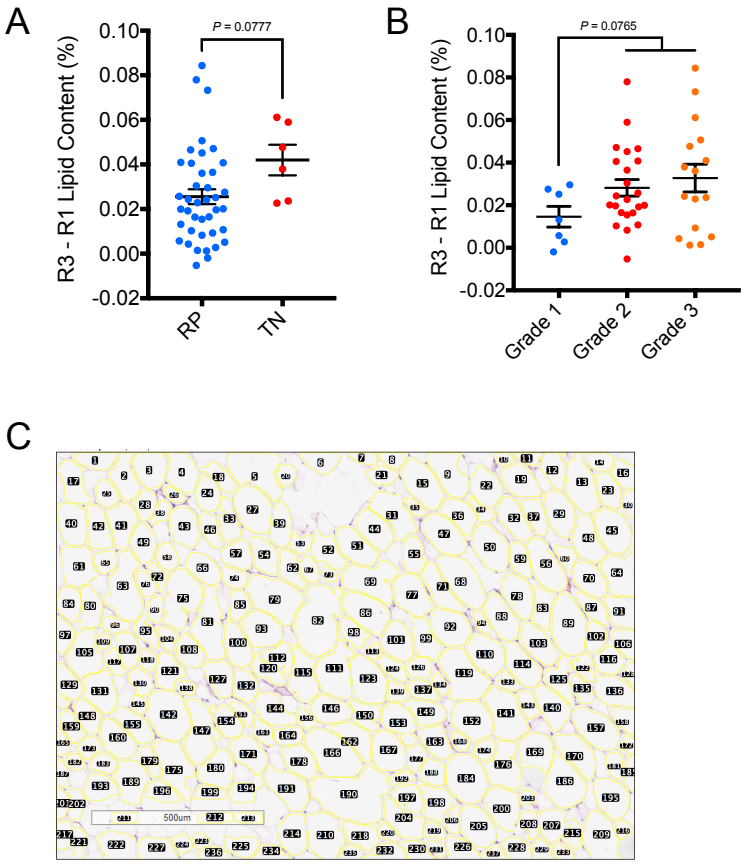

Fig. S1. NAT lipid content by receptor status and tumor grade, and adipocyte area quantification. (A) Change in lipid content in R3 of NAT versus R1 of NAT from TN and RP patients. (B) Change in lipid content in R3 of NAT versus R1 of NAT from grade 1, 2 and 3 patients. (C) Example of Adiposoft software output on manual mode before curation to identify whole, individual adipocytes. P values indicated; unpaired two-tailed t test (A) and (B).

Supplementary Tables 1-3

All supplementary tables can be found using the following link:

https://www.biorxiv.org/content/early/2018/03/07/277939.figures-only

References

1. A. D. Laidevant, S. Malkov, C. I. Flowers, K. Kerlikowske, J. A. Shepherd, Compositional breast imaging using a dual-energy mammography protocol. Med. Phys. 37, 164–174 (2009).
2. S. Malkov, J. Wang, K. Kerlikowske, S. R. Cummings, J. A. Shepherd, Single x-ray absorptiometry method for the quantitative mammographic measure of fibroglandular tissue volume. Med. Phys. 36, 5525–5536 (2009).
3. S. Malkov, J. Wang, F. Duewer, J. A. Shepherd, in International Workshop on Digital Mammography (2012; http://link.springer.com/10.1007/978-3-642-31271-7_99), pp. 769–774.
4. S. Malkov et al., in International Workshop on Digital Mammography (2016; http://link.springer.com/10.1007/978-3-319-41546-8), vol. 9699, pp. 211–218.
5. K. Drukker et al., Mammographic quantitative image analysis and biologic image composition for breast lesion characterization and classification. Med. Phys. 41, 31915 (2014).
6. M. E. H. Hammond et al., American Society of Clinical Oncology/College of American Pathologists guideline recommendations for immunohistochemical testing of estrogen and progesterone receptors in breast cancer (unabridged version). Arch. Pathol. Lab. Med. 134, e48-72 (2010).
7. A. C. Wolff et al., Recommendations for Human Epidermal Growth Factor Receptor 2 Testing in Breast Cancer: American Society of Clinical Oncology/College of American Pathologists Clinical Practice Guideline Update. J. Clin. Oncol. 31, 3997–4013 (2013).

8. M. Galarraga et al., Adiposoft: automated software for the analysis of white adipose tissue cellularity in histological sections. J. Lipid Res. 53, 2791–2796 (2012).
9. K. Shinoda et al., Genetic and functional characterization of clonally derived adult human brown adipocytes. Nat. Med. 21, 389–394 (2015).
10. R. G. W. Verhaak et al., Prognostically relevant gene signatures of high-grade serous ovarian carcinoma. J. Clin. Invest. 123, 517–25 (2013).
11. A. S. L. Cheng et al., Epithelial progeny of estrogen-exposed breast progenitor cells display a cancer-like methylome. Cancer Res. 68, 1786–96 (2008).
12. M. Dai et al., Evolving gene/transcript definitions significantly alter the interpretation of GeneChip data. Nucleic Acids Res. 33 (2005), doi:10.1093/nar/gni179.
13. B. Zhang et al., Proteogenomic characterization of human colon and rectal cancer. Nature. 513, 382–387 (2014).
14. Y. S. DeRose et al., Tumor grafts derived from women with breast cancer authentically reflect tumor pathology, growth, metastasis and disease outcomes. Nat. Med. 17 (2011), pp. 1514–1520.
15. C. M. D'Cruz et al., c-MYC induces mammary tumorigenesis by means of a preferred pathway involving spontaneous Kras2 mutations. Nat. Med. 7, 235–239 (2001).
16. R. M. Neve et al., A collection of breast cancer cell lines for the study of functionally distinct cancer subtypes. Cancer Cell. 10, 515–527 (2006).

17. G. K. Smyth, limma: Linear Models for Microarray Data. Bioinforma. Comput. Biol. Solut. Using R Bioconductor, 397–420 (2005).

18. A. Ettinger, T. Wittmann, Fluorescence live cell imaging (Elsevier Inc., ed. 1, 2014; http://dx.doi.org/10.1016/B978-0-12-420138-5.00005-7), vol. 123.

19. S. Stehbens, H. Pemble, L. Murrow, T. Wittmann, Imaging intracellular protein dynamics by spinning disk confocal microscopy (Elsevier Inc., ed. 1, 2012; http://dx.doi.org/10.1016/B978-0-12-391857-4.00015-X), vol. 504.

20. S. J. Stehbens et al., CLASPs link focal-adhesion-associated microtubule capture to localized exocytosis and adhesion site turnover. Nat. Cell Biol. 16, 558–570 (2014).

21. S. Kajimura et al., Initiation of myoblast to brown fat switch by a PRDM16–C/EBP-β transcriptional complex. Nature. 460, 1154–1158 (2009).

22. K. J. Livak, T. D. Schmittgen, Analysis of Relative Gene Expression Data Using Real-Time Quantitative PCR and the 2−ΔΔCT Method. Methods. 25, 402–408 (2001).

23. P. J. Goodwin, R. T. Chlebowski, Obesity and cancer: Insights for clinicians. J. Clin. Oncol. 34, 4197–4202 (2016).

24. R. Camarda et al., Inhibition of fatty acid oxidation as a therapy for MYC-overexpressing triple-negative breast cancer. Nat. Med. 22, 427–432 (2016).

25. J. H. Park et al., Fatty Acid Oxidation-Driven Src Links Mitochondrial Energy Reprogramming and Oncogenic Properties in Triple-Negative Breast Cancer. Cell Rep. 14, 2154–65 (2016).

26. H. Ye et al., Leukemic Stem Cells Evade Chemotherapy by Metabolic Adaptation to an Adipose Tissue Niche. Cell Stem Cell. 19, 23–37 (2016).

27. K. M. Nieman et al., Adipocytes promote ovarian cancer metastasis and provide energy for rapid tumor growth. Nat. Med. 17, 1498–1503 (2011).

28. S. Balaban et al., Adipocyte lipolysis links obesity to breast cancer growth: adipocyte-derived fatty acids drive breast cancer cell proliferation and migration. Cancer Metab. 5, 1 (2017).

29. Y. Y. Wang et al., Mammary adipocytes stimulate breast cancer invasion through metabolic remodeling of tumor cells. JCI Insight. 2 (2017), doi:10.1172/jci.insight.87489.

30. Y.-A. Wen et al., Adipocytes activate mitochondrial fatty acid oxidation and autophagy to promote tumor growth in colon cancer. Cell Death Dis. 8, e2593 (2017).

31. A. J. Hoy, S. Balaban, D. N. Saunders, Adipocyte–Tumor Cell Metabolic Crosstalk in Breast Cancer. Trends Mol. Med. 23, 381–392 (2017).

32. R. C. Hovey, L. Aimo, Diverse and active roles for adipocytes during mammary gland growth and function. J. Mammary Gland Biol. Neoplasia. 15, 279–290 (2010).

33. R. E. Duncan, M. Ahmadian, K. Jaworski, E. Sarkadi-Nagy, H. S. Sul, Regulation of Lipolysis in Adipocytes. Annu. Rev. Nutr. 27, 79–101 (2007).

34. Y. Zhu et al., Connexin 43 Mediates White Adipose Tissue Beiging by Facilitating the Propagation of Sympathetic Neuronal Signals. Cell Metab. 24, 420–433 (2016).

35. L. Palanker, J. M. Tennessen, G. Lam, C. S. Thummel, Drosophila HNF4 Regulates Lipid Mobilization and β-Oxidation. Cell Metab. 9, 228–239 (2009).

36. V. Large et al., Decreased expression and function of adipocyte hormone-sensitive lipase in subcutaneous fat cells of obese subjects 1. J. Lipid Res. 40, 2059–2066 (1999).

37. F. Wang et al., Mammary fat of breast cancer: Gene expression profiling and functional characterization. PLoS One. 9 (2014), doi:10.1371/journal.pone.0109742.

38. D. Aran et al., Comprehensive analysis of normal adjacent to tumor transcriptomes. Nat. Commun. 8, 1077 (2017).

39. T. Aasen, M. Mesnil, C. C. Naus, P. D. Lampe, D. W. Laird, Gap junctions and cancer: communicating for 50 years. Nat. Rev. Cancer. 16, 775–788 (2016).

40. M. A. Gleisner, M. Navarrete, F. Hofmann, F. Salazar-Onfray, A. Tittarelli, Mind the Gaps in Tumor Immunity: Impact of Connexin-Mediated Intercellular Connections. Front. Immunol. 8, 1–17 (2017).

41. Q. Chen et al., Carcinoma–astrocyte gap junctions promote brain metastasis by cGAMP transfer. Nature. 533, 493–498 (2016).

42. M. Osswald et al., Brain tumour cells interconnect to a functional and resistant network. Nature. 528, 93–98 (2015).

43. D. Horiuchi et al., MYC pathway activation in triple-negative breast cancer is synthetic lethal with CDK inhibition. J. Exp. Med. 209, 679–696 (2012).

44. D. C. Koboldt et al., Comprehensive molecular portraits of human breast tumours. Nature. 490, 61–70 (2012).

45. K. Wenzel, D. Manthey, K. Willecke, K. H. Grzeschik, O. Traub, Human gap junction protein connexin31: molecular cloning and expression analysis. Biochem Biophys Res Commun. 248, 910–915 (1998).

46. J. Willebrords, M. Maes, S. Crespo Yanguas, M. Vinken, Inhibitors of connexin and pannexin channels as potential therapeutics. Pharmacol. Ther. (2017), , doi:10.1016/j.pharmthera.2017.07.001.

47. W. Wang et al., Triple negative breast cancer development can be selectively suppressed by sustaining an elevated level of cellular cyclic AMP through simultaneously blocking its efflux and decomposition. Oncotarget (2016), doi:10.18632/oncotarget.13601.

48. Q. A. Wang, C. Tao, R. K. Gupta, P. E. Scherer, Tracking adipogenesis during white adipose tissue development, expansion and regeneration. Nat. Med. 19, 1338–1344 (2013).

Publishing Agreement

It is the policy of the University to encourage the distribution of all theses, dissertations, and manuscripts. Copies of all UCSF theses, dissertations, and manuscripts will be routed to the library via the Graduate Division. The library will make all theses, dissertations, and manuscripts accessible to the public and will preserve these to the best of their abilities, in perpetuity.

I hereby grant permission to the Graduate Division of the University of California, San Francisco to release copies of my thesis, dissertation, or manuscript to the Campus Library to provide access and preservation, in whole or in part, in perpetuity.

Author Signature  Date 07/30/2018